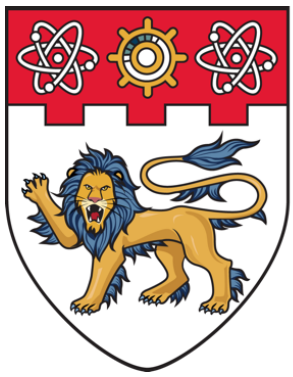

NANYANG TECHNOLOGICAL UNIVERSITY
SINGAPORE

ELECTROCHEMICAL BEHAVIORS AND APPLICATIONS OF COPPER-BASED NANOSTRUCTURES

ZHANG BOWEI

SCHOOL OF MATERIALS SCIENCE AND ENGINEERING

2018

ELECTROCHEMICAL BEHAVIORS AND APPLICATIONS OF COPPER-BASED NANOSTRUCTURES

ZHANG BOWEI

SCHOOL OF MATERIALS SCIENCE AND ENGINEERING

A thesis submitted to the Nanyang Technological University
in partial fulfilment of the requirement for the degree of
Doctor of Philosophy

2018

Statement of Originality

I hereby certify that the work embodied in this thesis is the result of original research and has not been submitted for a higher degree to any other University or Institution.

Input Date Here

. . . . . .

Date

Input Signature Here

. . . . . .

Input Name Here

Supervisor Declaration Statement

I have reviewed the content and presentation style of this thesis and declare it is free of plagiarism and of sufficient grammatical clarity to be examined. To the best of my knowledge, the research and writing are those of the candidate except as acknowledged in the Author Attribution Statement. I confirm that the investigations were conducted in accord with the ethics policies and integrity standards of Nanyang Technological University and that the research data are presented honestly and without prejudice.

Input Date Here	Input Supervisor Signature Here
. . . . .	. . . . .
Date	Input Supervisor Name Here

Authorship Attribution Statement

This thesis contains material from two papers published in the following peer-reviewed journals where I was the first author.

Chapter 4 is published as Zhang, B., Chen, B., Wu, J., Hao, S., Yang, G., Cao, X., Jing, L., Zhu, M., Tsang, S., Teo, H., Huang, Y. The Electrochemical Response of Single Crystalline Copper Nanowires to Atmospheric Air and Aqueous Solution. *Small*, **13(10)**, 1603411 (2017). DOI: 10.1002/smll.201603411.

The contributions of the co-authors are as follows:

- A/Prof Huang Yizhong and Prof. Wu Junsheng provided the initial project direction and edited the manuscript drafts.
- I prepared the manuscript drafts. The manuscript was revised by Dr Chen Bensong and A/Prof. Edwin Hang Tong Teo.
- I co-designed the study with Dr. Chen Bensong and performed all the laboratory work at the School of Materials Science and Engineering. I also analyzed the data.
- All microscopy, including sample preparation, was conducted by me, Dr. Hao Shiji, and Mr. Cao Xun in the Facility for Analysis, Characterization, Testing and Simulation.
- Dr Chen Bensong, Dr. Zhu Minmin and Dr Siu Hon Tsang assisted in the fabrication of the AAO template and CuNWs.
- Mr. Yang Guang and Mr. Jing Lin assisted in the test and interpretation of the X-ray diffraction data.

Chapter 5 is published as Zhang, B., Yang, G., Li, C., Huang, K., Wu, J., Hao, S., & Huang, Y. Electrochemical behaviors of hierarchical copper nanodendrites in alkaline media. In press, *Nano Research* (2018). DOI: 10.1007/s12274-018-2010-3.

The contributions of the co-authors are as follows:

- A/Prof Huang Yizhong and Prof. Wu Junsheng provided the initial project direction and edited the manuscript drafts.
- I prepared the manuscript drafts. The manuscript was revised by Mr Yang Guang and Mr. Huang Kang.
- All microscopy, including sample preparation, was conducted by me Dr. Li Chaojiang and Dr. Hao Shiji in the Facility for Analysis, Characterization, Testing and Simulation.
- I performed the materials synthesis and carried transmission electron microscopy, and conducted data evaluation.
- Mr. Yang Guang collected all the X-ray diffraction patterns and performed the analysis.

Input Date Here	Input Signature Here
. . . . .	. . . . .
Date	Input Name Here

Abstract

Copper based nanomaterials (Cu, Cu_2O, CuO et al) have been broadly used in electrochemistry related fields due to their favorable performance and the cost effective features. In such practical applications, the electrochemical degradation of Cu-based nanomaterials is much more serious than their counterparts owing to their large surface-to-volume ratio and plentiful surface defects, especially when they are subject to the harsh solutions and high applied potentials. As a consequence, it is of vital significance to study the electrochemical behaviors of Cu-based nanomaterials and use them as references to improve their performance in electrochemical applications.

First, large aspect ratio single crystalline copper nanowires (CuNWs) have been electrochemically deposited by using anodic aluminum oxide (AAO) template. Then, the surface passivation behaviors of the as-obtained CuNWs in both 40 % relative humidity (RH) atmosphere and 0.1 M NaOH aqueous solution have been studied by transmission electron microscope (TEM) observations. In 40 % RH atmosphere, a uniform compact Cu_2O passivation layer epitaxially covers the CuNWs surface following a logarithmic law relationship between Cu_2O thickness and exposure time, while showing faster growth rate than that on the counterpart bulky Cu surface under the same conditions. The electrochemical passivation behaviors of CuNWs in 0.1 M NaOH solution were investigated by cyclic voltammetry measurements. Initially, a homogeneously compact Cu_2O layer is observed to epitaxially coat the CuNWs substrate under solid-state reaction (SSR) mechanism at the first oxidation peak. Subsequently, the previously formed epitaxial compact Cu_2O layer will be partially oxidized into a compact CuO inner layer with parallel alignment and an adjacent disordered CuO/$Cu(OH)_2$ outer layer with random orientations under the dissoloution-redeposition (DR) mechanism at the second oxidation peak. When further increasing the applied potential prior to the oxygen evolution, the parallelly orientated Cu_2O/CuO inner layer will be completely oxidized into disordered CuO and $Cu(OH)_2$. Finally, a dual-layer structure (CuO inner layer and $Cu(OH)_2$ outer layer) with random orientation forms on CuNW substrate through an enhanced DR mechanism.

Subsequently, hierarchical copper nano-dendrites (CuNDs) are fabricated via electrodeposition method since they can reflect the influence of micro-structure of copper to their electrochemical properties besides the intrinsic ones. It is found that the CuNDs experience a non-equilibrium oxidation process when subject to the cyclic voltammetry (CV) measurement. As expected, the first oxidation peak corresponds to the formation of an epitaxial Cu_2O layer over the surface of hierarchical CuNDs. Unusually, a broad oxidation peak including a plateau appears at higher potentials in the CV profile. Scanning electron microscopy (SEM) and transmission electron microscopy (TEM) observations demonstrate that the nucleation and growth of $Cu(OH)_2$ nanoneedles at the localized regions originate and dominate the initial part of the second oxidation peak. Subsequently, further oxidation of the previously formed Cu_2O layer take place until it is completely transformed into CuO and $Cu(OH)_2$ to form a dual-layer structure at higher anodic potentials. Meanwhile, a larger amount of $Cu(OH)_2$ nanoneedles sprout and grow in the CuNDs as well.

In order to improve the OER electrocatalytic activity of the CuNDs electrode, a strategy that transforming a metal organic frameworks (MOFs) thin layer into a nanostructured CuO/C hollow shell to coat on the 3D CuNDs was successfully developed. This electrode is claimed to provide an extraordinary electrocatalysis for oxygen evolution reaction (OER) in alkaline media. The hierarchical complex presents fast electronic transmission networks and rich redox sites, leading to the significant enhancement in electrocatalytic OER efficiency. Furthermore, the spherical porous structure and robust architecture facilitate the high-speed diffusion of O_2 bubbles in a long-term operation. The results of this study may serve as a reference for the designing of novel class 3D metal/metal oxide hierarchical structures for gas-involved (i.e. O_2, H_2, CO_2 et al) electrocatalytic applications and beyond.

Lay Summary

Due to the earth abundance and cost effectiveness, copper-based materials have been widely used in various fields. However, the corrosion on Cu-based materials remains a big problem since they can easily react with oxidizing media including oxygen, acid and alkaline solutions et al. Although the study of the corrosion behaviors on bulk copper materials have been extensively conducted, similar research on copper nanomaterials was rarely reported. When the size of copper materials reduces to nanoscale, their surface-to-volume ratio (the amount of surface area per unit volume of an object or collection of objects) will subsequently increase. Therefore, a larger copper surface is exposed to the corrosive environment so that the copper nanomaterials will be corroded fast. In addition, there are more surface defects on nanoscale copper materials, which may lead to a different corrosion behavior from that on the bulk ones. As a consequence, it is important to study the corrosion mechanism of Cu nanomaterials in different environments.

In the thesis, the study of degradation mechanism of copper nanowires and copper nano-dendrites materials was conducted. Based on the analysis of the structure and composition on the surface of copper nanomaterials at different conditions, the corrosion mechanism was successfully revealed. The results show that the corrosion of Cu nanomaterials is much easier and faster than that on the bulk Cu materials. The corrosion mechanism on the copper nanomaterials is partially identical to the bulk copper, except the formation process of the oxide layer at high potentials. Moreover, the difference in the structure of the Cu nanomaterials can lead to a huge diversity on their corrosion behaviors. The discovery in this study can used to guiding the improvement of Cu-based nanomaterials in practical applications.

Being used as catalysts for water splitting for oxygen generation is one of the most important applications of Cu-based nanomaterials. Since the oxygen production above is carried out in strong alkaline solution, the surface stability is crucial to prevent the degradation of Cu-based catalysts. In the current project, a protective layer was grown on the surface of Cu-based catalyst by heat treatment method. On the other hand, the efficiency

of oxygen production requires a large contacting area between the alkaline solution and catalyst surface. Therefore, a thin layer consisting of CuO nanoparticles was coated at the outmost position to maximize the surface area of Cu-based catalyst so that the catalytic reactions can take place efficiently. At the same time, carbon material was also incorporated in the outer CuO layer in order to enhance the conductivity of the CuO catalyst. This is to increase the transport speed of the electrons during the catalytic reactions so that the oxygen could be produced efficiently.

Acknowledgements

This dissertation would not have been possible without funding from NTU RSS scholarship, AcRF grant MOE Singapore, National Natural Science Foundation of China, conference support from MSE and so on.

I would like to express my sincerest gratefulness to my supervisor, Prof. Huang Yizhong. His positive encouragements, insightful guidance and invaluable enlightenment extensively help me throughout my 4-year PhD study and life. Especially, his patience, care and prudence in revising my thesis and papers will undoubtedly benefit me in my future academic career.

I also want to appreciate Prof. Wu Junsheng from University of Science & Technology, Beijing (China), who also provides me valuable suggestions, considerate supervision and also abundant experimental support to fulfill my PhD project.

I express my gratitude to all FACTs staff and other technicians, especially Tay Yee Yan for patiently guiding me on the operation of TEM and its related equipment.

Many thanks and appreciations go to Dr. Chen Bensong from Institute of Solid State Physics, Chinese Academy of Sciences and Mr. Huang Kang from University of Science & Technology, Beijing (China) for the collaboration.

My gratitude also goes to the colleagues in my group. Their cheerful encourage, priceless friendship, innovative suggestions and the meaningful discussion, skills sharing accompany me in my experimental and daily life.

At last, I dedicate the thesis to my dear family members. I can never come this far without their unconditional care, understanding and support. I love you!

Table of Contents

Table Captions

Figure Captions

Figure 4.3 (a) Low-magnification TEM image of the as-fabricated CuNWs; (b) HRTEM image of one typical CuNW and the inset shows the FFT pattern of the CuNW; (c) XRD patterns of the samples embedded in AAO template; (d) EDX spectrum of the CuNW.

Figure 4.4 HRTEM images of fresh CuNWs. (a)- (d) correspond to II-V, respectively.

Figure 4.5 HRTEM images of (a) the fresh CuNW (I) and (b) after it was exposed to air for 3 hours.

Figure 4.6 HRTEM images of CuNWs II-V after being exposed in air 40% RH after (a-d) 6, 24, 48, and 96 h, respectively. Each inset on the top right corner is the corresponding FFT patterns. The white dotted line in each panel represents the interface between the outer layer and the inner CuNW substrate.

Figure 4.7 Experimental plots and fitting curve of the film thickness on CuNWs *vs* the exposure time in 40% RH atmosphere.

Figure 4.8 A cyclic voltammetry profile of CuNWs in 0.1 M NaOH aqueous.

Figure 4.9 (a) Low- magnification TEM image of one typical CuNW after being polarized to –0.15 V; (b) HRTEM image of the square A in panela and the inset on the top right corner is the corresponding FFT pattern.

Figure 4.10 (a) Low- magnification TEM image of one typical CuNW after being polarized to + 0.45 V. (b) and (c) are the HRTEM images taken from the marked areas B and C in panel c. The FFT patterns (F', G', H' and I') correspond to the marked area F, G, H and I in panel e.

Figure 4.11 (a) Low- magnification TEM image of one typical CuNW after being polarized to + 0.8V; (b) and (c) HRTEM image of the square A and B in panela. The FFT patterns (D', E', F', and G') correspond to the marked area D, E, F in panel b and region

G in panel c, respectively.

Figure 4.12 Schematic evolution of the oxide films on CuNWs under the different electrochemical potentials in 0.1 M NaOH solution.

Figure 5.1 Schematic of the fabrication of CuNDs by hydrogen-bubbles assist strategy.

Figure 5.2 (a) XRD pattern of CuNDs after surface cleaning; (b-d) SEM images of CuNDs at different magnifications; (e, f) Low magnification and high resolution TEM images of CuNDs.

Figure 5.3 (a) Low magnification and (b) high resolution TEM images of CuNDs.

Figure 5.4 A cyclic voltammetry curve of CuNDs electrode in 0.1 M NaOH aqueous solution.

Figure 5.5 (a) XRD pattern, (b) SEM image of CuNDs after being polarized to – 0.2 V.

Figure 5.6 (a) Low magnification and (b) high resolution TEM images of CuNDs after being polarized to – 0.2 V. The FFT patterns (A' and B') correspond to the marked areas A and B in panel d.

Figure 5.7 (a) XRD pattern, (b) SEM image of CuNDs after being polarized to + 0.2 V.

Figure 5.8 (a) Low magnification TEM image of CuNDs after being polarized to + 0.2 V; (b) HRTEM image taken from the marked area in panel a; (c) Low magnification image of a nanoneedle that grown during the electrochemical oxidation process; (d) HRTEM image taken from the marked area in panel c. The FFT patterns in (b) and (d) are transformed from the squares marked in the corresponding image, respectively.

Figure 5.9 (a) XRD pattern, (b) SEM image of CuNDs after being polarized to + 0.75 V.

Figure 5.10 (a) Low magnification TEM images of CuNDs after being polarized to + 0.75 V; (b-d) HRTEM images taken from the marked area A,B and C in panel a, respectively. The inset FFT patterns in panel b is transformed from the square marked in the corresponding image. The FFT patterns E', F', G' and H' are derived from the squares E, F, G and H, respectively.

Figure 5.11 The oxidation process on CuNWs with the increase of electrochemical potential in 0.1 M NaOH aqueous solution.

Figure 5.12 (a) LSV curves of polarized CuNDs electrode in 1.0 M KOH solution at a scan rate of 5 mV s^{-1}; Tafel plots (b) and Nyquist plots (c) of the NDs electrode.

Figure 6.1 Schematic of the fabrication of HS-CuO/C NDs.

Figure 6.2 Top view (a), side view (b) and low magnification (c) and high magenification (d) SEM images of as-prepared Cu_2O-Cu NDs.

Figure 6.3 TEM image (a) and XRD pattern (b) of as prepared Cu_2O-Cu NDs.

Figure 6.4 SEM image (a), XRD pattern (b) and TEM image (c) of as prepared MOFs coated NDs.

Figure 6.5 STEM image (a) and EDX mapping images (b-d) of MOFs coated NDs.

Figure 6.6 Low (a) and high magnification (b) SEM images of HS-CuO/C NDs; low magnification (c) and HRTEM (d) images of HS-CuO/C NDs.

Figure 6.7 SEM (a) and TEM (b) images of PS-CuO/C NDs; (c) SEM image of PS-CuO NDs.

Figure 6.8 STEM-EDX mapping (a) and inside-out line scan (b) of HS-CuO/C NDs.

Abbreviations

CuNWs	Copper Nanowires
AAO	Anodic Aluminum Oxide
RH	Relative Humidity
SSR	Solid-State Reaction
DR	Dissolution-Redeposition
CuNDs	Copper Nano-Dendrites
CV	Cyclic Voltammetry
MOFs	Metal Organic Frameworks
OER	Oxygen Evolution Reaction
CuNPs	Copper Nanoparticles
CuNCs	Copper Nanoclusters
TEM	Transmission Electron Microscopy
SEM	Scanning Electron Microscopy
XRD	X-ray Diffraction
PEMFCs	Proton Exchange Membrane Fuel Cells
DFT	Density Function Theory
BCDI	Bragg Coherent Diffraction Imaging
HRTEM	High Resolution Transmission Electron Microscopy
nZVI	Nano Zero-Valent Iron
IHOAM	Incipient Hydrous Oxide/ Adatom Mediator
DMFCs	Direct Methanol Fuel Cells
SCE	Saturated Calomel Electrode
ORR	Oxygen Reduction Reaction
HER	Hydrogen Evolution Reaction
RHE	Reversible Hydrogen Electrode
LDHs	Layered Double Hydroxides
3D	Three Dimensional
CCD	Charge-Coupled Device
SAED	Select Area Electron Diffraction

STEM	Scanning Transmission Electron Microscopy
EELS	Electron Energy Loss Spectroscopy
BEI	Backscattered Electron Imaging
XPS	X-ray photoelectron spectroscopy
FFT	Fast Fourier Transform
ECSA	Electrochemically-active Surface Area
C_{dl}	Double Layer Capacitance
R_{ct}	Charge Transfer Resistance
FIB	Focused Ion Beam
EDX	Energy Dispersive X-ray Spectroscopy
HRTEM	High Resolution Transmission Electron Microscopy
SAED	Selected Area Electron Diffraction
SEI	Secondary Electron Images

Chapter 1

Introduction

This chapter gives an overview on this thesis, which begins with the introduction of the hypotheses, followed by the description of the objectives and scope based on the hypothesis. Subsequently, the dissertation overview for each chapter in the present thesis is described. Finally, the findings and outcomes of this thesis on the basis of the whole content are summarized.

1.1 Hypothesis/Problem Statement

Copper nanomaterials, including copper nanowires (CuNWs), including copper nanoparticles (CuNPs) and copper nanoclusters (CuNCs) et al, have been drawn considerable attention in the past decade.[1-3] Attributing to their excellent electrical and thermal conductivities as well as the earth-abundance, copper nanomaterials play very important roles in many different application fields. Compared to the bulky Cu materials, the large surface-to-volume ratio of Cu nanomaterials makes them much more sensitive to the environment when being applied in the practical applications. As a consequence, corrosion on Cu nanomaterials tends to occur on the surface due to complicated electrochemical processes. Based on the problem statement above, the hypothesis here can be described as followed:

- The thesis first tests that the electrochemical behaviors of homogeneous CuNWs in atmospheric air and aqueous solution are much different from those of their bulky counterparts, which could provide essential evidence in failure analysis of CuNWs-based devices and illuminate more modification and protection methods in the real applications.

Besides widely applied in electronic fields, copper nanomaterials can also be used as promising electrocatalysts, such as oxygen evolution reaction (OER), methanol oxidation and CO_2 reduction et al.[4-6] In order to improve the electrochemical activities of Cu nanomaterials, various synthetic approaches have been employed to increase the density of active sites for electrocatalysis. Fabrication of copper nano-dendrites (CuNDs) structures is among one of the most effective methods to achieve a high-performance catalytic electrode with a large surface area. Being assembled with numerous CuNPs, the CuNDs possess a hierarchical structure, where a large amount of boundaries are exposed among the CuNPs, greatly increasing their risk of vulnerability. As a result, the hypothesis here is stated as followed:

- The thesis tests that peculiar phenomena will occur on CuNDs when they are subject to electrochemical tests in aqueous solution due to their hierarchical structures, which is far different from the CuNWs with homogeneous structure. The results in this study

contribute to the understanding of electrochemical behaviors of nanomaterials with hierarchical structures.

Copper based nanomaterials (Cu, Cu_2O, CuO and Cu_3P et al) have been broadly used in electrocatalysis due to their favorable performance and the cost effective feature.[7-10] As mentioned above, CuNDs electrode has great potential in electrocatalysis ascribed to its excellent conductivity, high porosity, hierarchical structure and large surface area. However, the instability of bare CuNDs in aqueous solution when subject to electrochemical treatments limits their adoption in practical applications. For the purpose of improve the stability of CuNDs, surface modification appears a necessary and effective approach. On the other hand, sufficient active sites should be created on the surface of CuNDs so that a highly efficient catalyst is obtained. Herein, the hypothesis to be put forward is as follows:

- The thesis tests that modification towards improving surface stability coupled with abundant active sites for electrocatalysis is a promising way to fabricate a high efficient catalyst with long-term durability in aqueous solution. Specifically, nanostructured CuO coating might act as active layer whilst the CuO passive film formed via heat-treatment could protect the CuNDs from corrosion in harsh alkaline electrolyte.

1.2 Objectives and Scope

The main objective of this thesis is to investigate the electrochemical behaviors of copper nanomaterials with different structures in aqueous solution followed by the fabrication of high performance Cu-based electrocatalysts for oxygen evolution reaction. Based on the hypotheses above, the detailed objectives and scope is listed below:

First, large-scale single-crystalline CuNWs with homogeneous appearance will be prepared using a template strategy, where the CuNWs are electrodeposited into an anodic aluminum oxide template via a chronoamperometric method. Subsequently, the CuNWs with absolutely clean surface will be gone through the air-exposure and electrochemical treatment before the structure characterization by transmission electron microscopy (TEM).

The growth rate of the passive film that is formed under air-exposure will be calculated based on the TEM results. In addition, the mechanism of oxide layers growing on CuNWs via cyclic voltammetry (CV) method in alkaline solution can also be revealed by analyzing the structural evolution of the surface passive film.

Second, CuNDs with hierarchical 3D structure will be fabricated via a hydrogen-bubble assistance strategy, where copper nanoparticles are electrodeposited onto the copper foil accompanied with hydrogen evolution from the copper foil surface so that a general porous structure is obtained. Electrochemical measurement on as-prepared CuNDs electrode will be conducted via a CV method in alkaline solution to investigate their electrochemical response compared to the homogeneous CuNWs. On the basis of scanning electron microscopy (SEM), X-ray diffraction (XRD) and TEM results, the oxidation mechanism of CuNDs in alkaline solution will be disclosed. Meanwhile, attributed to the great potential of the as-prepared CuNDs electrode as an electrocatalyst (i.e. large surface area, high conductivity and global porous structure), its OER activity will be studied.

Third, given the vulnerability of bare CuNDs electrode caused by high-density defects among the copper nanoparticles, modification on CuNDs is required to improve their surface stability towards a durable electrocatalysis for OER in aqueous solutions. Specifically, a thin layer of metal organic frameworks (MOFs) that are transformed from the previously formed Cu_2O layer can be in-situ grown on the surface of CuNDs. Heat treatment will be followed to realize the transformation of Cu-MOFs into nanostructured CuO/C layer on top of the CuNDs. Meanwhile, a protective passivation film consists of CuO_x is able to formed between the Cu substrate and the CuO/C layer. Thus, a core-shell structure composed of passivated Cu substrate and nanostructured CuO/C layer could be fabricated. The OER performance of as-prepared CuO/C coated Cu/CuO_x nano-dendrites electrode will be investigated.

1.3 Dissertation Overview

The thesis addresses how to investigate the electrochemical behaviors of homogeneous single-crystalline CuNWs and hierarchical CuNDs in aqueous solution by means of the combination of electrochemical measurements and TEM analysis. The thesis also addresses how to fabricate a copper-based hierarchical structures via electrochemical method on the basis of the understanding of electrochemical behavior of CuNDs in aqueous solution. In addition, the thesis also exhibits how to prepare a high-performance Cu-based OER catalyst by using multiple synthetic approaches.

The study of oxidation process on CuNWs contributes to study the natural electrochemical properties of nanoscale pure copper materials whilst revealing the mechanism of oxidation on CuNDs is associated with the nature of copper coupled with the influence of morphology-related factors.

Chapter 1 provides a rationale for the research and outlines the goals and scope.

Chapter 2 reviews the literature concerning the mechanism study on electrochemical behaviors of metallic nanomaterials in various applications, especially the current progress on the electrochemical properties of pure copper nanomaterials. It also contains the literature about the copper-based nanomaterials and nanostructures in energy conversion applications.

Chapter 3 discusses the rational of the methods that are used in the thesis study. It also discusses the principles underlying the synthesis/characterization techniques employed and the methods of data analysis.

Chapter 4 elaborates the synthesis and characterization of electrodeposited single-crystalline CuNWs, followed by the study on their electrochemical behaviors in atmospheric air and aqueous solution on the basis of the combination of electrochemical measurements and TEM analysis.

Chapter 5 elaborates the fabrication and characterization of electrodeposited three dimensional CuNDs. Subsequently, the electrochemical behaviors of the bare CuNDs in alkaline solution is investigated. Based on the understanding of the electrochemical properties of the CuNDs, Cu-based NWs@NDs hierarchical structure is prepared towards the catalysis of water oxidation.

Chapter 6 elaborates a modification approach to coat a nanostructured CuO/C hollow shell that is derived from Cu-MOFs (HKUST-1) on the surface of CuNDs electrode. The electrochemical performance of as-prepared catalyst above for OER in alkaline solution is subsequently studied.

.

Chapter 7 draws conclusions of the whole thesis and elaborates the opportunities and strategies should be accomplished in the near future.

1.4 Findings and Outcomes/Originality

This research led to several novel outcomes by:

1. TEM analysis has been proved to very powerful for the characterization of the structures of the single-crystalline CuNWs after being subject to electrochemical treatments in atmospheric air and aqueous solution. The structural and compositional evolution of the oxide layers that are formed on the surface of CuNWs during the electrochemical processes has been investigated, which contributes to the understanding of oxidation mechanism of CuNWs in the surrounding environments.

2. 3D Cu foam consists of CuNDs has been prepared, followed by the study of its electrochemical behaviors by SEM, TEM and XRD. As predicted in the hypothesis, the electrochemical properties of the as-fabricated CuNDs with hierarchical structure in alkaline solution under CV test present to be much different from the homogeneous single-crystalline CuNWs, where a non-equilibrium oxidation

process occurs on the CuNDs electrode. Based on the mechanism study above, Cu-based catalyst with NWs@NDs hierarchical structures have been fabricated towards the electrocatalysis of water oxidation.

3. CuNDs electrodes with MOFs derived CuO/C coating have been successfully prepared via an in-situ transformation strategy. In the OER performance evaluation, the NDs catalysis with CuO/C layers exhibit a much better activities than that the bare NDs electrode. Especially for the CuO/C hollow shell coated NDs (HS-CuO/C NDs), it only requires a low overpotential of 286 mV to achieve a current density of 10 mA cm^{-2} in 1 M KOH solution at a Tafel slope of 66.3 mV dec^{-1}. In addition, the HS-CuO NDs can also sustain a high stability in catalysis due to the protection of a passive layer under the hollow shell.

References

[1] Bhanushali, S.; Ghosh, P.; Ganesh, A.; Cheng, W., *Small* **2015,** *11* (11), 1232-1252.

[2] Shown, I.; Hsu, H.-C.; Chang, Y.-C.; Lin, C.-H.; Roy, P. K.; Ganguly, A.; Wang, C.-H.; Chang, J.-K.; Wu, C.-I.; Chen, L.-C., *Nano Lett.* **2014,** *14* (11), 6097-6103.

[3] Wang, C.; Wang, C.; Xu, L.; Cheng, H.; Lin, Q.; Zhang, C., *Nanoscale* **2014,** *6* (3), 1775-1781.

[4] Liu, Y.; Li, Q.; Si, R.; Li, G. D.; Li, W.; Liu, D. P.; Wang, D.; Sun, L.; Zhang, Y.; Zou, X., *Adv. Mater.* **2017,** *29* (13).

[5] Han, L.; Cui, P.; He, H.; Liu, H.; Peng, Z.; Yang, J., *J. Power Sources* **2015,** *286*, 488-494.

[6] Sen, S.; Liu, D.; Palmore, G. T. R., *Acs Catal.* **2014,** *4* (9), 3091-3095.

[7] Heli, H.; Jafarian, M.; Mahjani, M.; Gobal, F., *Electrochim. Acta* **2004,** *49* (27), 4999-5006.

[8] Brito, J. F. d.; Silva, A. A. d.; Cavalheiro, A. J.; Zanoni, M. V. B., *Int. J. Electrochem. Sci.* **2014**, 5961-5973.

[9] Dubale, A. A.; Pan, C.-J.; Tamirat, A. G.; Chen, H.-M.; Su, W.-N.; Chen, C.-H.; Rick, J.; Ayele, D. W.; Aragaw, B. A.; Lee, J.-F., *J. Mater. Chem. A* **2015,** *3* (23), 12482-12499.

[10] Wei, S.; Qi, K.; Jin, Z.; Cao, J.; Zheng, W.; Chen, H.; Cui, X., *ACS Omega* **2016,** *1* (6), 1367-1373.

Chapter 2

Literature Review

This chapter gives the literature review on the recent progress of investigating the electrochemical oxidation behaviors of metallic nanomaterials in aqueous solutions. The studies on nanoscale noble metals are introduced first, followed by the reported works on active and transition metals nanomaterials. Subsequently, the application of copper-based nanomaterials in electrochemistry-related fields is summarized. Finally, the questions and the thesis in context based on the literature are also discussed.

2.1 Overview

The metallic nanomaterials have been widely used in various electrochemical-related applications due to their excellent physical, thermal, electrical and electrochemical properties.[1] As we know, metallic nanomaterials usually exhibit much more active than their bulk counterparts ascribed to their larger surface area and high-density defects. Therefore, nano-scale metal materials will experience a much severer degradation than their bulk counterparts caused by the oxidation process occurred on the surface of nano-metals. Especially when they are used in electrochemistry-related fields, where the surrounding atmosphere is oxidative and aggressive. Thus, it is necessary to study the electrochemical oxidation behaviors of metallic nanomaterials in their practical applications, such as biosensing, catalysis and fuel cells et al.

Among the metallic materials, copper is one of the most promising element due to its earth-abundance, cost-effectiveness and favorable performance. As a consequence, copper-based nanomaterials have long been developed and employed in various fields. The study of electrochemical oxidation behavior of nanoscale copper materials is crucial to the understanding of their instinct properties and the inhibition of their degradations in practical applications. Most importantly, it can also gain insights into the fabrication of multifunctional copper-based nanomaterials in a wide range of areas.

2.1.1 Electrochemical oxidation of metallic nanomaterials

Over the past decades, the study on metallic nanomaterials has been playing one of the most important roles in the nanomaterials research, which is considered as the key to realize the innovation and development of modern technologies.[2-4] Recently, metallic nanomaterials with low dimension has been widely used and possess a promising application prospect in various fields, such as nano-devices, multiple-phase catalysis, electrochemical sensor, fuel cells and biomedical et al, attributed to their particular optical, electrical, magnetic properties and excellent surface chemical properties.[5-9] The small size effect, super high specific surface area, large amount of surface defects, suspended bond

of metallic nanomaterials makes their remarkable activities for chemical reactions., which are quite different from the their bulky counterparts.[10] For example, surface reconstruction of nanoscale rhodium is shown in Figure 2.1, where the adsorption of oxygen atoms on the (100) surface of rhodium induces the lattice distortion.[11] However, such high activities of the metallic nanomaterials not only exhibit as specific properties and functions, but also limit their practical applications since they are very easy to be oxidized.[12, 13]

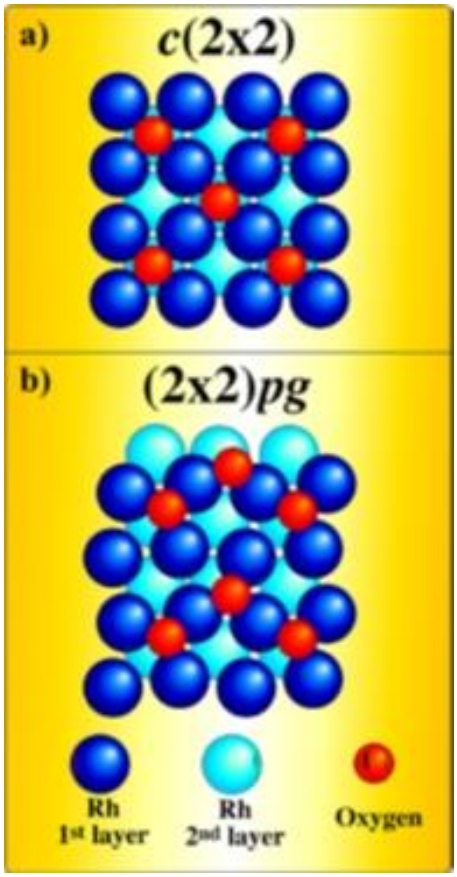

Figure 2.1 Adsorbate over layers on a (100) fcc metal surface (Rh in this case) at a coverage of 0.5 ML.[11]

Although much efforts have been spent on the thermal stability and anti-oxidation properties of metallic nanomaterial, the oxidation of nanoscale metals in aqueous solutions deserves much more attentions since most of their practical applications are in the liquid environments with multiple phases. For instance, metallic nanomaterials, such as Pt, Ru, Co et al, have been broadly used in electrocatalysis of oxygen evolution reaction. As a consequence, it is necessary to study the electrochemical oxidation behaviors of metallic

nanomaterials when they are subject to aqueous solutions, which can also provide more information towards the inhibition of the oxidation as well as the fabrication of novel nanomaterials with various applications.

2.1.1.1 Electrochemical oxidation of nanoscale noble metals

It is well known that the chemical activities of metallic nanomaterials can be exceedingly good as long as the size of the nanomaterials reduces to less than 100 nm in any one dimension. At the expense of high activity, the anti-oxidation behaviors of the metallic nanomaterials will become quite different from the traditional bulk metals. Based on the previous study, severe oxidation will also occur on the inert metals when the size of them reaches down to nanoscale. For example, as shown in Figure 2.2, the electrocatalyst Pt/C that is used in proton exchange membrane fuel cells (PEMFCs) will tend to be electrochemically oxidized and dissolved to become inactivated due to the continuous redox reactions.[14]

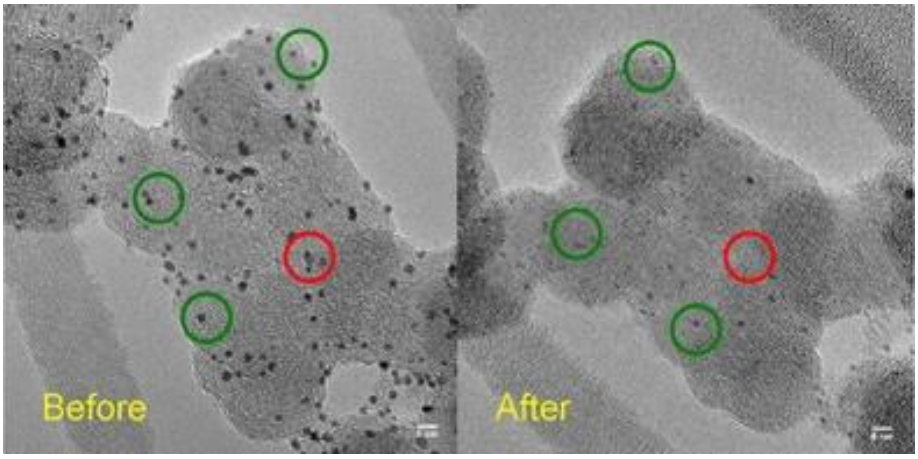

Figure 2.2 IL-TEM images taken before and after accelerated oxidation test.[14]

According to the study on bulk Pt materials. the electrochemical reactions that causing the oxidation of Pt are included below:[15]

$$Pt + H_2O = PtO + 2H^+ + 2e^- \quad (1)$$

$$PtO + H_2O = PtO_2 + 2H^+ + 2e^- \quad (2)$$

$$PtO_2 + H_2O = PtO_3 + 2H^+ + 2e^- \quad (3)$$

As for the Pt nanomaterials, Tang et al believes that the deactivation in acid solutions is due to the generation of dissolvable Pt^{2+} during the electrochemical oxidation reactions,[16, 17] which is much different from the oxidation mechanism of bulk Pt. The authors have also drawn the Potential-pH diagram of Pt nanoparticles with different sizes in acid solutions, as illustrated in Figure 2.3. The results shows that a negatively shift of the equilibrium potential occurs in the Pt/Pt^{2+} system. The Pt nanoparticles with 1 nm diameter cannot even exist stably at an applied potential of 0.4 $V_{vs.SHE}$. Thus, it is convincing that the dissolution of Pt nanoparticles dominates the electrochemical process.

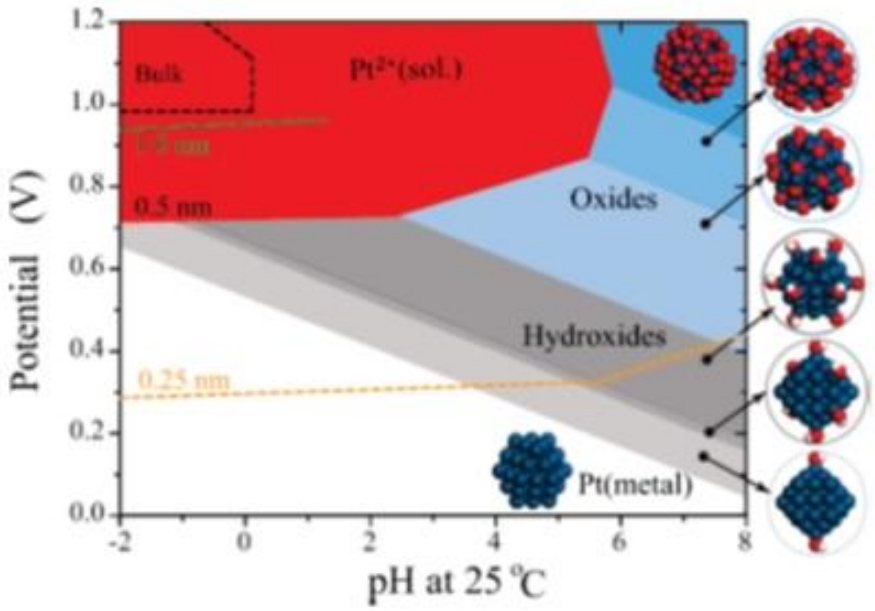

Figure 2.3 Ab initio calculated Pourbaix diagram for a Pt particle with radius 0.5 nm.[16]

Generally, the surface of the nanoparticles presents to be isotropic. The decreased stability of the nanoparticles are mainly resulted from the reduction of their cohesive energy. As a matter of fact, the ration of surface atoms on the terraces to those at the edges and peaks gradually decreases along with the shrinkage of the particle size. Thus, the reducing atomic coordination number leads to a drastically negative shift of the Nernst equilibrium potential of the metallic nanoparticles. However, the strongly unsaturated coordination absorption of the O and OH^- onto the surface of nanoparticles will in turn results in the surface passivation so that the dissolution of Pt is inhibited. According to the density function

theory (DFT) calculation of Jinnouchi, although the surface Pt atoms at the terrace edges possess a relatively low cohesive energy and exhibit a high tendency of being dissolved, the strong absorption of oxygen atoms onto these Pt atoms will also occur during the electrochemical polarization process.[18] Therefore, the electrochemical dissolution and oxygen behaviors of Pt nanoparticles is rather complicated, where the cohesive energy based on the size and shape effect, surface absorption and the equilibrium potential of dissolution/precipitation should be taken into account at the same time. Currently, the main applications of the noble metal nanomaterials focus on fuel cells, electrocatalysis and systems with strongly oxidative media, the peculiar electrochemical oxidation behaviors of these nanoscale noble metals are worthy of more attention.

Being a relatively cheap noble metal, nanoscale silver materials also exhibit some special physiochemical properties, which have been extensively used in varieties of fields, such as catalysis, biosensor, solar cells, micro-electronic and anti-bacteria et al.[19-23] It has been a general concern that the electrochemical oxidation behaviors of Ag nanomaterials in atmospheric air and aqueous solutions. Ivanova et al has studied the electrochemical behaviors of the Ag nanoparticles.[24] The results show that the redox potential of the Ag nanoparticles will gradually shift negatively with the decrease of the particle size, which is much lower than the bulk Ag in the same conditions. Another technique Bragg coherent diffraction imaging (BCDI) has also been employed to in situ investigate the electrochemical oxidation process of Ag nanoparticles, providing the direct evidence that the surface stress and defects of the nanoparticles have a strong influence on the corrosion process.[25] In addition, the study also found that the oxidation of the Ag nanoparticles initiates at the horseshoe dislocation rings and the mixed dislocation regions and extended towards the interior of the Ag nanoparticles. Besides the oxidation occurred in the solutions, the oxidation behaviors of the Ag nanomaterials in atmospheric air have also been studied. Based on the report by Keast by high resolution transmission electron microscopy (HRTEM) observation, an oxidation layer with the thickness of 20- 50 nm could be characterized on the surface of bulk Ag after 10 months' exposure in air.[26] In contrast, the Ag nanoparticles with the size between 50 and 120 nm would rapidly decompose into more nanoparticles with much smaller sizes only after a few days' exposure. Afterwards, the as-

obtained smaller Ag nanoparticles will be sulfurized into Ag_2S. The oxidation behaviors of the Ag nanowires in atmospheric air have also been studied (Figure 2.4).[27] The results show that the oxidation rate of Ag nanowire is slightly higher than the Ag nanoparticles due to the higher defect density and larger amount of twinning and dislocation, which will bring a unstable surface with higher activity.

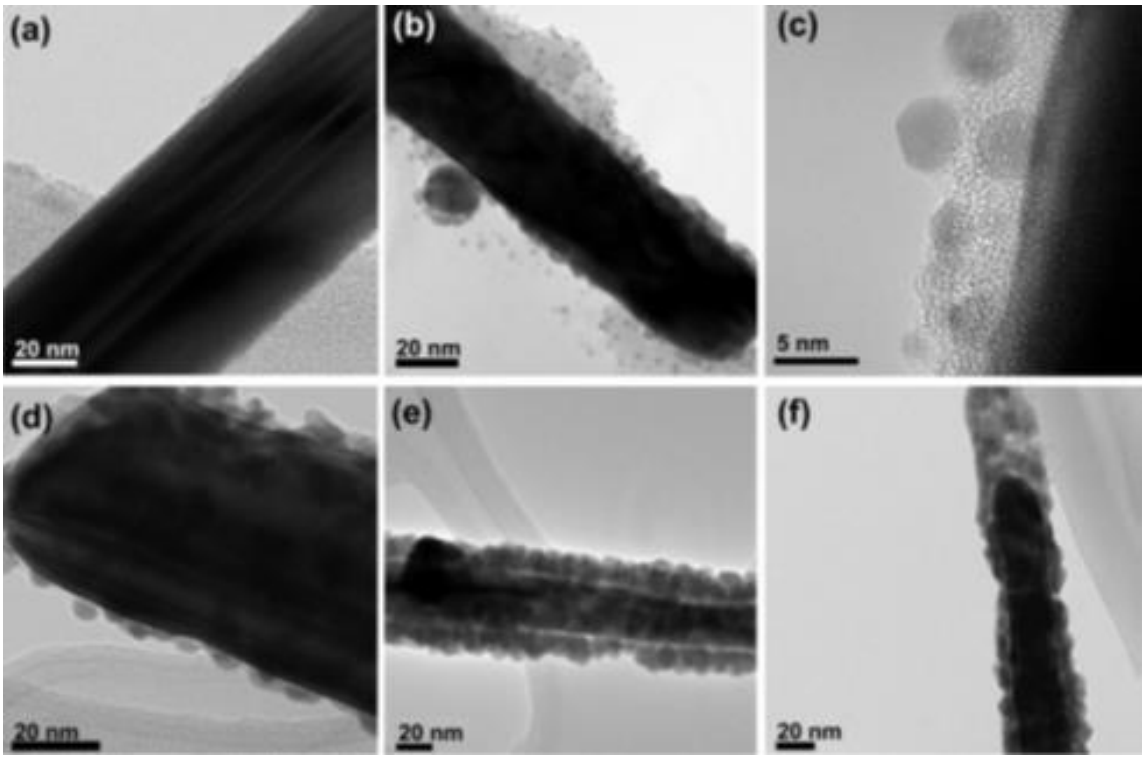

Figure 2.4 TEM images of the same sample at different times after exposure to air at ambient conditions.[27]

2.1.1.2 Electrochemical oxidation of nanoscale active metals

The study of the electrochemical oxidation behaviors mainly focuses on the noble metals and transition metals above since they have exhibit favorable physiochemical properties in a wide range of applications. The results prove that the oxidation process on metallic nanomaterials has a great difference from the bulk metals, which is always associated with the composition, size and structure of the nanomaterials, as well as the surrounding environment. As we know, Al nanoparticles can be used as biomedical field due to its low toxicity. Hedberg et al have study the electrochemical stability of Al nanoparticles in cell

culture medium.[28] The results show that a thin Al_2O_3 passive film can be formed on the surface of Al nanoparticles rapidly to protect them from being further oxidized or dissolved. The oxidation behaviors of Al nanoparticles in air have also been extensively investigated.[29] The research results indicate that the oxidation behaviors of the Al nanoparticles is dependent to the particle size, which can be summarized in Table 2.1. The ratio that the passive film takes in Al nanoparticles is usually above 10 %, which is much higher than that of micron-size Al particles (0.5 %- 2.5 %). Specifically, 70 % of the Al nanoparticles will be taken by the oxide film when the size reaches down to less than 10 nm. Thus, Al nanoparticles with the diameter of 10- 20 nm can hardly exist stably in the air.

As another active metal, nanoparticles of magnesium-based alloy have also been used for the oxidation behaviors study.[30] A similar oxidation process to the Al nanoparticles case has been found on the Mg-based nanoparticles, suggesting its poor anti-oxidation ability in aqueous solutions.

Table 2.1 Calculated oxide layer thickness for aluminum particles.[30]

Particle Diameter, nm	Powder	S_{sp} (BET), m^2/g	Oxide Content, wt %	Particle Density, kg/m^3	Oxide Layer Thickness (φ), nm
10	Aluminum nanopowder	222.222	70	3603	1.78
20		111.111	50	3345	1.73
30		74.074	40	3216	1.78
40		55.556	30	3087	1.54
50		44.444	25	3023	1.5
60		37.037	20	2958	1.35
70		31.746	19	2945	1.47
80		27.778	16	2904	1.34
90		24.691	13	2870	1.22
100		22.222	10	2829	0.99
200		11.111	9	2816	1.76
500		4.444	7	2790	3.33
1000	Aluminum micron-sized powder # 4 (fine fraction)	2.222	6	2777	5.63
10000	Aluminum micron-sized powder # 4	0.222	2	2726	17.90
100000	Aluminum micron-sized powder # 1	0.022	1	2713	88.10
1000000	Aluminum micron-sized powder # 1	0.002	0.1	2701	87.10

Germanium nanowires are playing an important role in semiconductor field and have a promising application prospect in micro-electronics. Like other metals, nanoscale Ge has a higher activity than the bulk counterpart. In dry air, the surface of the Ge nanowires will be rapidly covered by a GeO_x layer to prevent them being further oxidized. However, the GeO_x film is very unstable in aqueous solution, which will be dissolved in few hours. As a consequence, the they can only be used after surface passivation.[31, 32]

2.1.1.3 Electrochemical oxidation of nanoscale transition metals (Ni, Fe)

Compared to the noble metals with relative high ionization potentials, the galvanic series of non-noble metals are more negative, which leads to a higher chemical and electrochemical activity. In fact, the electrochemical oxidation processes on the non-noble metals are much more complicated due to their more valent states and the existence of passivation mechanism et al.

Ni nanoparticles and nanowires have received great attention due to their widely application in magnetic materials,[33] catalysis,[34] new energy resources[35] and medicine et al.[36] As we know, nickel is very stable in atmospheric air and most aqueous solutions ascribed to the formation of a protective passive film on the surface. Unlike nanoscale silver, the chemical stability of nanoscale nickel materials remain excellent.

Our group have successfully fabricated nanoscale Ni sample with needle shape and studied its electrochemical oxidation behaviors in both acid and alkaline solutions.[37] The passive films that formed on the Ni nanoneedle samples after electrochemical treatments have been analyzed on the basis of HRTEM images, which are illustrated in Figure 2.5. The results show that a thin layer that is composed of crystalline NiO is epitaxially grown on the surface of Ni nanoneedle substrate after potentiostatic polarization in 0.1 M H_2SO_4 solution for 1 hour. In contrast, a duel layer structure is observed to be adjacent to the Ni substrate after the polarization in 0.1 M NaOH solution, in which the inner layer also turns out to be epitaxial NiO whilst the outer layer is characterized to be $Ni(OH)_2$ without orientation relationship to the inner layer. As suggested in the paper, the epitaxial NiO layer is formed

probably due to the direct oxidation of the Ni substrate and the formation of the disordered $Ni(OH)_2$ layer is due to the re-deposition of the dissolved $Ni(OH)_2$ particles in the solution back to the nanoneedle sample.

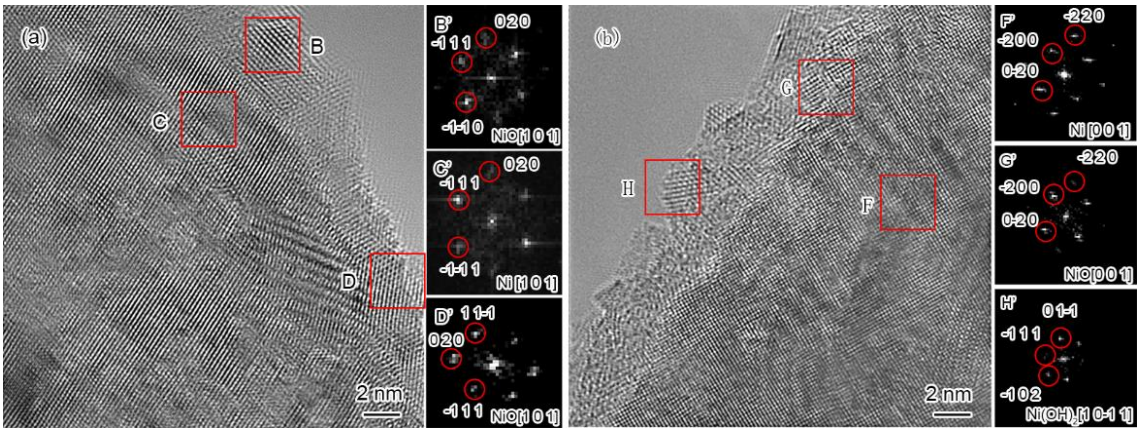

Figure 2.5 HRTEM images of nickel nanoneedle samples after electrochemical polarization in 0.1 M H_2SO_4 solution (a) and 0.1 M NaOH solution (b), respectively.[37]

During the past years, nano zero-valent iron (nZVI) have been broadly used in environmental purification and catalysis et al.[38-41] Since the practical application environments of the nZVI are usually aqueous solutions full of oxidative ions, dissolved oxygen and corrosive ions, the oxidation on nZVI will greatly influence its stability. According to the study by Sarathy,[42] nanoscale nZVI particles experience an activation period in the first 2 days in the anaerobic deionized water and tend to become stabilized. The mechanism involves the passivation of the nZVI particles, the breakdown of Fe(III) passive film and the re-passivation process. In another study of the electrochemical oxidation behavior of nZVI nanoparticles, their stability in both aerobic and anaerobic aqueous solutions are compared.[43] The results show that the nZVI nanoparticles exhibit a better stability in anaerobic environment. The schematic evolution of the nZVI nanoparticles in water has been illustrated in Figure 2.6. In anaerobic water, a core shell structure (i.e. Fe core and FeO/α-FeOOH and β-FeOOH shell) is formed and remain stable after 72 hours' immersion. In contrast, a core-shell structure similar to the case above is also obtained at the first stage (< 1 day). Subsequently, the shell becomes thicker and thicker at the expense of core consumption and results in the decomposition of the core-shell structure and the formation of iron oxide nanoparticles (< 4 weeks), which will totally

transform into the most stable α -FeOOH. Given the several oxidation of nZVI in the media containing oxygen, the applications of nZVI are tremendously limited.

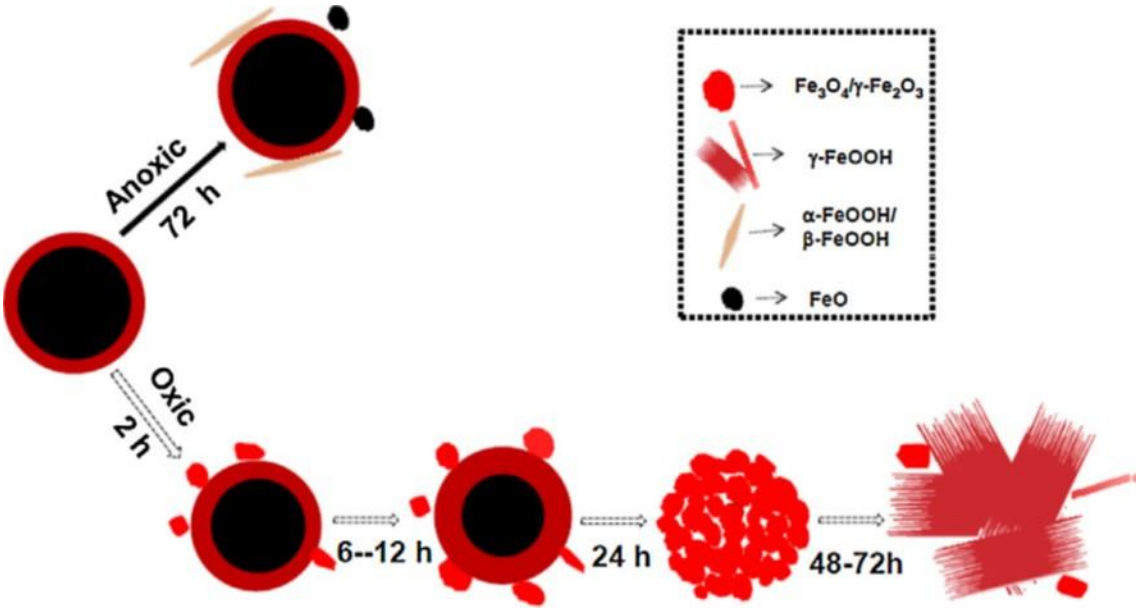

Figure 2.6 A conceptual model on nZVI evolution in water.[43]

2.1.1.4 Electrochemical oxidation of nanoscale Cu

Copper, one of the most commonly used metals, is playing critical roles in electronic devices due to its excellent physical properties. By taking advantages of the high electrical and thermal conductivity, copper nanowires (CuNWs) show promising applications in constructing high performance transparent conductive electrodes,[44] polymer solar cell,[45] chemical nanosensor,[46] lithium ion battery conductive agent[47] and heat dissipation devices.[48] Compared to Ni, the electrochemical passivation on Cu is more complicated due to the involvement of more oxide species, which is similar to the Fe case. Taylor et al[49] studied the electrochemical properties of nanoscale Cu using first principle DFT calculation. The results show that the decrease of the surface coherent energy of Cu nanomaterials would lead to a higher tendency of thermaldynamic dissolution and a drastically negative shift of the dissolution balance potential. A large number of surface atoms with low coordination have a strong absorption of the water, oxygen, hydrogen and hydroxyl ions, which could result in the decrease of the ionization potentials of the surface Cu atoms. As depicted in the potential-pH diagram in Figure 2.7, the equilibirum potential,

active oxidation region and passive region of copper nanomaterials tend to shift negatively compared to the bulky copper. The caculated results above provide solid thermaldynamic evidence for the study of electrochemical oxidation on copper nanomaterials. Besides the caculation study, experimental method has also been adopted to investigate the electrochemical behaviors of nanoscale copper materials. In the immersion experiments conducted by Xia et al, Cu nanoparticles were immersed distilled water for a certain period.[50] The characterization of the nanoparticles after immersion confirms that the composition of the compact passive layer is quite complex, where CuO, $Cu(OH,Cl)_2 \cdot 2H_2O$ and $Cu_2(CO_3)(OH)_2$ have all been detected, which exhibits distinguishable oxidation properties to the Cu particles with micron size.

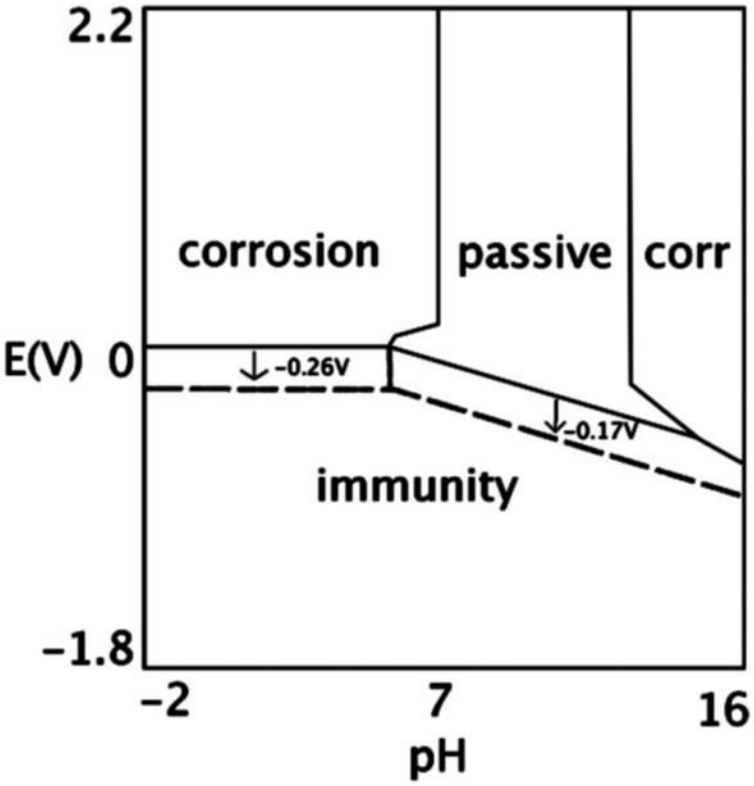

Figure 2.7 A schematic E-pH Pourbaix diagram for copper with modifications.[49]

2.1.2 Cu-based nanomaterials for electrocatalysis

Nanomaterials fabricated from inexpensive metals with earth abundancy have become more and more attractive due to their great potential as favorable alternatives to the traditional ones prepared by noble metals in varieties of applications.[51] Being a 3d

transition metal with promising physical and chemical properties, Cu is considered as one of the desirable substituted options.[52-54] Cu-based nanomaterials are capable of promoting various electrochemistry-related reactions since Cu possesses a wide range of oxidation states, including Cu^0, Cu^I, Cu^{II} and Cu^{III}, which provides the possibility of one- and/ or two-electron pathways in electrochemical reactions.[55] On account of their unique properties and features, Cu-based nanomaterials (Cu, Cu_2O, CuO, $Cu(OH)_2$ and their complex) have been widely applied in electrocatalysis, such as, fuel-cell related reactions, CO_2 reduction and water splitting.[56-58]

2.1.2.1 Cu-based nanomaterials for methanol (ethanol) oxidation

During the past decades, Cu has been regarded as a promising catalyst for the electro-oxidation of organic compounds.[59] Electrodes with Cu_2O, CuO or/and $Cu(OH)_2$ modification can effectively facilitate the electrochemical oxidation of methanol, ethanol, carbohydrates and amino acids et al.[60] The mechanism of electrocatalytic oxidation of organic compounds on Cu nanoparticles in alkaline media has been raised by Xia et al: the oxidation of organic compounds is achieved by the adsorbed ·OH radicals that formed on the CuO layer covered the Cu particles.[59] This process is called incipient hydrous oxide/ adatom mediator (IHOAM) model, which is well-agreed for the explanation of Cu catalysis towards the organic compounds oxidation at low potentials.[61] The elaborate catalytic activity of Cu in alkaline solutions have been discussed in IHOAM model by Burke et al, declaring that the active sites mainly come from the defects site, which produce the energetic adatoms.[62] In terms of nanomaterials, the enhanced electrocatalytic performance can be realized due to the decrease of mean lattice coordination number, leading to a higher surface free energy. As a consequence, the hydrous oxides that formed on the surface of metal nanomaterials surface will serve as mediators in the electrocatalytic process.

Electro-oxidation of organic compounds is regarded as an important path to realize the energy conversion using liquid fuels.[63] Cu-based nanomaterials have been used as favorable catalysts in direct methanol fuel cells (DMFCs) in alkaline media.[64] Cu nanostructures fabricated by electrochemical methods could provide a large surface area

so that an improved electrocatalytic activity is realized. According to the previous studies, there are many factors that can influence the catalytic performance of the nanomaterials. As for copper, the facet-dependent feature has been investigate by Venkatasubramanian et al.[65] By means of CV measurements in alkaline solution containing methanol, the Cu nano-plates and Cu octahedrons exhibit quite different activities towards methanol oxidation, where a 2-fold higher current density has been achieved on the nano-plate Cu electrode, as shown in Figure 2.8. The distinct difference is ascribed to the fact that the exposed facets of Cu nano-plates (1 1 1) and (1 1 0) possess a superior electrocatalytic capability for methanol oxidation than the crystal plate (1 0 0) provided by the Cu octahedrons.

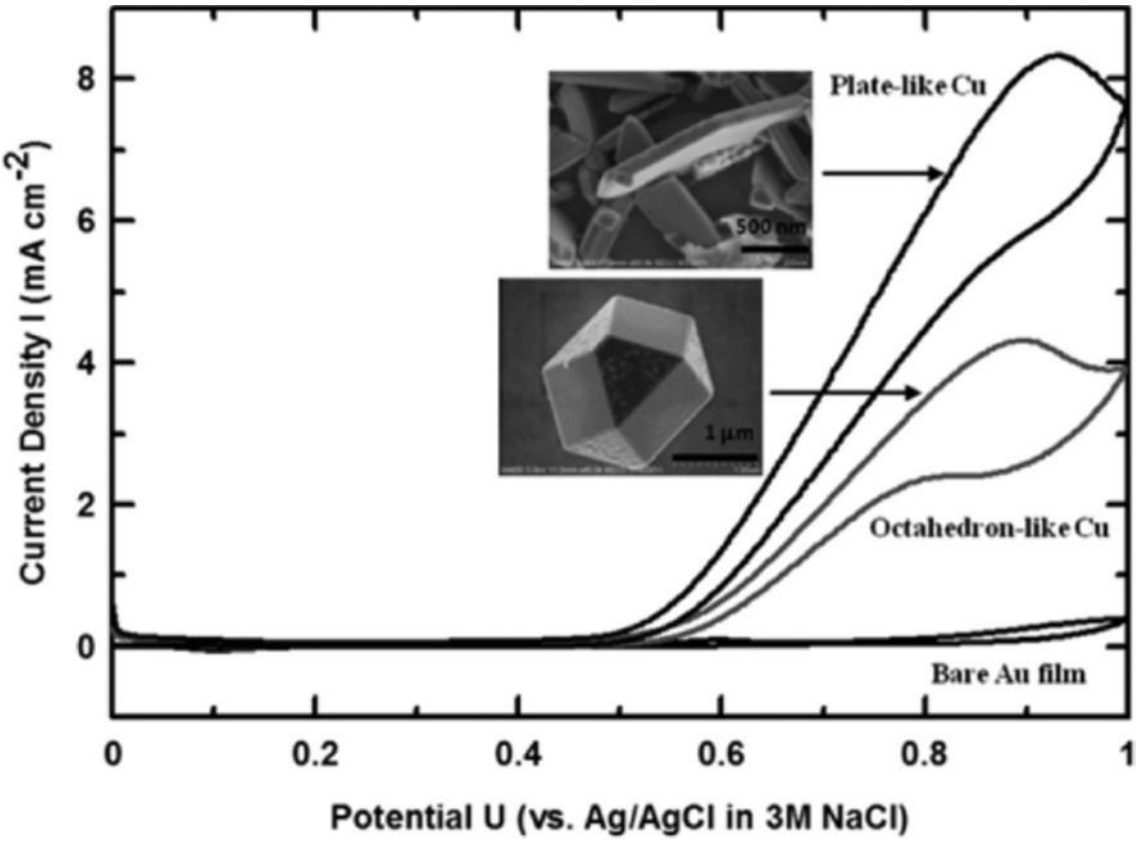

Figure 2.8 CV curves for copper particles in an alkaline electrolyte medium containing CH_3OH (0.25 M) and NaOH (0.1 M) at a scan rate of 10 mV s^{-1}.[65]

The electrocatalytic activity is not only determined by the exposed facet of Cu nanoparticles, but also associated with the correlation of the particles' geometry. Xia et al have study the methanol oxidation performance of the multilaminated Cu nanoparticles

with the preferential orientation [1 1 1] grown on different conductive matrixes.[59] In addition, the combination of a conductive polymer to the Cu nanoparticles could increase the surface active area as well as the charge-transfer rate towards methanol electro-oxidation, leading to an excellent performance of the as-prepared Cu-based structures, where a current density of 196 mA cm^{-2} at 0.838V vs. saturated calomel electrode (SCE) has been achieved.

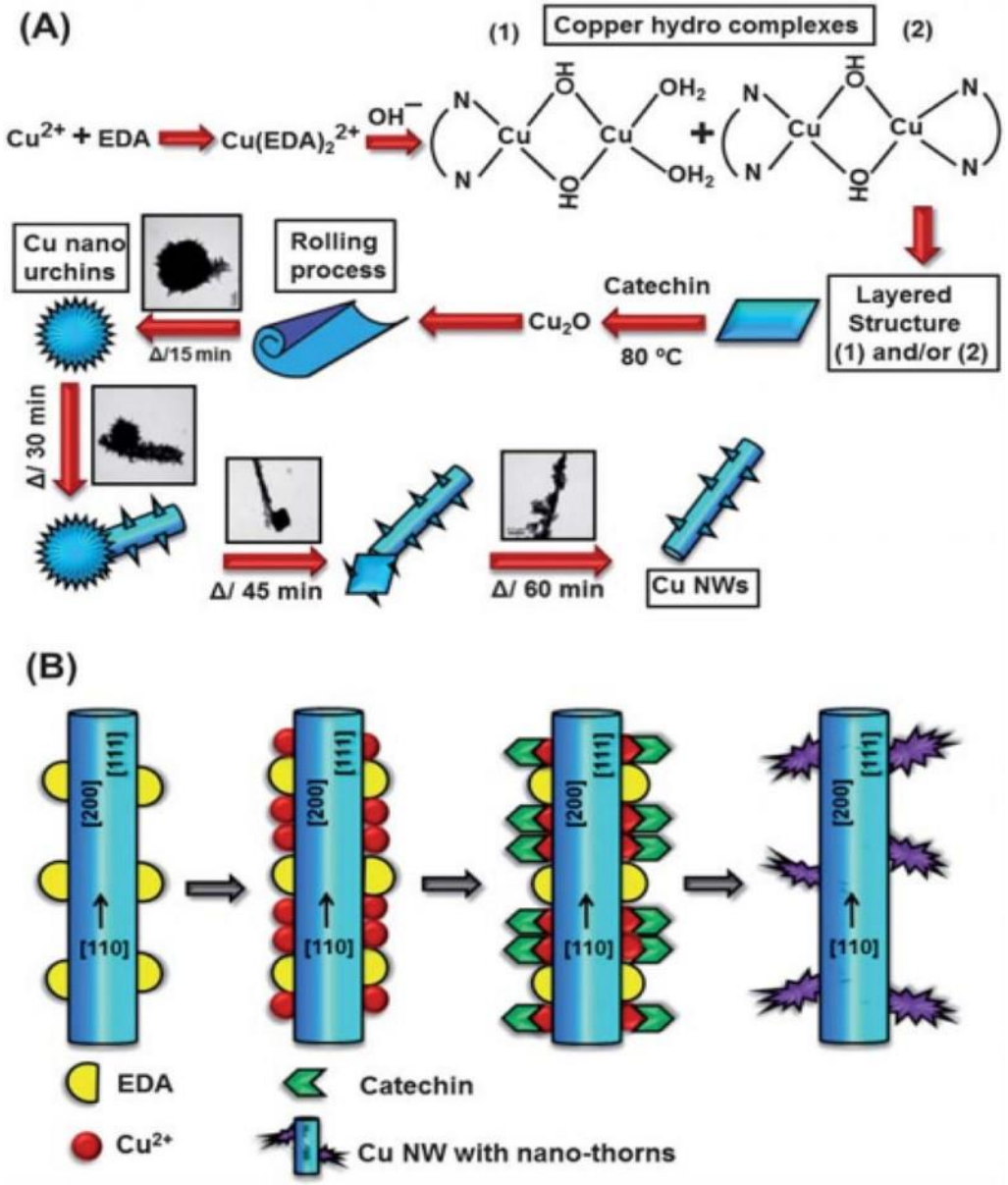

Figure 2.9 Scheme illustrating the growth mechanism of (A) hierarchical Cu NWs and (B) nanothorns in Cu NWs in the presence of EDA and catechin.[59]

Besides the Cu nanoparticles, Cu nanowires (CuNWs) eletrocatalysts have also been widely applied in methanol oxidation. As illustrated in Figure 2.9, Periasamy et al. have prepared CuNWs via a wet chemistry method.[66] Due to the existence of reducing agent catechin, the CuNWs are grown from the nanothorns with (2 0 0) side facets and capped by ethylenediamine (EDA). The as-prepared CuNWs can hybrid with graphene to meet a requirement of lowing charge-transfer resistance in methanol oxidation. As expected, the hybrid catalyst can exhibit a superior methanol oxidation activity than the bare CuNWs with a long-term durability.

Another approach to improve the catalytic activity of Cu is the copper chloride modification.[67] By immerse the polished copper electrode in 0.1 M $CuCl_2$ solution for 20s, a thin layer of CuCl was formed on the surface of copper electrode. The as-prepared CuCl modified copper electrode exhibits a superior activity of methanol electro-oxidation than the bare copper electrode. The better methanol oxidation performance is attributed to the formation of a layer of $(ClCu)_2O$ on the surface of modified copper electrode during the electrochemical oxidation process in 0.1 M NaOH solution through the equation (4) below,

$$2CuCl + 2OH^- \rightarrow (ClCu)_2O + H_2O + 2e^- \quad (4)$$

which is able to provide an efficient oxidation activity of methanol. The study by Liu et al. have indicated that the insoluble surfactant hexadecylamine (HDA) capped on the CuNWs surface will inhibit the methanol oxidation due to the block of active Cu surface (Figure 2.10).[68] In their work, CuNWs with high purity and "clean surface" have been synthesized from the Cu_2O seeds. The results show that the as-obtained CuNWs with abundant (1 0 0) facets can achieve the methanol electro-oxidation at a low overpotential, which is better than the CuNPs with "clean surface" and 6.45 folder higher than the HDA capped CuNWs, which is ascribed to the exposure of more active sites to realize the efficient charge transfer during the electrocatalysis process.

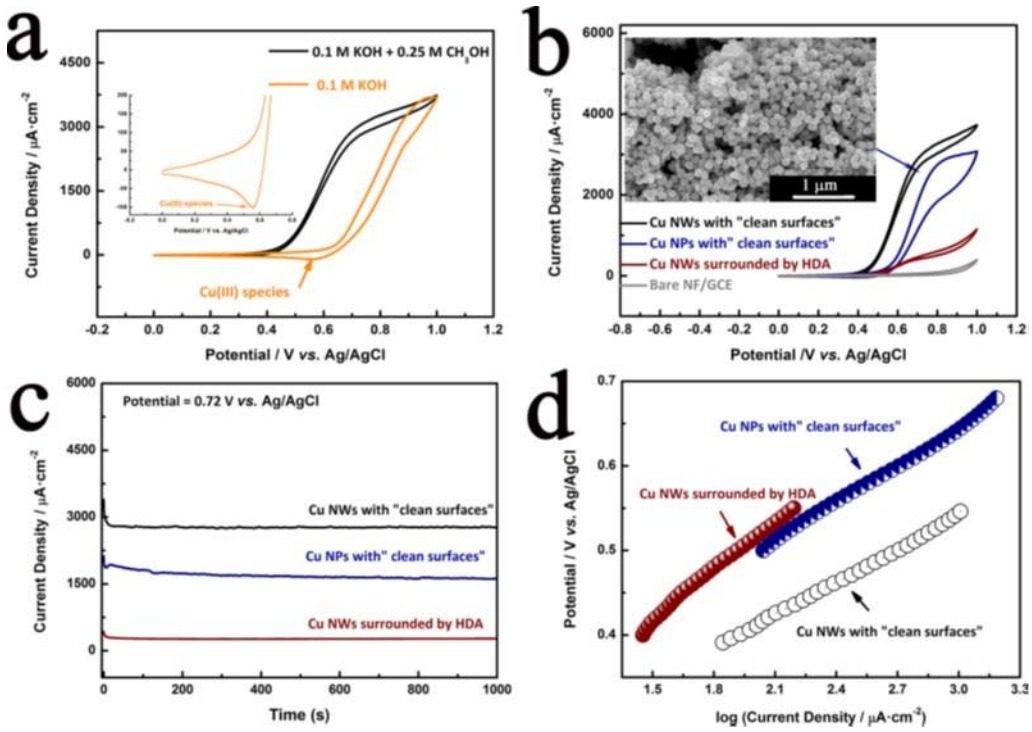

Figure 2.10 Methanol oxidation activities of as-prepared CuNWs with "clean surface", CuNPs with "clean surface" and HDA capped CuNWs.[68]

In order to increase the activity and stability of Cu-based electrocatalyst for methanol or ethanol electro-oxidation, the incorporation of noble metal elements (Pt, Au, Pd et al)has also been proved an effective way.[69-71] Mintsouli et al. have prepared a bimetallic Cu-Pt carbon-supported catalyst through the galvanic replacement of Cu atoms by Pt at room temperature.[72] The obtained core-shell structure (i.e. Pt-rich shell and Cu-Pt core) presents a better catalytic performance of methanol oxidation than the commercial 20% Pt catalyst. This is because the Pt incorporated Pt can effectively remove the oxidation product CO from the poisoned Cu atoms, boosting the overall efficiency of the CuPt catalyst. The electrocatalytic performance of CuPt nanocrystals can also be realized by introducing high-index facets with higher surface area, which has been successfully studied by Zhang et al.[73] As shown in Figure 2.11, screw-like CuPt nanowires with high-index facet (2 2 1) and (3 3 1) and high active surface area have been synthesized and used as electrocatalyst for methanol and ethanol oxidation. The resulted CuPt nanowires exhibit a much better performance than the CuPt nanoparticles.

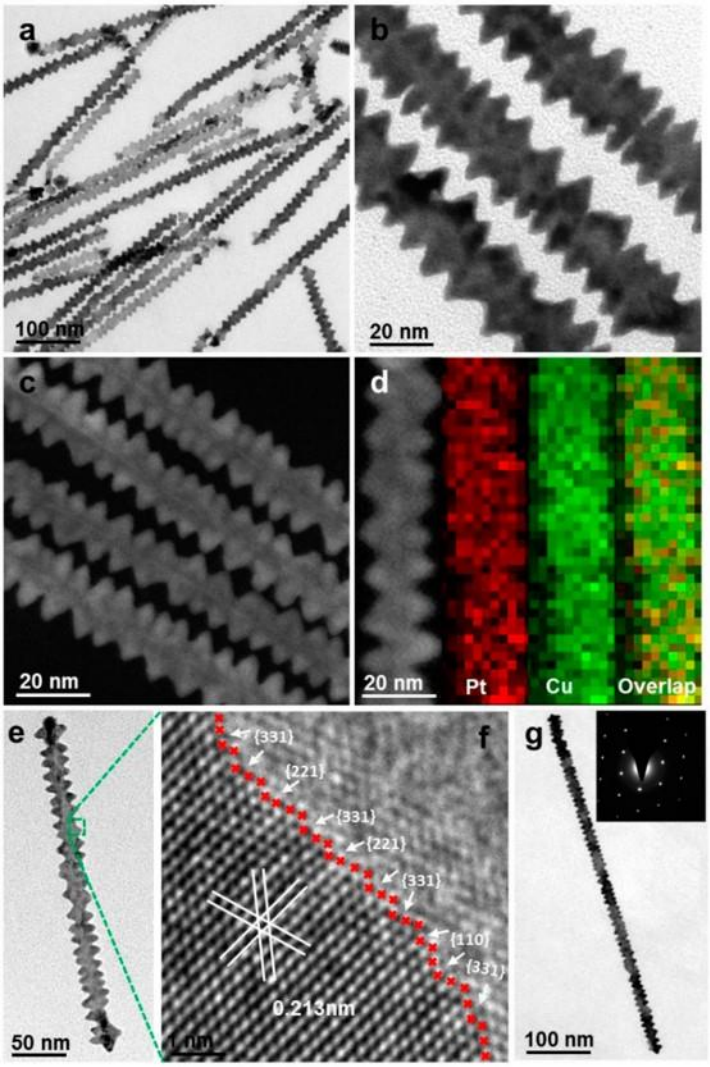

Figure 2.11 Morphological and structural analyses for screw thread-like $PtCu_{1.8}$ NWs.[73]

Another alloying noble element Pd has also been applied to improve the catalytic activity of Cu nanomaterials. A novel Pd decorated CuNWs (Pd@CNWs) catalyst via a hydrometallurgy method by Ren et al, where a 30-50 nm thick Pd shell is coated uniformly on the as-fabricated CuNWs.[70] The performance tests show that the one dimensional Pd@CNWs exhibit a higher catalytic activity and better durability for the methanol oxidation in alkaline solution than the Pd-Cu. The mechanism study reveals that the oxidation rate of the Pd@CNWs catalyst is determined by the first charge transfer step, which is independent to the concentration of CH_3OH or OH^- at all Tafel ranges. Zhao et al. fabricated a CuPd alloy nanosheets (NSs) with hierarchical structure for electro-oxidation of ethanol.[74] Specifically, CuPd NSs were obtained by Cu diffusion into the lattice of as-

prepared Pd NSs, leading to the lattice distortion so that the NSs is wrinkled, followed by the interlacing of the NSs into 3D flower-like nanostructure (Figure 2.12). The as-fabricated 3D CuPd electrocatalyst exhibits a selective oxidation of ethanol into carboxylate with an enhanced activity due to the abundant surface active sites on the nanosheets, the favorable conductivity of the metallic structure and the synergistic effect between Cu and Pd to improve the absorption behaviors for catalysis.

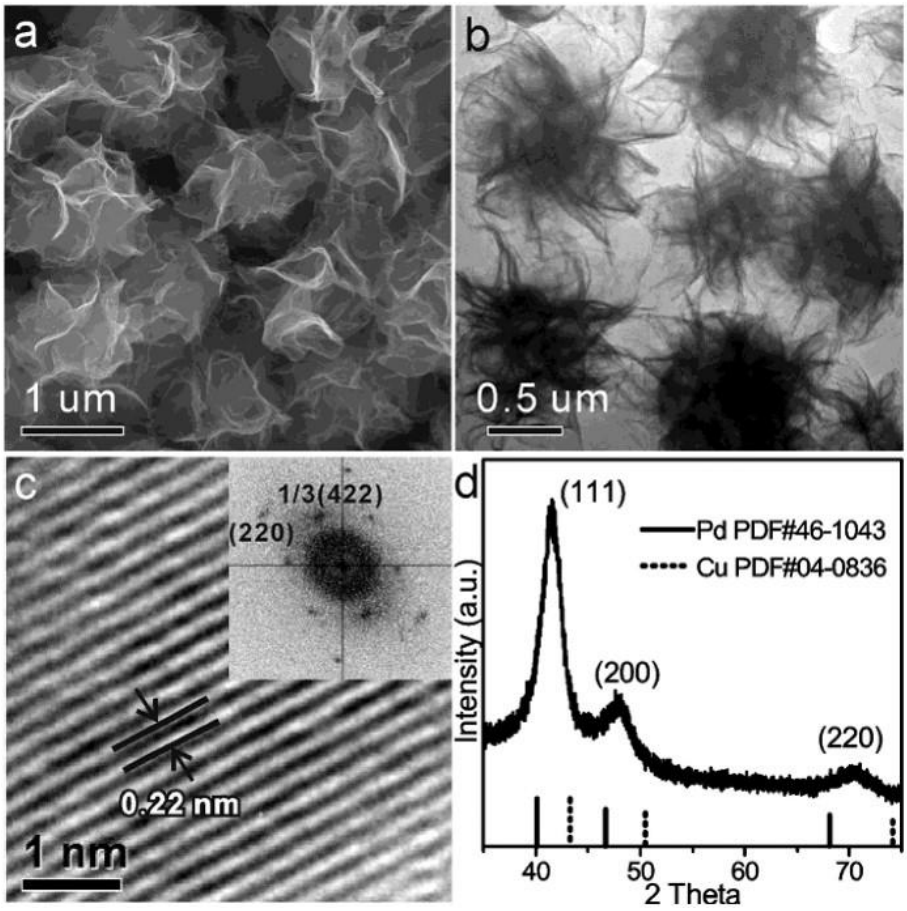

Figure 2.12 a) SEM image of 3D CuPd NSs, b) TEM image, c) HRTEM image and the corresponding FFT pattern image, d) XRD pattern of the 3D CuPd NSs.[74]

2.1.2.2 Cu-based nanomaterials for O_2 and CO_2 reduction

In fuel cells or metal air batteries, the reduction of oxygen process may act as a detrimental factor in limiting the overall catalytic efficiency.[75, 76] Awad et al. have fabricated a Cu NPs decorated Au electrode using a electroreduction method towards the electrocatalysis of oxygen reduction reaction (ORR).[77] The as-deposited electrode shows a high ORR

activity due to the synergistic effect between the decorated Cu NPs and the Au (1 0 0) substrate, which is comparable to the Pt catalyst. Copper-silver alloys have also been developed as the catalysts for oxygen reduction reaction with a similar performance of platinum catalysts.[78, 79] Based on the study by Wu et al, CuAg nano-alloys have a promising potential as the air cathode in zinc-air batteries.[80] A pulsed laser deposition method was employed to prepare a hierarchical structure, where crystalline CuAg nanoparticles are embedded into the amorphous Cu thin film., On the basis of DFT calculations, Cu doping atoms into the core or onto the surface of the CuAg cluster could change the mulliken charge of silver atoms, which is shown in Figure 2.13. Among the CuAg nano-alloys with different Cu/Ag ratios, $Cu_{50}Ag_{50}$ exhibit the best performance for ORR in alkaline solution. In primary zinc-air batteries, the maximum power density 86.3 mW cm^{-2} is also obtained from the $Cu_{50}Ag_{50}$ catalyst with the cell voltage of 0.863 V.

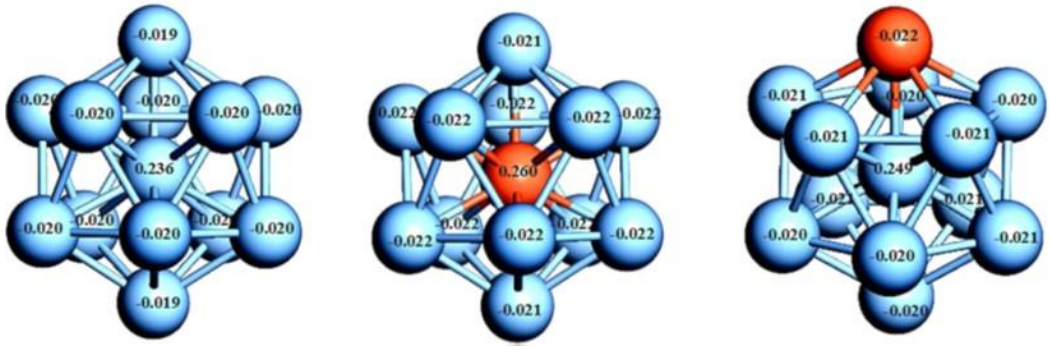

Figure 2.13 Mulliken atomic charge of the Ag_{13}, $Ag_{12}Cu$(Cu-core), and $Ag_{12}Cu$(Cu-shell) structures.[80]

The introduction of metal ions into carbon-based materials is regarded as a promising approach to improve the catalytic activities of ORR.[81, 82] Cu nanomaterials have been successfully immobilized into various carbon-based materials (amorphous carbon, carbon nanotubes and graphene et al) for the electrocatalysis of oxygen reduction reaction.[83, 84] Goenaga et al. developed a pyrolysis method to prepare a nitrogen-copper co-doped carbonaceous material as the electrocatalyst for ORR.[85] An catalyst consists of encapsulated Cu-nanoparticles with nitrogen-doped graphite (Cu@ onion-like N-C) as the core-shell structure was fabricated by Shao et al, as shown in Figure 2.14.[84] The results show that the best ORR activity and stability can be achieve by CuCN-650 (small-sized Cu

nanoparticles coated with a few-layer N doped carbon shell), which is comparable to the commercial Pt/C catalyst in alkaline solutions. The high performance of the Cu@ onion-like N-C catalyst is ascribed to the synergistic effect between the Cu core and the N-doped carbon shell, where the encapsulated Cu nanoparticles could donate the electronic charges to the outer shell for electrocatalysis.

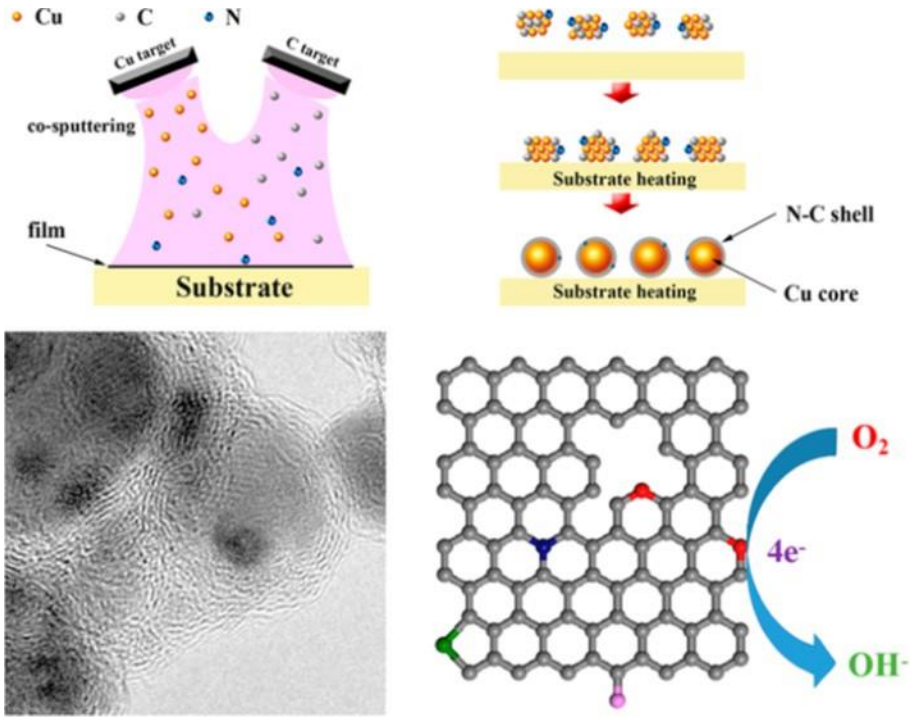

Figure 2.14 Schematic of the growth process of Cu@onion-like N−C during magnetron sputtering.[84]

For the individual Cu NPs with alloying or doping, the intrinsic catalytic activity for oxygen reduction reaction have also been investigated, in which a colloidal solution coupled with Cu nanoclusters was successfully applied.[86] Although the Cu nanoclusters are covered with capping agent, their intrinsic activity can also be demonstrated. Additionally, the doping of Cu into inorganic catalysts, including MnO_2 and TiO_2, has also been proved to be an efficient path to improve their ORR activity.[87, 88]

The electrocatalytic reduction of CO_2 to organic compounds as liquid fuels is one of the promising ways in renewable energy generation.[89] Cu is among the ideal catalysts with

earth abundancy and low cost that can facilitate the electrochemical reduction of CO_2 with highest selectivity for the liquid fuels.[90] However, the required overpotential of Cu to drive the CO_2 reduction is high due to the current losses in the reduction process, which is caused by the competition to the hydrogen evolution reaction (HER) from the aqueous solutions.[91] HER process usually overwhelms the CO_2 reduction reaction at low overpotentials, leading to a great loss in overpotential to be compensated, which is much higher than the tested materials (Figure 2.15). As a consequence, it is a crucial task to realize the CO_2 readuction over H_2 evolution in aqueous media.

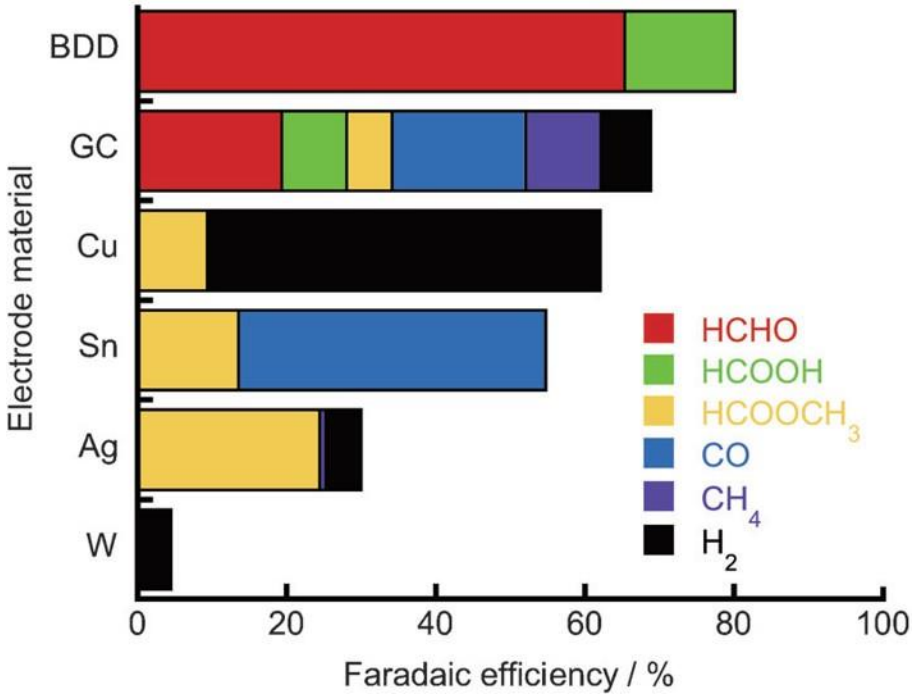

Figure 2.15 Faradaic efficiency of the products generated by the electrochemical reduction of CO_2 using various electrodes in a MeOH electrolyte.[91]

Li et al. have investigated the electrochemical reduction of CO in aqueous solution using Cu nanoparticles prepared by electrochemical and chemical reduction of Cu_2O nanoparticles, respectively.[92] The results show that the generated organic compounds include acetate, ethane, ethanol, ethylene and propanol, which are mainly catalyzed at the grain boundaries of the Cu nanoparticles. Based on the work above, it is noteworthy that the fine fabrication of Cu-based nanoparticles with effective grain boundaries can enhance their catalytic activities for electrochemical CO_2 reduction.[93] Fabricating Cu nanoparticles

through the reduction from Cu_2O is regarded as a promising method since it can bring about a rough surface with sufficient active sites.[94] The approach above would reduce the CO_2 to CO & HCO_2H at low overpotentials and C-2 hydrocarbons at a more negatively potential -0.6 V (vs RHE).

The mechanism of Cu catalysts driving CO_2 to ethanol and hydrocarbons are still to be explored. Several works based on theoretical study have tried to explain the specific process of electrochemical CO_2 and CO reduction on the surface of Cu-based catalysts.[95, 96] Nevertheless, most of the works only take the ideal surfaces without defects or grain boundaries as the study objects, where many actual conditions were not included in the practical electrocatalysts.

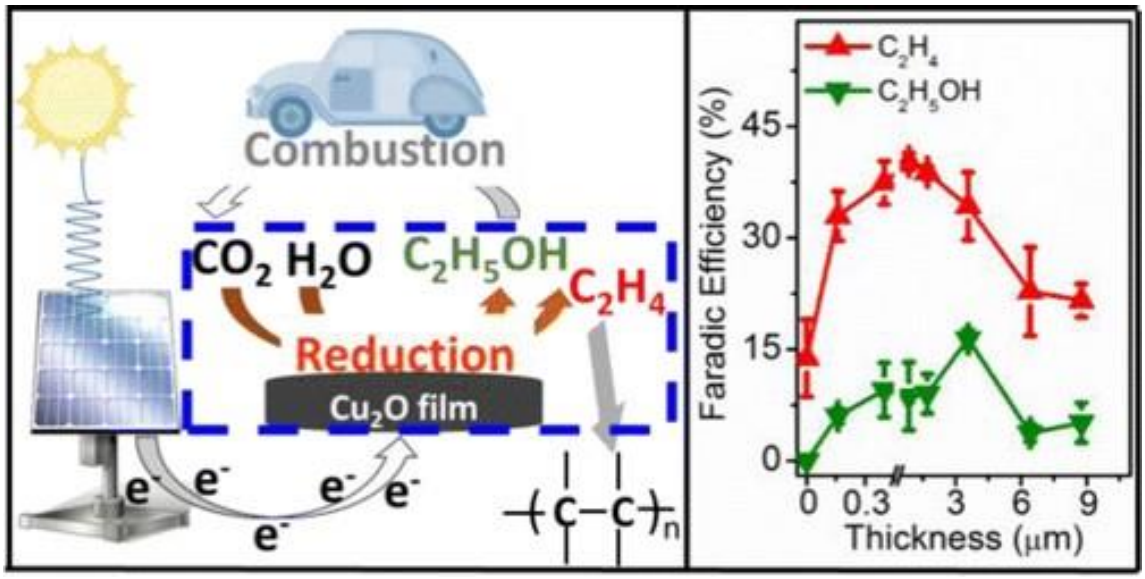

Figure 2.16 The correlation between the faradic yield of ethanol and ethylene with the thickness of the Cu_2O layer.[97]

As mentioned above, the selectivity of CO_2 reduction have been proved to be realized on copper-based catalysts. Based on the research of Ren et al, the faradic yield of ethanol and ethylene that are two main products of CO_2 reduction process is proportional to the thickness of the Cu_2O film on the Cu substrate (Figure 2.16).[97] To be more specific, the eletrocatalyst above could show the high selectivity for the C-2 products at an applied potential of -0.99 V vs. RHE when the thickness of the copper oxide film is between 1.7-3.6 μm. Meanwhile, the yield of major product ethylene was as high as 34- 39%, which is

more than twice than that of ethanol. Besides, there was less than 1 % methane generated under the condition above. The copper oxide film was characterized to be reduced to copper particles after the eletrocatalytic process under the intense reduction current. In addition, they also claimed that the Cu (0) phase act as the active sites for CO_2 reduction even though the exposure surface is copper oxide.

The facet-dependency of copper catalyst has been verified by Roberts et al.[98] In their research, copper cubic crystals have been used for the CO_2 reduction. The results showed that these cubic Cu crystals preferred to the production of C-2 products compared the polycrystalline Cu films. Furthermore, single-crystalline copper films with the planes of (1 0 0), (1 1 1) and (2 1 1) were also employed to evaluate their catalytic effects in comparison with that of the Cu cubes. The results indicated that the Cu cubes with more (1 0 0) surface exposure exhibited a better selectivity for the C-2 products than those with close-packed (1 1 1) plane and the (2 1 1) with high steps.

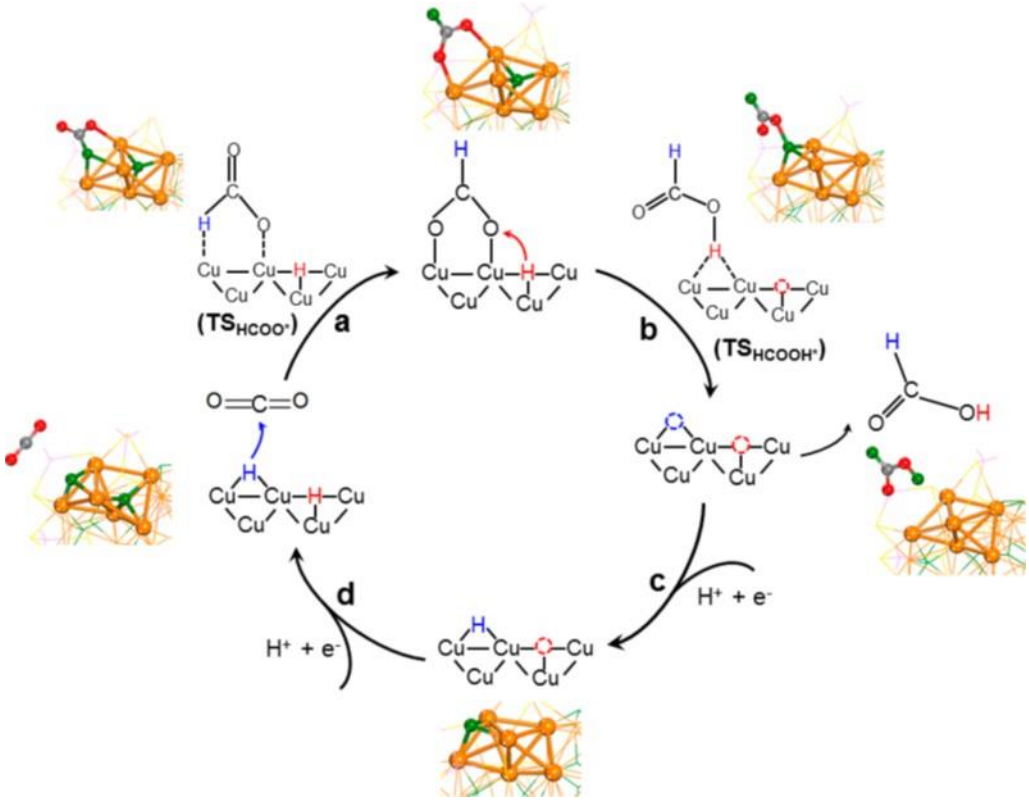

Figure 2.17 Overall mechanism of HCOOH formation from CO_2 reduction on $Cu_{32}H_{20}L_{12}$ via the lattice-hydride channel; the structures of the key intermediates and transition states are shown.[99]

The mechanism of CO_2 reduction on nanostructured copper has also been investigated by Tang et al. by using Cu-hydride nanocluster as the catalyst.[99] Similar to the cube crystals above, the Cu-hydride nanocluster exhibited a unique selectivity at low overpotentials. The DFT calculations further predicted the critical role of the Cu-hydride nanocluster with negative charges in the selectivity behavior for CO_2 reduction, producing HCOOH at a low overpotential. The mechanism of the HCOOH formation was summarized in Figure 2.17: CO_2 is reduced to HCOOH by the surface hydrides first, then the caused hydride vacancies will be regenerated by the proton reduction of the electrochemical process. The possibly competitive hydrogen evolution was also calculated to be much weaker than the HCOOH formation process at low overpotentials, which was testified by the experiments as well. The HER only overwhelmed the reduction process at higher overpotentials.

2.1.2.3 Cu-based nanomaterials for water splitting

Photoelectrocatalytic water splitting one of the most important applications of copper-based nanomaterials, especially Cu_2O with semiconductor properties. Zhao et al. have developed a Cu/Cu_2O layer as an efficient hydrogen evolution catalyst in the solution mediated by phosphate ions, where a very low overpotential of 30 mV was achieved[100] In order to improve the photoelectrochemical hydrogen evolution activity of Cu_2O, Morales-Guio deposited an amorphous molybdenum sulfide catalyst and a Ni-Mo catalyst to catalyze HER under sunlight in 1 M KOH media.[101] The as-prepared photocatalyst was able to generate a photocurrent density of – 6.3 mA cm^{-2} at the reversible hydrogen evolution potential, which is one of the highest values reported for a metal oxide photocathode covered with catalysts consisting of earth-abundance elements. In another work by Luo et al, Cu_2O nanowires were firstly grown on the conductive substrate of fluorine-doped tin oxide, then a uniform and protective layer containing nanoscale p-n junction were finely fabricated on the surface of Cu_2O nanowires as a photocathode for hydrogen evolution under solar irradiation (Figure 2. 18).[102] The as-synthesized catalyst could deliver a photocurrent density as high as 10 mA cm^{-2} with a high stability of more than 50 h.

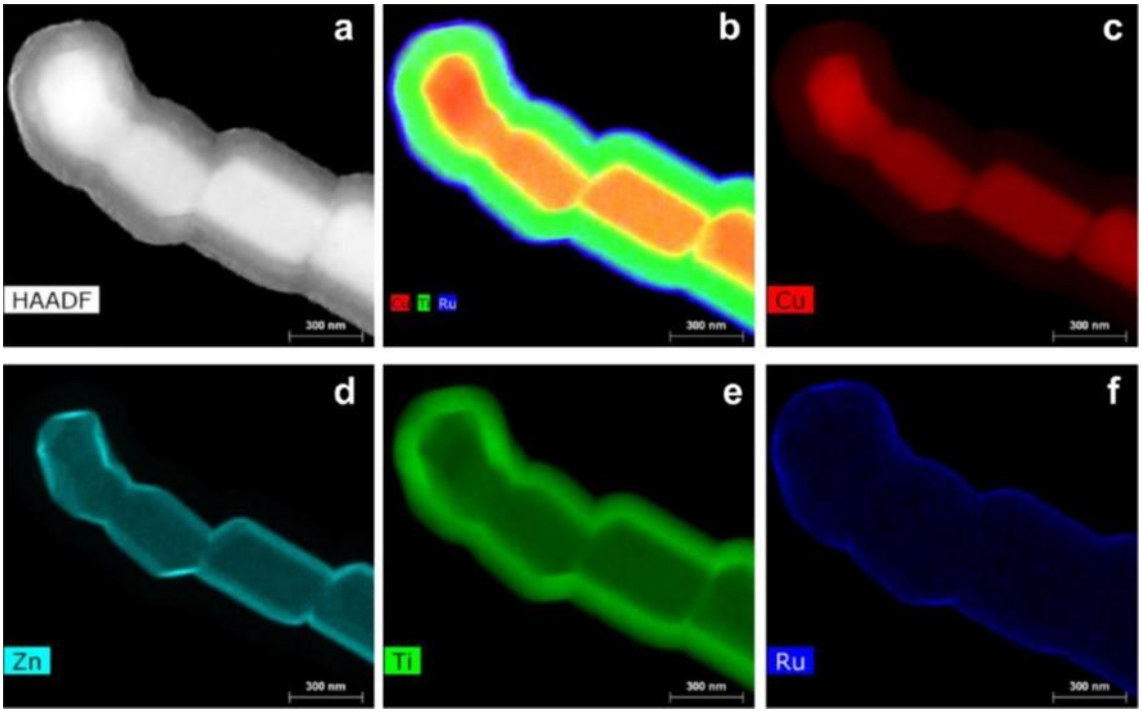

Figure 2.18 TEM and EDX characterization of the Cu_2O NW with overlayers.[102]

Dubale et al. developed a Cu_2O/CuO heterostructure modified with CuS as a highly efficient photocathode for solar driven hydrogen evolution.[103] The heterostructure was fabricated using an in situ approach: a Cu_2O/CuO layer was firstly electrodeposited on the Cu substrate, followed by ion layer adsorption and reaction (SILAR) method. The as-prepared catalyst could provide an excellent photocurrent density of -5.4 mA cm^{-2}, which is more than 2.5 times than the care Cu_2O/CuO catalyst at 0 V vs. RHE (reversible hydrogen electrode). Furthermore, the photocurrent density were boosted to -5.7 mA cm^{-2} with the additional decoration of Pt due to the suppression of eletron-hole recombination. The remarkable photocelectrocatalytic performance is ascribed to the bicatalytic effects as well as the synergistic effect of a heterojunction in light absorption and charge separation. The illustration of band energy levels and charge transfer for the heterostructural photocathode is shown in Figure 2.19. Qi et al. found that the modification of Cu_2O by layered double hydroxides (LDHs) could also improve the photoelectrochemical hydrogen production.[104] The as-obtained Cu_2O/NiFe LDH electrodes could provide a high photocurrent density at -0.2 V vs Ag/AgCl attributed to the enhanced electron transfer rate and an appropriate energy level alignment.

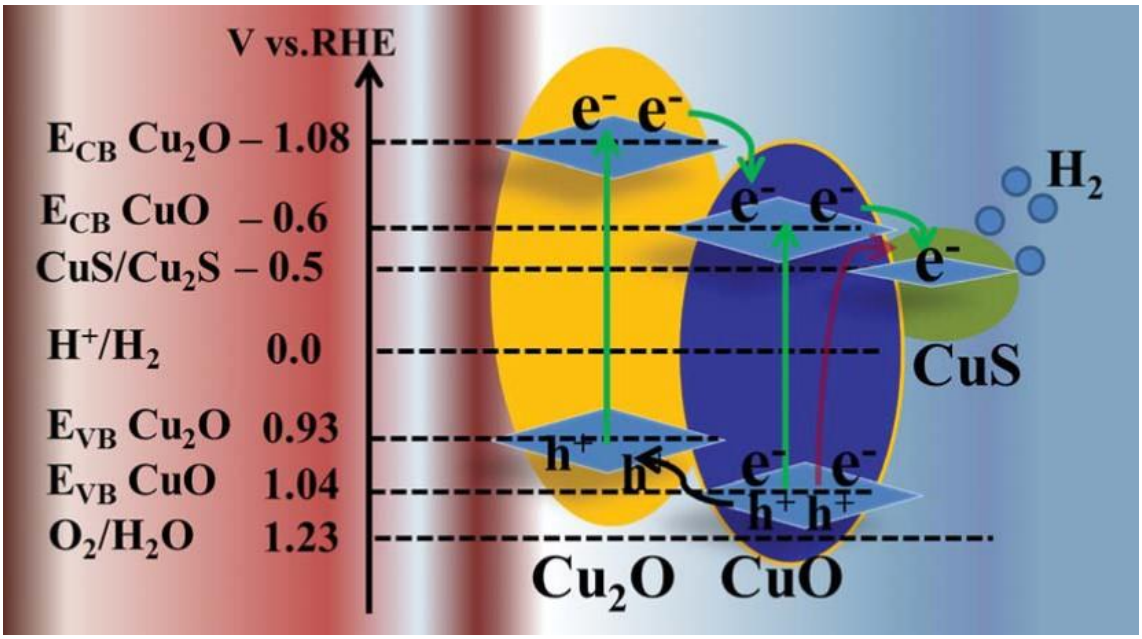

Figure 2.19 Schematic illustration of band energy levels and charge transfers for the Cu2O–CuO–CuS photocathode.[104]

Cu-based nanomaterials have long been used as bifunctional electrocatalyst for both hydrogen evolution reaction and oxygen evolution reaction in the water splitting processes. $Cu(OH)_2$-CuO layer that synthesized by electrochemical deposition has been evaluated as the catalyst for hydrogen evolution reaction in a weak basic solution at pH 9.2.[105] The results showed that the catalyst above can provide an onset overpotential of 450 mV for HER.

Cu-based catalyst with superior HER activity than platinum could also been fabricated through the alloying strategy. Lu et al. have successfully prepared a hierarchical porous Cu-Ti catalyst for high-efficient HER although the HER activity for individual Cu and Ti are both weak.[106] Compared to Pt/C catalyst, the hierarchical porous Cu-Ti exhibited a similar onset potential for hydrogen evolution. However, the hierarchical porous Cu-Ti catalyst presented a better activity when the potential went to more negative values. As shown in a volcano pot of Figure 2.20, the position of the catalytic center for HER is the key point to achieve a higher activity than platinum, which is dependent to the Ti concentration.

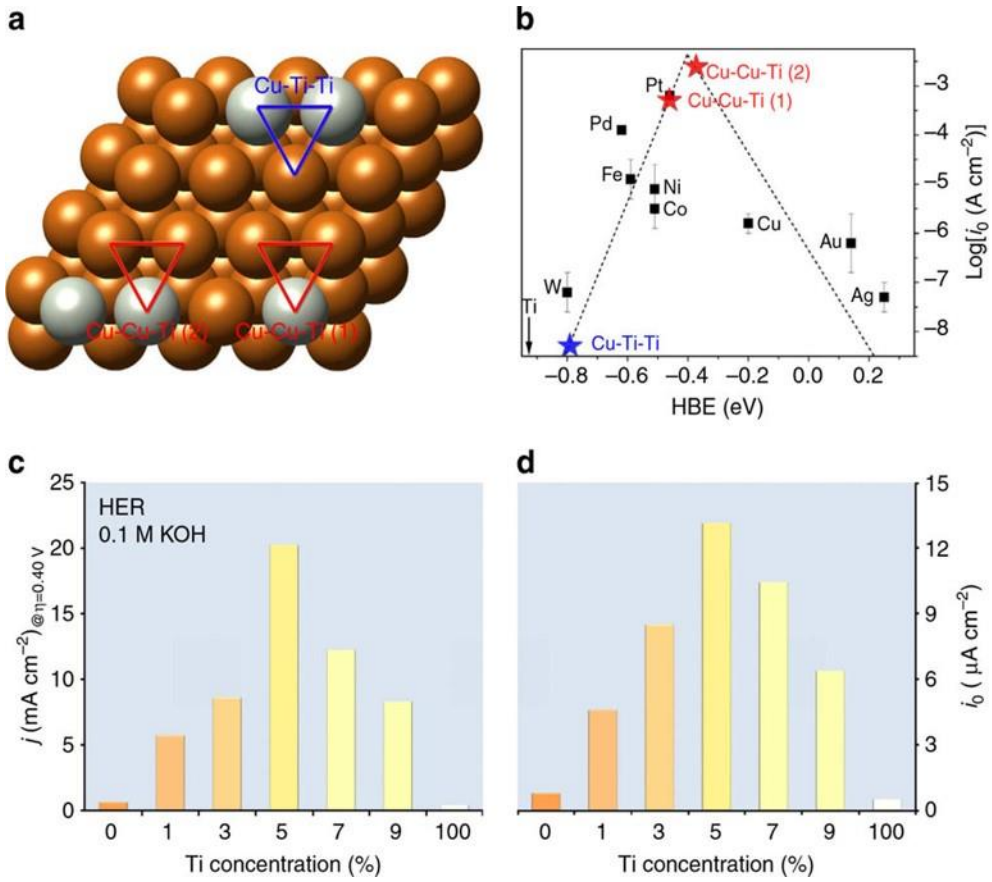

Figure 2.20 Computational studies. (a) Proposed activity sites composed by Cu and Ti. (b) Corresponding hydrogen-binding energies of the proposed active sites in a volcano plot. (c) HER activities and (d) exchange current densities obtained for Cu−Ti alloy surfaces as a function of the Ti content in the alloy.[106]

Unlike the noble metals, the copper catalyst with zero valent cannot be applied in OER since they will be easily oxidized under anodic conditions.[107] However, the active materials to drive the oxygen evolution reaction is Cu (III) and Cu (IV) species on the surface of the Cu-based eletrocatalysts.[108] Stable Cu-based catalysts must be developed to prevent the degradation of the metallic copper in the aggressive electrolytes. Toparli et al. in situ studied the electrochemical behaviors of the Cu catalyst under transpassive conditions in alkaline solution using electrochemical measurement coupled with Raman spectroscopy, photoluminescence spectroscopy and spectroscopic ellipsometry.[109] The results indicated that the thickness of the copper oxide film on Cu surface experienced an initial increase beyond the OER onset potential and the >10 nm oxide layer would dropped

to <5 nm when the overpotential reached around 400 mV. Meanwhile, copper oxide species CuO, Cu_2O and Cu_4O_3 were all characterized by Raman spectroscopy (Figure 2. 21) since the onset of OER. In addition, strong photoluminescence was observed at 1.55 eV with the thickness drop of the oxide film, suggesting that singly charged oxygen vacancies V_O^+ were formed at this stage, which indicated the transpassive dissolution of the oxide film with n-type semiconductive properties due to the defect formation.

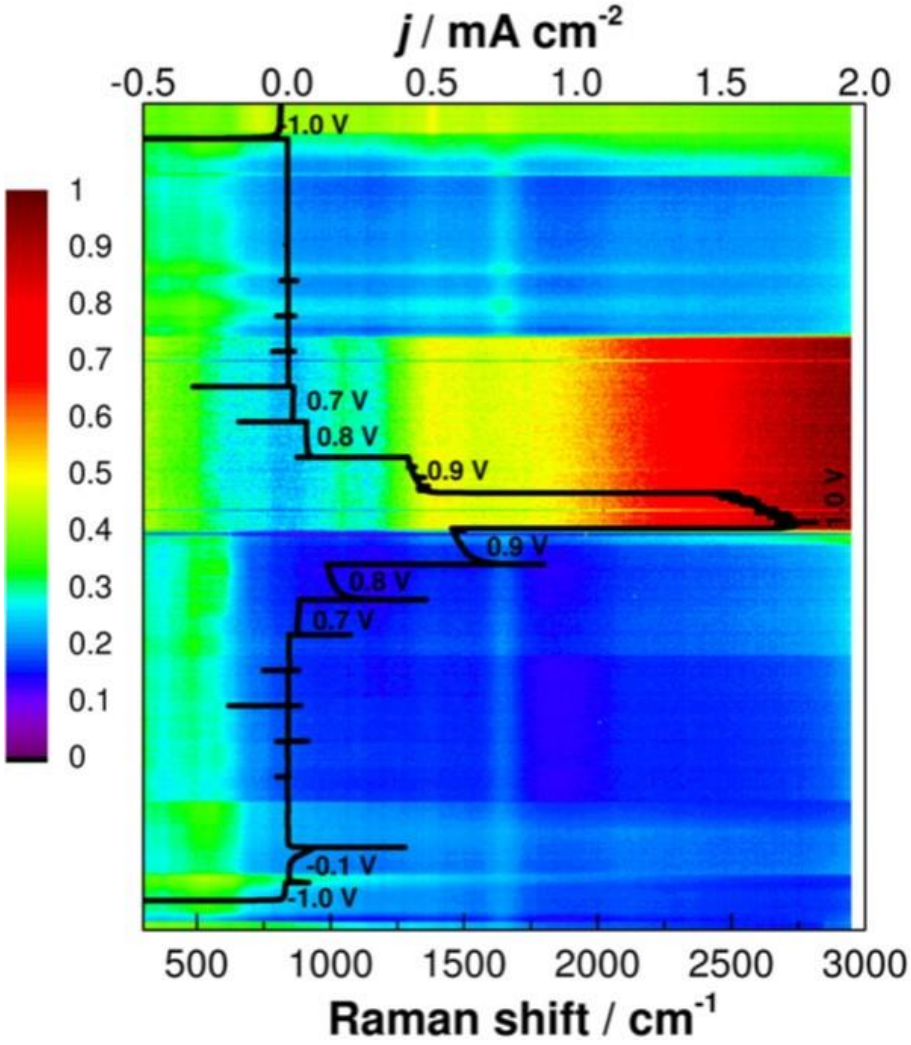

Figure 2.21 Color-coded Raman and PL spectra (excitation: 633 nm / 1.96 eV) recorded during CA experiments, superimposed with current density data.[109]

Given that bare copper nanomaterials are not suitable for the electrocatalysis of oxygen evolution reaction ascribed to their instability in aqueous solutions. Cu oxide species CuO and $Cu(OH)_2$ et al. have been extensively studied for their potentials as electrochemical

catalysts for OER. Yu et al. synthesized a copper oxide-based thin film using electrodeposition from Cu^{2+} contained borate buffer solution for oxygen evolution reaction.[110] The as-obtained Cu-B_i thin film presented a high activity for OER with a long-term stability (1.2 mA cm^{-2}, 1.3 V vs. NHE for 10 h) in borate buffer solution (pH 9). Liu et al. have in situ fabricated a low-cost copper oxide thin film using a one-step approach.[111] The as-prepared copper oxide film exhibited a favorable activity for OER catalysis in 1.0 M KOH solution, where a current density of 1 mA cm^{-2} and 10 mA cm^{-2} could be met at the overpotential of ~ 370 mV and ~ 475 mV, respectively. In addition to copper oxide, copper hydroxide can also serve as a cost-effective and efficient electrocatalyst for oxygen evolution reaction in alkaline solutions.[112] The measured results indicated that a current density of 0.1 mA cm^{-2} could be achieved by the as-synthesized $Cu(OH)_2$ catalyst with a Tafel slope of 78 mV dec^{-1} in the electrolyte with the pH of 9.2.

Compared to metallic copper, the electrical conductivity of bare copper oxide species appear to be much poorer. Thus, hybridization of copper oxide with conductive materials seems a promising path to solve the issue above. Du et al. prepared a thin film consisting of CuO and $Cu(OH)_2$ on Cu using deposition.[108] This protective thin film not only prevented the corrosion of the Cu-based catalyst, but also exhibited a good electrocatalytic activity toward the water oxidation, where a current density of 10 mA cm^{-2} was achieved at an overpotential of 580 mV. Furthermore, the authors also claimed that the addition of concentrated CO_3^{2-} in the electrolyte can effectively prevent the electrochemical corrosion of the Cu-based catalysts. Inspired by the work above, Cu-based nanorods with core-shell structure (i.e. Cu core and CuO/ $Cu(OH)_2$ shell) were fabricated for the electrocatalysis of oxygen evolution reaction by Cheng et al.[113] By means of electrochemical anodization of metallic copper foil followed by the chemical reduction process, abundant copper nanorods were fabricated on the Cu foil. The subsequent anodic oxidation of the as-prepared electrode could lead to the formation of the core-shell structure. In the electrocatalysis measurement, a current density of 10 mA cm^{-2} could be reached at an overpotential of 417 mV. In addition, the durability test indicated that the as-prepared electrode was able to provide a stable catalysis for more than 24 h in the alkaline electrolyte. Carbon materials (amorphous carbon, carbon nanotubes and graphene et al.) are also regarded as an excellent

materials to increase the conductivity of hybrid catalyst with transition metal oxides. Andersen et al. developed a CuO/CNTs composite for water oxidation in alkaline media, which exhibited an enhanced catalytic activity than the care CuO nanoparticles in alkaline solution.[114]

2.2 Questions to Answer Based on Literature

As discussed in the literature review above, extensive efforts have been devoted into the mechanism study of the electrochemical oxidation behaviors of metallic nanomaterials and the synthesis of copper-based nanomaterials in electrochemistry-related applications. However, there are still questions to be answered as followed:

First, the electrochemical oxidation processes of bulk metallic materials (Cu, Ni et al.) have been studied at nanoscale in aqueous solutions and some controversies on the composition and structure of the oxidation layers have been clarified by using direct TEM observation. Although the tips of the needle-shape samples are nanoscale, the working electrodes in the electrochemical measurements are actually bulk materials but not real nanomaterials. Thus, it is not convincing to describe the electrochemical oxidation behaviors using the results above. Experiments and characterization on real metallic nanomaterials should be conducted to reveal the electrochemical oxidation process on metallic nanomaterials. On the other hand, although the growth rate of the oxidation film on bulk metals in atmospheric environment have been extensively studied, similar experiments on nanoscale metals, such as copper, have not been carried out.

Second, the metal samples that are used in the electrochemical measurements usually possess a smooth and homogeneous surface, which leads to the neglect of many other factors (morphology, structure et al) that can influence the electrochemical oxidation processes on the metals. Therefore, it is necessary to perform electrochemical measurement on nanoscale copper materials with hierarchical structure and inhomogeneous surface to explore their oxidation behaviors in aqueous solutions to compare with the homogenous copper nanomaterials. In addition, the electrocatalytic performance of such hierarchical

copper-based nanostructures for oxygen evolution reaction also needs to be investigated. It is also unexplored that what influence of the pre-treatment by electrochemical methods on the hierarchical copper-based nanostructures will cause for their electrochemical performance for OER.

Last, copper-based nanomaterials have been widely applied in oxygen evolution reaction catalysis. In terms of copper oxides, the OER performance is not good enough ascribed to their poor conductivity. As a consequence, whether the combination of copper and copper oxide species as a complex is capable of improving the OER activity still needs to be studied. Meanwhile, how to develop the complex involving metallic copper and copper oxides with enhanced conductivity and high active surface area as highly efficient electrocatalysts for OER is also challenging. Another criterion for a successful OER catalyst is the long-term stability. As mentioned above, pure copper nanomaterials has a favorable OER activity but their stability in electrocatalysic conditions is undesirable due to the severe oxidation process on the copper surface. The fabrication of copper-based electrocatalysts with stable interface towards a long-term OER catalysis remains a huge project.

2.3 PhD in Context of Literature

In the thesis, the aforementioned questions about the electrochemical oxidation behaviors of copper nanomaterials with different structures have been studied. Based on the mechanism study above, the fabrication of copper-based nanostructure have been conducted for the electrocatalysis of oxygen evolution reaction. My contributions to the research are described as followed.

First, single crystalline copper nanowires have been electrochemically grown through anodic aluminum oxide (AAO) template. The environmental stability of the as-obtained CuNWs in both 40 % relative humidity (RH) atmosphere and 0.1 M NaOH aqueous solution have been subsequently studied. The growth rate of the oxide film on CuNWs in atmosperic environment has been estimated. In addition, the mechanism of the passive film

formation on CuNWs under electrochemical treatment in alkaline solution has also been revealed. The results of this study may be used for references in the protection and degradation-control for the practical CuNWs-based nanodevices and nanosystems.

Second, hierarchical copper nano-dendrites (CuNDs) are fabricated via electrodeposition method. The electrochemical behaviors of the as-obtained hierarchical CuNDs in 0.1 M NaOH aqueous solution are subsequently studied. Different from the homogeneous CuNWs, a non-equilibrium oxidation process has been found when subject to the cyclic voltammetry (CV) measurement. This study not only reveals the mechanism of the electrochemical oxidation behaviors of the CuNDs, but also provide more evidence for the fabrication or modification approaches on copper-based nanostructures using electrochemical methods.

Last, a strategy that transforming a metal organic frameworks (MOFs) thin layer into a nanostructured CuO/C hollow shell to coat on the 3D nano-dendritic Cu foams as an electrode was successfully developed. This electrode is claimed to provide an extraordinary electrocatalysis for oxygen evolution reaction (OER) with long-term durability in alkaline media. The results of this study may serve as a reference for the designing of novel class 3D metal/metal oxide hierarchical structures for gas-involved (i.e. O_2, H_2, CO_2 et al) electrocatalytic applications and beyond.

References

[1] Sakintuna, B.; Lamari-Darkrim, F.; Hirscher, M., *Int. J. Hydrogen Energy* **2007**, *32* (9), 1121-1140.

[2] Jain, P. K.; Huang, X.; El-Sayed, I. H.; El-Sayed, M. A., *Plasmonics* **2007**, *2* (3), 107-118.

[3] Gélin, P.; Primet, M., *Appl. Catal., B* **2002**, *39* (1), 1-37.

[4] Pradeep, T., *Thin Solid Films* **2009**, *517* (24), 6441-6478.

[5] Wang, B.; Xu, Y.; Yung, K.-L.; Chen, W.; Kang, C.-L., *J. Microelectromech. Syst.* **2013**, *22* (3), 519-526.

[6] Yu, W.; Porosoff, M. D.; Chen, J. G., *Chem. Rev.* **2012**, *112* (11), 5780-5817.

[7] Li, H.; Guo, C.-Y.; Xu, C.-L., *Biosens. Bioelectron.* **2015**, *63*, 339-346.

[8] Bing, Y.; Liu, H.; Zhang, L.; Ghosh, D.; Zhang, J., *Chem. Soc. Rev.* **2010**, *39* (6), 2184-2202.

[9] Hoene, A.; Prinz, C.; Walschus, U.; Lucke, S.; Patrzyk, M.; Wilhelm, L.; Neumann, H.-G.; Schlosser, M., *Biome. Mater.* **2013**, *8* (3), 035009.

[10] Rosei, F., *J. Phys.: Condens. Matter* **2004**, *16* (17), S1373.

[11] Rosei, F.; Rosei, R., *Surf. Sci.* **2002**, *500* (1), 395-413.

[12] Dreizin, E. L., *Prog. Energy Combust. Sci.* **2009**, *35* (2), 141-167.

[13] Wang, Q.; Lee, S.; Choi, H., *J. Phys. Chem. C* **2010**, *114* (5), 2027-2033.

[14] Perez-Alonso, F. J.; Elkjær, C. F.; Shim, S. S.; Abrams, B. L.; Stephens, I. E.; Chorkendorff, I., *J. Power Sources* **2011**, *196* (15), 6085-6091.

[15] Cherevko, S.; Kulyk, N.; Mayrhofer, K. J., *Nano Energy* **2016**, *29*, 275-298.

[16] Tang, L.; Han, B.; Persson, K.; Friesen, C.; He, T.; Sieradzki, K.; Ceder, G., *J. Am. Chem. Soc.* **2009**, *132* (2), 596-600.

[17] Tang, L.; Li, X.; Cammarata, R. C.; Friesen, C.; Sieradzki, K., *J. Am. Chem. Soc.* **2010**, *132* (33), 11722-11726.

[18] Jinnouchi, R.; Suzuki, K. K. T.; Morimoto, Y., *Catal. Today* **2016**, *262*, 100-109.

[19] Hack, D.; Dürr, A. B.; Deckers, K.; Chauhan, P.; Seling, N.; Rübenach, L.; Mertens, L.; Raabe, G.; Schoenebeck, F.; Enders, D., *Angew. Chem. Int. Ed.* **2016**, *55* (5), 1797-1800.

[20] Yang, P.; Peng, J.; Chu, Z.; Jiang, D.; Jin, W., *Biosens. Bioelectron.* **2017**, *92*, 709-717.

[21] dos Reis Benatto, G. A.; Roth, B.; Corazza, M.; Søndergaard, R. R.; Gevorgyan, S. A.; Jørgensen, M.; Krebs, F. C., *Nanoscale* **2016**, *8* (1), 318-326.

[22] Shen, W.; Zhang, X.; Huang, Q.; Xu, Q.; Song, W., *Nanoscale* **2014**, *6* (3), 1622-1628.

[23] Le Ouay, B.; Stellacci, F., *Nano Today* **2015**, *10* (3), 339-354.

[24] Ivanova, O. S.; Zamborini, F. P., *J. Am. Chem. Soc.* **2009**, *132* (1), 70-72.

[25] Liu, Y.; Lopes, P.; Cha, W.; Harder, R.; Maser, J.; Maxey, E.; Highland, M.; Markovic, N.; Hruszkewycz, S.; Stephenson, G., *Nano Lett.* **2017**, *17* (3), 1595-1601.

[26] Keast, V.; Myles, T.; Shahcheraghi, N.; Cortie, M., *J. Nanopart. Res.* **2016**, *18* (2), 45.

[27] Elechiguerra, J. L.; Larios-Lopez, L.; Liu, C.; Garcia-Gutierrez, D.; Camacho-Bragado, A.; Yacaman, M. J., *Chem. Mater.* **2005**, *17* (24), 6042-6052.

[28] Hedberg, Y. S.; Pradhan, S.; Cappellini, F.; Karlsson, M.-E.; Blomberg, E.; Karlsson, H.; Wallinder, I. O.; Hedberg, J. F., *Electrochim. Acta* **2016**, *212*, 360-371.

[29] Gromov, A. A.; Strokova, Y. I.; Teipel, U., *Chem. Eng. & Technol.* **2009**, *32* (7), 1049-1060.

[30] Lei, J.; Huang, H.; Dong, X.; Zhu, X.; Lu, B.; Lei, M., *J. Nanosci. Nanotechnol.* **2009**, *9* (12), 7503-7509.

[31] Hanrath, T.; Korgel, B. A., *J. Am. Chem. Soc.* **2004**, *126* (47), 15466-15472.

[32] Holmberg, V. C.; Korgel, B. A., *Chem. Mater.* **2010**, *22* (12), 3698-3703.

[33] Ji, Z.; Shen, X.; Zhu, G.; Zhou, H.; Yuan, A., *J. Mater. Chem.* **2012**, *22* (8), 3471-3477.

[34] Tasker, S. Z.; Standley, E. A.; Jamison, T. F., *Nature* **2014**, *509* (7500), 299.

[35] Lu, X.; Zhao, C., *Nat. commun.* **2015**, *6*, 6616.

[36] Singh, J.; Roychoudhury, A.; Srivastava, M.; Chaudhary, V.; Prasanna, R.; Lee, D. W.; Lee, S. H.; Malhotra, B., *J. Phys. Chem. C* **2013**, *117* (16), 8491-8502.

[37] Zhang, B.; Wu, J.; Li, X.; Liu, H.; Yadian, B.; Ramanujan, R.; Zhou, K.; Wu, R.; Hao, S.; Huang, Y., *J. Phys. Chem. C* **2014**, *118* (17), 9073-9077.

[38] Wang, Y.; Sun, H.; Duan, X.; Ang, H. M.; Tadé, M. O.; Wang, S., *Appl. Catal., B* **2015**, *172*, 73-81.

[39] Shu, H.-Y.; Chang, M.-C.; Chen, C.-C.; Chen, P.-E., *J. Hazard. Mater.* **2010**, *184* (1-3), 499-505.

[40] Tanboonchuy, V.; Grisdanurak, N.; Liao, C.-H., *J. Hazard. Mater.* **2012**, *205*, 40-46.

[41] Dror, I.; Jacov, O. M.; Cortis, A.; Berkowitz, B., *ACS Appl. Mater. & Interfaces* **2012**, *4* (7), 3416-3423.

[42] Sarathy, V.; Tratnyek, P. G.; Nurmi, J. T.; Baer, D. R.; Amonette, J. E.; Chun, C. L.; Penn, R. L.; Reardon, E. J., *J. Phys. Chem. C* **2008**, *112* (7), 2286-2293.

[43] Liu, A.; Liu, J.; Han, J.; Zhang, W.-x., *J. Hazard. Mater.* **2017**, *322*, 129-135.

[44] Im, H.-G.; Jung, S.-H.; Jin, J.; Lee, D.; Lee, J.; Lee, D.; Lee, J.-Y.; Kim, I.-D.; Bae, B.-S., *ACS nano* **2014**, *8* (10), 10973-10979.

[45] Zhai, H.; Wang, R.; Wang, W.; Wang, X.; Cheng, Y.; Shi, L.; Liu, Y.; Sun, J., *Nano Res.* **2015**, *8* (10), 3205-3215.

[46] Stortini, A.; Moretto, L.; Mardegan, A.; Ongaro, M.; Ugo, P., *Sens. Actuators, B* **2015**, *207*, 186-192.

[47] Han, D.; Li, X.; Zhao, X.; Feng, J.; Qian, Y., *J. Nanosci. Nanotechnol.* **2015**, *15* (9), 7177-7180.

[48] Jung, S. M.; Preston, D. J.; Jung, H. Y.; Deng, Z.; Wang, E. N.; Kong, J., *Adv. Mater.* **2016**, *28* (7), 1413-1419.

[49] Taylor, C. D.; Neurock, M.; Scully, J. R., *J. Electrochem. Soc.* **2008**, *155* (8), C407-C414.

[50] Xia, X.; Xie, C.; Cai, S.; Yang, Z.; Yang, X., *Corros. Sci.* **2006**, *48* (12), 3924-3932.

[51] Zaera, F., *Chem. Soc. Rev.* **2013**, *42* (7), 2746-2762.

[52] Huang, H.; Huang, W.; Xu, Y.; Ye, X.; Wu, M.; Shao, Q.; Ou, G.; Peng, Z.; Shi, J.; Chen, J., *Catal. Today* **2015**, *258*, 627-633.

[53] Ahmed, A.; Elvati, P.; Violi, A., *RSC Adv.* **2015**, *5* (44), 35033-35041.

[54] Mondal, J.; Biswas, A.; Chiba, S.; Zhao, Y., *Sci. Rep.* **2015**, *5*, 8294.

[55] Zhang, J.; Liu, J.; Peng, Q.; Wang, X.; Li, Y., *Chem. Mater.* **2006**, *18* (4), 867-871.

[56] Zhang, J.; Ma, J.; Zhang, S.; Wang, W.; Chen, Z., *Sens. Actuators, B* **2015**, *211*, 385-391.

[57] Niu, M.; Xu, W.; Zhu, S.; Liang, Y.; Cui, Z.; Yang, X.; Inoue, A., *J. Power Sources* **2017**, *362*, 10-19.

[58] Dubal, D. P.; Chodankar, N. R.; Gund, G. S.; Holze, R.; Lokhande, C. D.; Gomez-Romero, P., *Energy Technol.* **2015**, *3* (2), 168-176.

[59] Xia, L.-P.; Guo, P.; Wang, Y.; Ding, S.-Q.; He, J.-B., *J. Power Sources* 2014, *262*, 232-238.

[60] Xie, Y.; Huber, C. O., *Anal. Chem.* **1991**, *63* (17), 1714-1719.

[61] Burke, L.; Bruton, G.; Collins, J., *Electrochim. Acta* **1998**, *44* (8-9), 1467-1479.

[62] Burke, L. D.; Collins, J. A.; Murphy, M. A., *J. Solid State Electrochem.* **1999**, *4* (1), 34-41.

[63] Zhou, Y.; Neyerlin, K.; Olson, T. S.; Pylypenko, S.; Bult, J.; Dinh, H. N.; Gennett, T.; Shao, Z.; O'Hayre, R., *Energy Environ. Sci.* **2010**, *3* (10), 1437-1446.

[64] Carugno, S.; Chassaing, E.; Rosso, M.; González, G. A., *Mater. Chem. Phys.* **2014**, *143* (3), 1012-1017.

[65] Venkatasubramanian, R.; He, J.; Johnson, M. W.; Stern, I.; Kim, D. H.; Pesika, N. S., *Langmuir* **2013**, *29* (43), 13135-13139.

[66] Periasamy, A. P.; Liu, J.; Lin, H.-M.; Chang, H.-T., *J. Mater. Chem. A* **2013**, *1* (19), 5973-5981.

[67] Karim-Nezhad, G.; Dorraji, P. S., *Electrochim. Acta* **2010**, *55* (9), 3414-3420.

[68] Liu, X.; Sui, Y.; Yang, X.; Wei, Y.; Zou, B., *ACS Appl. Mater. Interfaces* **2016**, *8* (40), 26886-26894.

[69] Qiu, H.-J.; Shen, X.; Wang, J.; Hirata, A.; Fujita, T.; Wang, Y.; Chen, M., *ACS Catal.* **2015**, *5* (6), 3779-3785.

[70] Ren, Y.; Zhang, S.; Lin, R.; Wei, X., *Int. J. Hydrogen Energy* **2015**, *40* (6), 2621-2630.

[71] Sobczak, I.; Wolski, Ł., *Catal. Today* **2015**, *254*, 72-82.

[72] Mintsouli, I.; Georgieva, J.; Armyanov, S.; Valova, E.; Avdeev, G.; Hubin, A.; Steenhaut, O.; Dille, J.; Tsiplakides, D.; Balomenou, S., *Appl. Catal. B* **2013**, *136*, 160-167.

[73] Zhang, N.; Bu, L.; Guo, S.; Guo, J.; Huang, X., *Nano Lett.* **2016**, *16* (8), 5037-5043.

[74] Zhao, X.; Dai, L.; Qin, Q.; Pei, F.; Hu, C.; Zheng, N., *Small* **2017**, *13* (12).

[75] Coleman, E. J., *J. Catal.* **2014**, *316*, 191-200.

[76] Jin, Y.; Chen, F., *Electrochim. Acta* **2015**, *158*, 437-445.

[77] Awad, M. I.; Ohsaka, T., *J. Power Sources* **2013**, *226*, 306-312.

[78] Jin, Y.; Chen, F.; Lei, Y.; Wu, X., *ChemCatChem* **2015**, *7* (15), 2377-2383.

[79] Ma, W.; Chen, F.; Zhang, N.; Wu, X., *J. Mol. Model.* **2014**, *20* (10), 2454.

[80] Wu, X.; Chen, F.; Jin, Y.; Zhang, N.; Johnston, R. L., *ACS appl. Mater.Interfaces* **2015**, *7* (32), 17782-17791.

[81] Wu, Z.-S.; Yang, S.; Sun, Y.; Parvez, K.; Feng, X.; Müllen, K., *J. Am. Chem. Soc.* **2012**, *134* (22), 9082-9085.

[82] Fu, G.; Cui, Z.; Chen, Y.; Li, Y.; Tang, Y.; Goodenough, J. B., *Adv. Energy Mater.* **2017**, *7* (1).

[83] Ania, C. O.; Seredych, M.; Rodriguez-Castellon, E.; Bandosz, T. J., *Appl. Catal. B* **2015**, *163*, 424-435.

[84] Shao, H.; Zhang, X.; Huang, H.; Zhang, K.; Wang, M.; Zhang, C.; Yang, Y.; Wen, M.; Zheng, W., *ACS Appl Mater. Interfaces* **2017**, *9* (48), 41945-41954.

[85] Goenaga, G. A.; Foister, S.; Belapure, A.; Byrne, K.; Hawks, S.; Papandrew, A. B.; Zawodzinski, T., *ECS Electrochem. Lett.* **2014**, *3* (11), F68-F71.

[86] Wu, Z.; Li, Y.; Liu, J.; Lu, Z.; Zhang, H.; Yang, B., *Angew. Chem. Int. Ed.* **2014**, *53* (45), 12196-12200.

[87] López, N.; Aguila, G.; Araya, P.; Guerrero, S., *Catal. Commun.* **2018**, *104*, 17-21.

[88] Davis, D. J.; Lambert, T. N.; Vigil, J. A.; Rodriguez, M. A.; Brumbach, M. T.; Coker, E. N.; Limmer, S. J., *J. Phys. Chem. C* **2014**, *118* (31), 17342-17350.

[89] Windle, C. D.; Perutz, R. N., *Coord. Chem. Rev.* **2012**, *256* (21-22), 2562-2570.

[90] Gattrell, M.; Gupta, N., *J. Electroanal. Chem.* **2006**, *594* (1), 1-19.

[91] Nakata, K.; Ozaki, T.; Terashima, C.; Fujishima, A.; Einaga, Y., *Angew. Chem. Int. Ed.* **2014**, *53* (3), 871-874.

[92] Li, C. W.; Ciston, J.; Kanan, M. W., *Nature* **2014**, *508* (7497), 504.

[93] Appel, A. M., *Nature* **2014**, *508* (7497), 460.

[94] Li, C. W.; Kanan, M. W., *J. Am. Chem. Soc.* **2012**, *134* (17), 7231-7234.

[95] Montoya, J. H.; Peterson, A. A.; Nørskov, J. K., *ChemCatChem* **2013**, *5* (3), 737-742.

[96] Calle-Vallejo, F.; Koper, M., *Angew. Chem.* **2013**, *125* (28), 7423-7426.

[97] Ren, D.; Deng, Y.; Handoko, A. D.; Chen, C. S.; Malkhandi, S.; Yeo, B. S., *ACS Catal.* **2015**, *5* (5), 2814-2821.

[98] Roberts, F. S.; Kuhl, K. P.; Nilsson, A., *Angew. Chem.* **2015**, *127* (17), 5268-5271.

[99] Tang, Q.; Lee, Y.; Li, D.-Y.; Choi, W.; Liu, C.; Lee, D.; Jiang, D.-e., *J. Am. Chem. Soc.* **2017**, *139* (28), 9728-9736.

[100] Zhao, J.; Tran, P. D.; Chen, Y.; Loo, J. S.; Barber, J.; Xu, Z. J., *ACS Catal.* **2015**, *5* (7), 4115-4120.

[101] Morales-Guio, C. G.; Liardet, L.; Mayer, M. T.; Tilley, S. D.; Grätzel, M.; Hu, X., *Angew. Chem. Int. Ed.* **2015**, *54* (2), 664-667.

[102] Luo, J.; Steier, L.; Son, M.-K.; Schreier, M.; Mayer, M. T.; Grätzel, M., *Nano Lett.* **2016**, *16* (3), 1848-1857.

[103] Dubale, A. A.; Tamirat, A. G.; Chen, H.-M.; Berhe, T. A.; Pan, C.-J.; Su, W.-N.; Hwang, B.-J., *J. Mater. Chem. A* **2016**, *4* (6), 2205-2216.

[104] Qi, H.; Wolfe, J.; Fichou, D.; Chen, Z., *Sci. Rep.* **2016**, *6*, 30882.

[105] Liu, X.; Zheng, H.; Sun, Z.; Han, A.; Du, P., *ACS Catal.* **2015**, *5* (3), 1530-1538.

[106] Lu, Q.; Hutchings, G. S.; Yu, W.; Zhou, Y.; Forest, R. V.; Tao, R.; Rosen, J.; Yonemoto, B. T.; Cao, Z.; Zheng, H., *Nat. commun.* **2015**, *6*, 6567.

[107] Wu, J.; Li, X.; Yadian, B.; Liu, H.; Chun, S.; Zhang, B.; Zhou, K.; Gan, C. L.; Huang, Y., *Electrochem. Commun.* **2013**, *26*, 21-24.

[108] Du, J.; Chen, Z.; Ye, S.; Wiley, B. J.; Meyer, T. J., *Angew. Chem. Int. Ed.* **2015**, *54* (7), 2073-2078.

[109] Toparli, C.; Sarfraz, A.; Wieck, A. D.; Rohwerder, M.; Erbe, A., *Electrochim. Acta* **2017**, *236*, 104-115.

[110] Yu, F.; Li, F.; Zhang, B.; Li, H.; Sun, L., *ACS Catal.* **2014**, *5* (2), 627-630.

[111] Liu, X.; Cui, S.; Qian, M.; Sun, Z.; Du, P., *Chem. Commun.* **2016**, *52* (32), 5546-5549.

[112] Cui, S.; Liu, X.; Sun, Z.; Du, P., *J. Phys. Chem. C*, **2016**, 120(2): 831-840

[113] Cheng, N.; Xue, Y.; Liu, Q.; Tian, J.; Zhang, L.; Asiri, A. M.; Sun, X., *Electrochim. Acta* **2015**, *163*, 102-106.

[114] Andersen, N. I.; Serov, A.; Atanassov, P., *Appl. Catal. B* **2015**, *163*, 623-627.

Chapter 3

Experimental Methodology

In this chapter, the rationale for the selection of the synthetic methods of multiple Cu-based nanostructured, the techniques used for the characterization and measurements are summarized. First, the principle for the preparation of anodic aluminum oxide (AAO) template is elaborated, followed by the electrochemical deposition of nanowires into AAO template. Subsequently, the principle of electrodeposition of metal foams by bubble dynamic template method as well as the rationale for the growth of MOFs layer on the metal oxide surface are stated. Finally, the principles of the characterization and measurement techniques in the thesis are illustrated.

3.1 Rationale for selection of Methods

Cu nanomaterials have been selected as the objectives to study their electrochemical oxidation behaviors since copper is a typical transition metal with abroad applications. Furthermore, the Cu possesses a wide range of oxidation states, including Cu^0, Cu^I, Cu^{II} and Cu^{III}, which provides the possibility of one- and/ or two-electron pathways in electrochemical oxidation reactions.

In the first part, anodic aluminum oxide (AAO) template strategy was selected to synthesize single-crystalline CuNWs as the target materials. The single-crystalline CuNWs prepared by wet-chemistry synthetic methods are usually covered with organic compounds on the surface, which is quite different to be removed, resulting in more challenges in the following electrochemical tests.[1] AAO temple method can produce a large amount of nanowires with controlled diameter and length, homogeneous morphology and absolute clean surface without too many defects.[2] Therefore, the CuNWs prepared by the approach are suitable to be used for the investigation on the natural electrochemical oxidation behaviors. In order to study the electrochemical oxidation process on as-fabricated CuNWs in atmospheric air, the exposure to the air with a constant temperature and relative humidity were conducted. For the case in aqueous solution, electrochemical measurements were carried out using CuNWs as the working electrode. The oxidized CuNWs under different conditions above would be characterized by TEM observation. Since TEM has the powerful capacity to direct observe the microstructure details of materials with high resolution. Therefore, it can be conveniently used to study the formation mechanism of oxide films on CuNWs.

In the second part, hydrogen-bubbles assist method was employed to electrochemically deposit copper foams composed of copper nanodendrites. The general porous structure and large surface area of the CuNDs make them promising candidate for the substrate for gas-evolving electrocatalysis.[3] Therefore, electrochemical measurements were carried out to investigate the oxidation process on CuNDs. Unlike the CuNWs with homogeneous nano size, the as-prepared CuNDs are stacked to form a 3D structure, which is beyond the

characterizing ability individually based on TEM. The combination of SEM and XRD with TEM were adopted to study the morphology and phase evolution of CuNDs during the electrochemical treatment, which is able to provide a comprehensive understanding of the oxidation mechanism on CuNDs in aqueous solution.

In the last part, CuNDs foam was first electrodeposited as the template for the further modification of catalyst electrode for oxygen evolution reaction due to its merits that have been mentioned above. However, the results above indicates that the bare CuNDs electrode is unstable as thus not appropriate for the electrocatalysis of OER under high overpotential in aqueous solution. Therefore, the surface modification by forming a passive layer on top of the CuNDs were conducted to improve their stability of CuNDs. On the other hand, the high efficiency of catalysis requires a large amount of active site to drive the occurrence of oxygen evolution reaction. The fabrication of a nanostructured CuO/C hollow shell can not only meet the requirement for the abundant active sites, but also increase their conductivity and mechanism stability. Furthermore, the inner void under the hollow shell is able to buffer the stress caused by the fierce reaction and bubble transportation.

3.2 Synthesis

3.2.1 Preparation of anodic aluminum oxide (AAO) template

Anodic aluminum oxide (AAO) template is one type of porous nanomaterial. Anodic aluminum could be easily obtained by putting aluminum into acid solution for anodic oxidation. Through the modulation of the anodic reaction conditions, two kinds of aluminum oxide could be fabricated: compact type and porous type, which is highly dependent to the chemical properties of the electrolyte for the fabrication of the anodic aluminum. Neutral electrolytes (pH 5-7) tend to produce the highly compact anodic aluminum oxide layer, such as borate, oxalate, citrate, phosphate, tungstate solutions et al. This is because the anodic aluminum oxide layer cannot be dissolved in such electrolytes. In contrast, acidic electrolytes are able to produce porous anodic aluminum oxide layer,

such as selenic acid, sulfuric acid, oxalic acid, phosphoric acid, citric acid et al. since the AAO layer can be slightly dissolved into the electrolytes above.

The fabrication of the AAO template is accompanied with the formation of anodic electrolysis and its dissolution into the electrolyte. The electrode reactions are as followed:

Anode: $2Al + 6OH^- \rightarrow Al_2O_3 + 3H_2O + 6e^-$ (1)

Cathode: $6H^+ + 6e^- \rightarrow H_2 \uparrow$ (2)

The self-construct AAO template with periodic hexagonal arrangement is one typical structure (Figure 3.1), whose formation can be explained using different theoretical models. Including electric field assist dissolution model, critical current density effect model and stress effect model et al.[4]

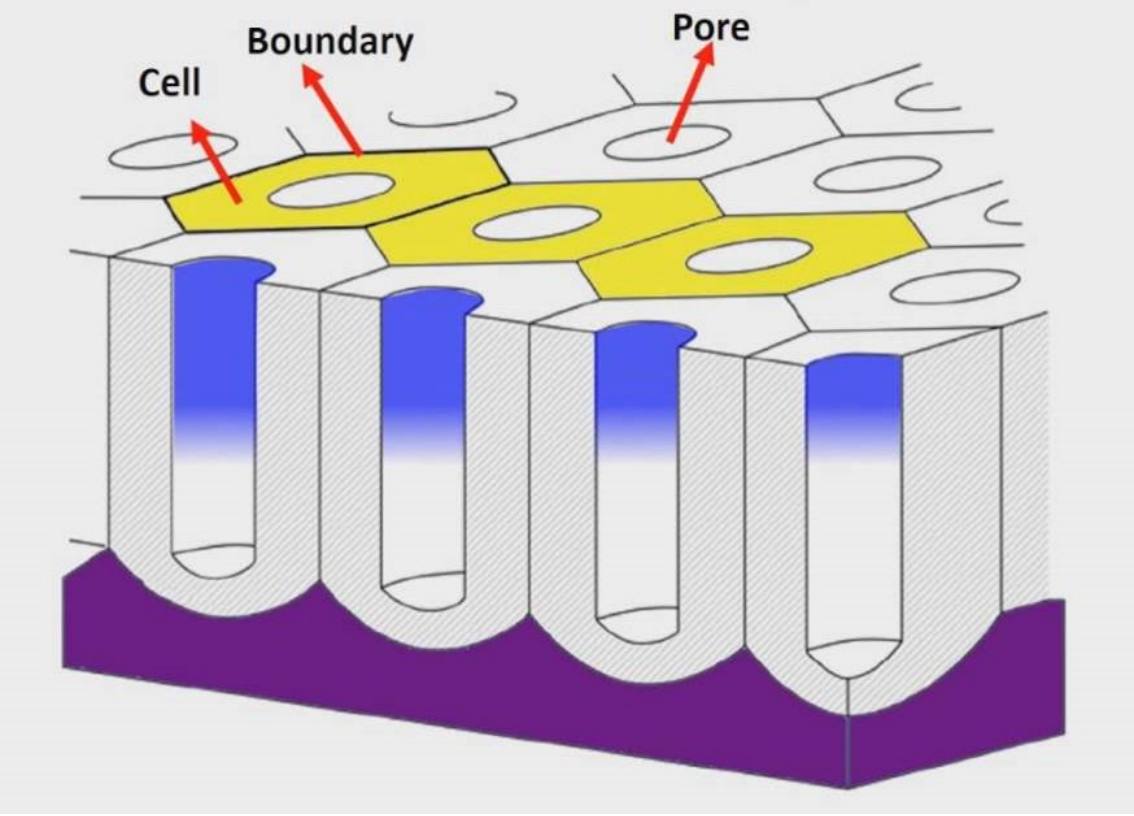

Figure 3.1 Self-construct AAO template with periodic hexagonal arrangement.[4]

In the electric field assist dissolution model, the formation of porous AAO template consists of three steps: the formation of the barrier layer, partial dissolution of the barrier layer and the growth of porous layer. In the first step, the reaction between aluminum and the electrolyte leads to the formation of the barrier layer. In the second step, the as-formed AAO layer will continue react with the electrolyte so that part of the layer is dissolved. In the last step, plentiful etched spots with regular arrangement are generated on the surface of aluminum as the pore nucleuses, which is the base of the growth of the pore channels. In the pore channels, the previous homogeneously distributed electric field becomes concentrated, resulting in the increase of dissolution rate of the pore nucleuses. At the same time, the electric field in the pore channels is much stronger than that at other locations. The located high temperature ascribed to the higher current density in the pore channels will accelerate the reaction rate at the bottom of the pores. Due to the much higher dissolution rate of the pore nucleuses than that of the pore walls, the pore nucleuses could undergoing continuous growth until the formation of the pore channels. When the growth rate of the barrier layer is equal to its dissolution rate, the growth of pore channels reach a stable step.

In the critical current density model, the researchers believe that there is always a limit critical current density in a particular anodic oxidation system. When the current density is beyond this critical value, the 100 % current efficiency in such oxidation process is capable of leading to the formation of a compact aluminum oxide layer on the aluminum surface. On the contrary, a porous AAO layer can be produced when the current efficiency is below 60 %.

In the stress model, a swelling stress occurs on the surface of the aluminum during the oxidation process since the as-generated aluminum oxide has a larger volume than its aluminum precursor. As a consequence, the effect of the stress brings about the formation of hexagonal pores with periodical arrangement according to the principle of minimum energy.

3.2.2 Electrodeposition of nanowires into AAO template

The latter one is regarded to possess a promising material in various applications due to its merits including homogeneous distribution of pores, identical size of the pore diameter, the precise control of the pore shape and the large surface area et al. Among the multiple applications of AAO template, the growth of one dimensional nanomaterials such as metals, metal oxides, alloys and semiconductors have been successfully conducted. One big advantage of this method is that the length of the nanowires can be easily controlled by the modulation of the experimental conditions. For example, metallic nanowires arrays with different length-diameter ratios can be realized through the control of the amount of the metal ions in the electrolyte.

As shown in Figure 3.1, a non-conductive aluminum oxide layer presents between the pore channels and the Al substrate, which makes it impossible to conduct electrodeposition directly using the bare AAO template. Therefore, a modified surface film with high conductivity (Au, Pt et al.) is necessarily deposited on the one end of the pore channels as a conductive substrate. As to the other end, the aluminum oxide barrier layer should be removed prior to the electrodeposition, which is initiated from the other side, as shown in Figure 3.2.

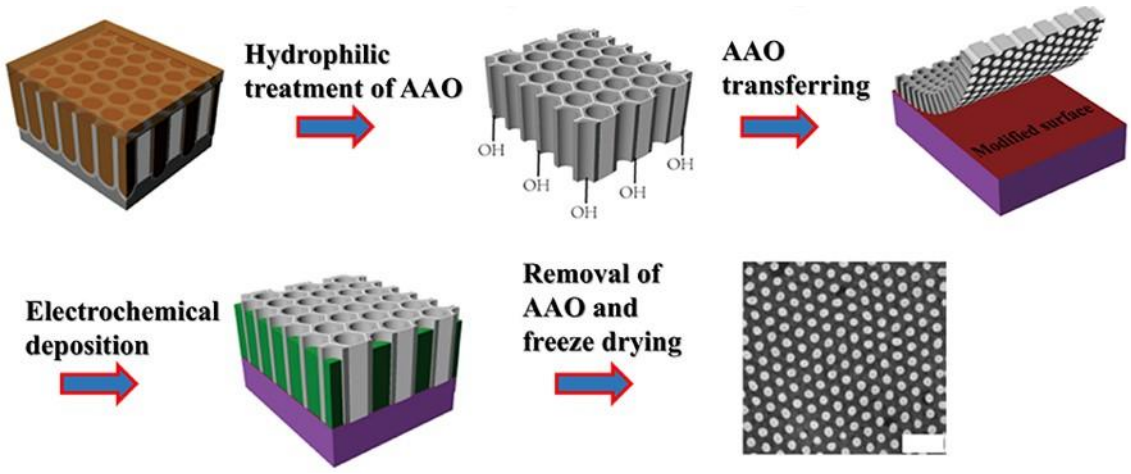

Figure 3.2 Electrodeposition of metallic nanowires into AAO template.[3]

Take metal nanowires as an example, they are able to be fabricated via various electrochemical methods, such as constant current density electrodeposition, constant potential deposition, pulsed deposition and cyclic voltammetry deposition et al. The methods to fabricate single-crystalline nanowires are usually constant current density or potential methods. Through modulating the value of current density (potential), the control of the growth rate and orientation of the nanowire may be achieved. Under low current density, the growth rate of the nanowire is relatively low and the metal nanowire tend to be stacked along the lattice plane with low surface energy, such as (1 1 1) for body centered cubic crystals, Au, Cu et al. When the current density or potential is higher enough, the growth rate of the nanowires is necessarily higher and their growth orientation may alter since the nanowire could be stacked among other lattice planes with higher surface energy, which is beneficial from the high energy supply provided by the higher current density from the power station.

3.2.3 Electrodeposition of metal foams by bubble dynamic template method

As we know, hydrogen evolution reaction (HER) is almost inevitable in the electrodeposition of metal/alloy structure from the aqueous solutions. Usually, we take the HER as a threat for the electroplating and electrometallurgy since the existence of the hydrogen will bring some defects or dangers to the target metallic materials. However, it can also be used as a powerful method to fabricate various porous structures if the HER process is well coordinated with the electrodeposition process.

As shown in the AAO template case, the formation a compact aluminum oxide layer requires a nearly 100 % efficiency of the current. Similarly, the ideal electrodeposition of metal is also expect a 100 % current efficiency at the liquid-solid interface. Nevertheless, if the electrodeposition is conducted under a high current density, there will be a concentration gradient of the target metal ions around the cathode. As a result, the electrodeposition of the metals is highly dependent on the rate of ion diffusion and hydrogen evolution reaction that happens on the surface of the cathode. Upon the absorption of the hydrogen bubbles on the cathode surface, they will act as an insulator

between the electrolyte and the cathode. And this will lead to the formation a gas-liquid-solid interface consisting of three phases. Thus, the electrodeposition of the metals can only occur between the bubbles so that a porous structure is formed (Figure 3.3).[5]

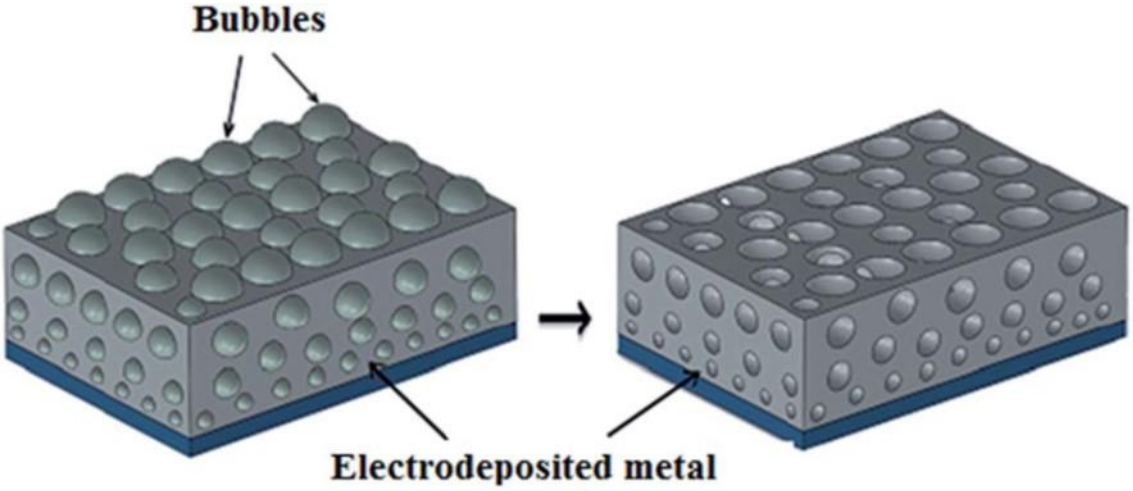

Figure 3.3 The schematic diagram for the electrodeposition of porous films on a gas–liquid–solid three-phase interface.[5]

The building of such porous structure is mainly associated with the kinetics of bubble generation and the behaviors of the crystallization during the fast electrodeposition process. Different from traditional electrodeposition, bubbles assist method proceeds at a high overpotential or current density since numerous bubbles are required to be generated in order to create the typical gas-liquid-solid interface near the cathode surface in the electrolyte. As a consequence, the kinetics of the bubbles generate including the nucleation, growth and diffusion of the bubbles will determine the density and pore size of the porous structure. With the proceeding of the electrodeposition, a 3D porous structure will construct with the increase of the deposition time.

In addition, the kinetics of the bubbles generation is dependent on the wettability of the cathode surface. To be more specific, the bubbles that are generated on a surperhydrophilic surface tend to separate rapidly and break off easily so that they can hardly residue on the cathode surface as the template for electrodeposition, which leads to the formation of a smooth and compact layer on the cathode (Figure 3.4a). In contrast, the bubbles that formed on a superhydrophobic surface can be absorbed on the rough surface and achieve a large

break-off diameters so that the electrodeposition can be proceeded via the bubbles template on the cathode surface (Figure 3.4b).

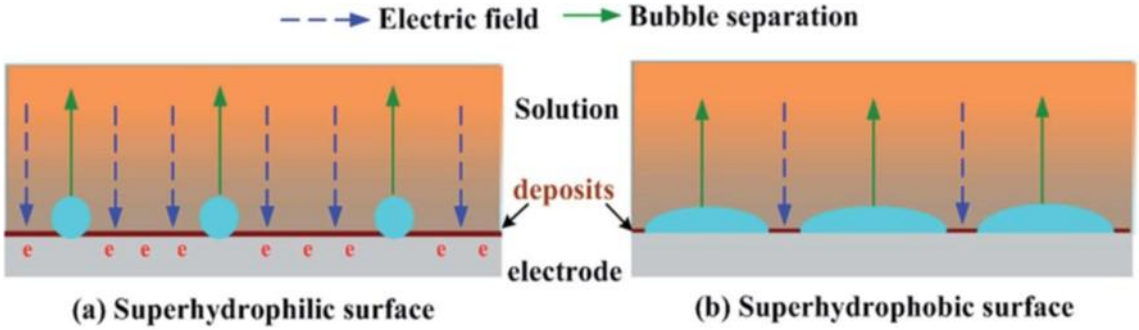

Figure 3.4 The bubble adsorption and current distribution on the electrode surface.[6]

The wettability is determined by the surface conditions of the cathode and the composition of the electrolyte. The wettability is able to be adjusted by the addition of surfactants into the electrolyte, where a decreased surface tension is achieved. Therefore, the incorporation of the surfactants with the electrolyte is necessary to realize the porous metallic structure with homogenous pores. According to the previous study, an increase concentration of the surfactants will lead to the decrease of the bubble sizes.[6]

In addition to the kinetics of the bubble generation, the crystallization behaviors of the metals also plays an important role in determining the chemical composition and morphology of the as-electrodeposited structure. The construction of such 3D porous structure is mainly controlled by the diffusion process of the metal ions. The deposition tend to occur at the active sites without hydrogen bubbles so that the protrusions are formed. Then the protrusions will continue to grow to build a porous structure. A high growth rate of the protrusions can be achieved by increasing the concentration of the metal ions, the degree of the concentration polarization. Besides, the exchange current density of the metals, which is the intrinsic property of the metals, also influences the electrodeposition behaviors. The construction of the metals with high exchange current density (Au, Ag Cu et al) is much easier than those with low values (Fe, Co and Ni). What's more, the pH value of the electrolytes will also affect the electrodeposition process since the pH value is associated with the hydrolysis of the metal ions. For example, the pure $NiCl_2$ can hardly be used as the electrolyte due to the strong hydrolysis effect.

3.2.4 In situ transformation of Cu_2O into HKUST-1

Metal organic frameworks (MOFs) are constructed with periodical subclass of coordination polymers that are composed of metal ion and organic ligands.[7] For example, Cu-based MOFs HKUST-1 is composed of copper ions and 1, 3, 5-benzenetricarboxylic acid (Figure 3.5). They have been widely used as ideal precursors to fabricate various nanomaterials including metal oxides, metal sulfides, metal phosphides and their composites et al with high specific surface area and multiple functions.

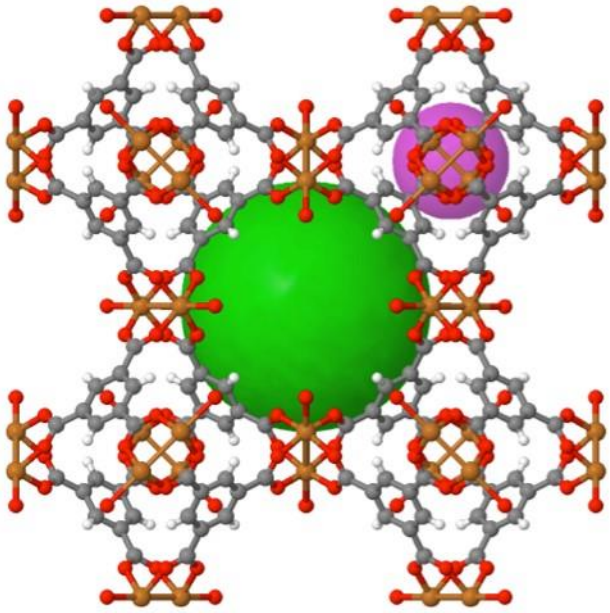

Figure 3.5 The subclass of coordination polymer of HKUST-1.[7]

Normally, the synthesis of MOFs are conducted via hydrothermal or solvothermal methods, where the metal ions and the organic ligands directly coordinate with each other to form a one dimensional, two dimensional or three dimensional MOFs particles. For the current project, the target is to grow MOFs layer on top of CuNDs with a native Cu_2O thin film. Therefore, the native Cu_2O layer is used as the source of copper ion and coordinate with the ligand in order to form a HKUST-1 thin film at the outmost position of the CuNDs.

Since the chemical activity of Cu_2O is relatively high compared to CuO, the key to accomplish the in situ fabrication of HKUST-1 thin film is the control of its growth rate during the transformation process. As we know, the transformation rate of Cu_2O into

HKUST-1 is associated with the dissolution rate of the Cu_2O film and the diffusion rate of the dissolved copper ion and the ligands in the solvents. Thus, the reaction temperature and the concentration of the ligands are important factors in the transformation process. In addition, another key factor that can determine the diffusion rate of the ions is the viscosity of the solvent.

Table 3.1 Physical properties of common solvents.

Name	Molecular formula	Specific Density	Surface Tension	Viscosity
Formamide	CH_3NO	1.129	57.0	3.34
Nitromethane	CH_3NO_2	1.129	36.3	0.63
Methanol	CH_4O	0.787	22.1	0.54
Ethanol	C_2H_6O	0.787	22.0	1.07
Acetone	C_3H_6O	0.786	23.0	0.31
Methyl acetate	C_3H_6O2	0.927	24.5	0.36
N,N-Dimethylformamide	C_3H_7NO	0.945	34.4	0.79
Glycerol	$C_3H_8O_3$	1.257	76.2	934
1-Butanol	$C_4H_{10}O$	0.806	25.0	2.54
Pyridine	C_5H_5N	0.979	36.7	0.88
Benzene	C_6H_6	0.873	28.2	0.60
Aniline	C_6H_7N	1.018	42.4	3.85
Cyclohexanone	$C_6H_{10}O$	0.942	34.4	2.02
Cyclohexane	C_6H_{12}	0.773	24.7	0.89
Benzonitrile	C_7H_5N	1.001	38.8	1.27
Benzaldehyde	C_7H_6O	1.040	38.3	1.4
Toluene	C_7H_8	0.865	27.9	0.56
Benzyl alcohol	C_7H_80	1.041	36.8	5.47
3-Methylphenol	C_7H_8O	1.030	35.8	12.9
2-Heptanone	$C_7H_{14}O$	0.811	26.1	0.71
n-Heptane	C_7H_{16}	0.682	19.8	0.39
Styrene	C_8H_8	0.900	32.0	0.70
Acetophenone	C_8H_8O	1.024	39.0	1.68
Ethylbenzene	C_8H_{10}	0.865	28.6	0.63
Water	H_2O	0.999	72.7	0.89
Hydrogen peroxide	H_2O_2	1.449	74.0	1.25
Hydrazine	H_4N_2	0.950	66.9	0.88

As shown in Table 3.1, the commonly used solvents such as acetone, methanol, ethanol and DMF et al. all have a viscosity around or less than 1, which means the ion diffusion is relatively easy in these solvents. As a result for the current case, the in situ HUKST-1 growth from Cu_2O will undergo at a high rate, leading to the inhomogeneous growth of HUKST-1. The MOFs can be formed not only on the surface of the Cu_2O film, but also in the solvent due to the fast diffusion rate of the dissolve copper ion and coordinate with the organic ligands in the solvent. Thus, it is necessary to employ a solvent with high viscosity, such as benzyl alcohol with a viscosity of 5.47. In such a high-viscosity solvent, the diffusion rate of the copper ions from the dissolution of Cu_2O will be much slower than that in the solvents like methanol so that the growth rate of the HKUST-1 is controllable on the surface of Cu_2O film to form a homogeneous coating.

3.3 Characterization

3.3.1 Transmission electron microscopy (TEM)

Transmission electron microscopy (TEM) is a microscopic technology where an electron beam with high energy is emitted, accelerated within the vacuum chamber then transmitted through an ultrathin specimen. The primary image is formed by the focus of the scattered radiation of the specimen by the objective lens. And then the primary image is further magnified by the intermediate lens and projection lens to produce the final image (Figure 3.6). At high resolution, the primary image is, in effect, the fourier transform of the diffraction pattern, which is produced at the back focal plane of the objective lens. Therefore, the high resolution transmission electron microscopy image is actually the interference pattern of the incident beam and the diffractive beam at the back focal plane of the objective lens. The pattern will be detected and magnified on a screen or charge-coupled device (CCD) camera after their interaction with the specimen.

At low magnifications, the contrast in TEM images is on account of the different electrons scattering or absorption of the materials with different composition or thickness. The contrast of the image can be enhanced by inserting the objective aperture to block the

scattered electrons. In comparison, the image contrast at high magnifications are much more complicated, where diffraction contrast, phase contrast and mass-thickness contrast may all be taken into account. The contrast of a HRTEM image is formed due to the interference of the electron waves in the image plane.

High-resolution transmission electron microscopy (HR-TEM) is usually used to observe and take image of the structure of the sample at atomic scale, where individual atoms of a crystal can be observed clearly.[8] Based on the atom arrangement of the specimen, crystalline information can be obtained and characterized at atomic scale. On the basis of Fast Fourier Transform algorithm[9] of each ingredients with different crystalline structures, identical crystalline structure but differing cell parameters can be distinguished within a tiny area, such as the oxide films in the present project.

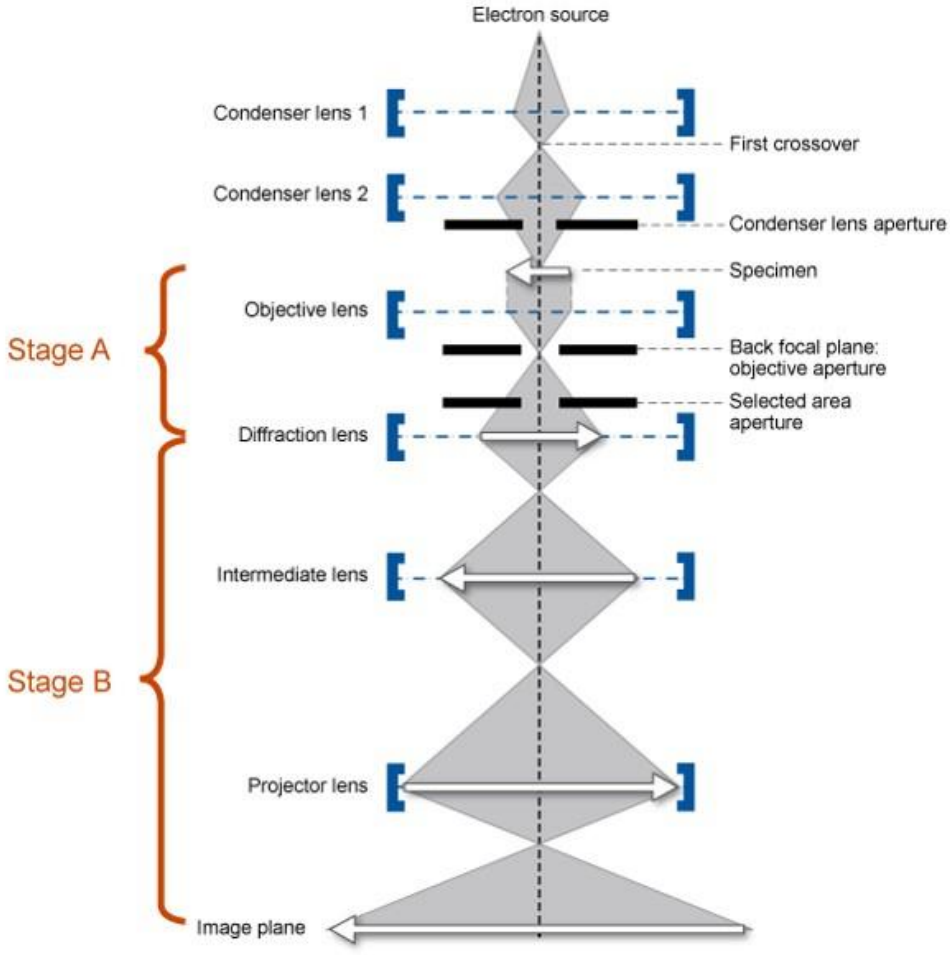

Figure 3.6 Image formation process in TEM.[10]

Another important application of TEM is to investigate the crystalline information of the sample using select area electron diffraction (SAED). As shown in Figure 3.7, diffracted beam is produced by the interaction of the electron beam and the crystalline thin specimen when the Bragg's Law is satisfied. The waves from different directions will interact with each other and be focused at the back focal plane of the objective lens as the diffraction pattern or rings, where the incident beam with diffraction will penetrate the objective lens and produce a bright spot in the center of the pattern or rings (Figure 3.7). Through the index of the obtained SAED pattern, the crystalline information of the sample could be analyzed, including the space group, crystal parameters et al.

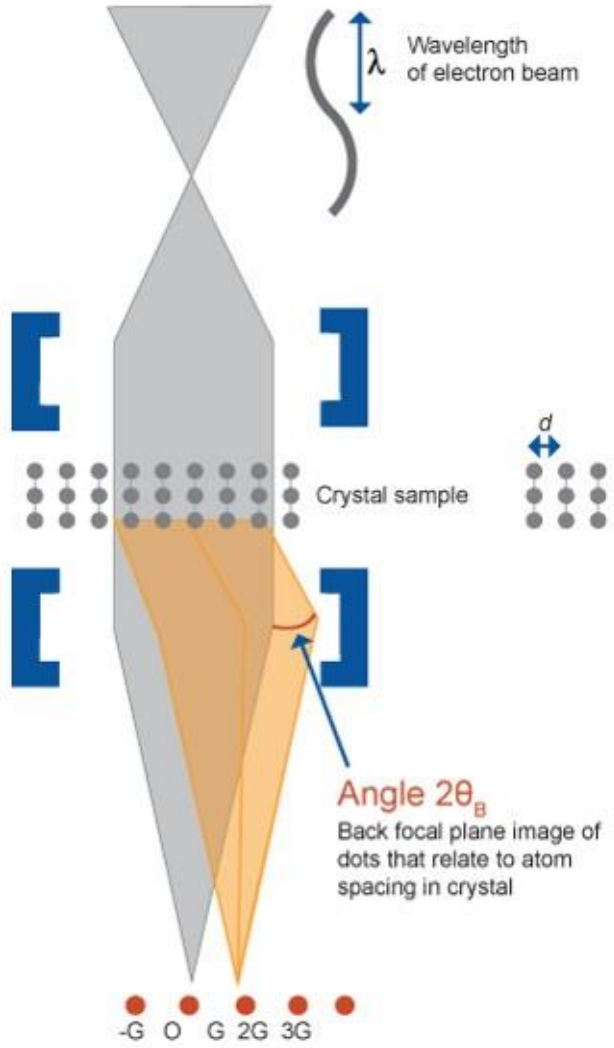

Figure 3.7 The working principle of diffraction in TEM.[10]

3.3.2 Scanning transmission electron microscopy (STEM)

A scanning transmission electron microscopy (STEM) is one type of TEM, where the electron beam is focused to a spot with a typical size between 0.05 nm and 1 nm and scan over the sample, which is similar to SEM. Different from TEM, the beam illuminated at each point of sample is parallel to the optical axis in STEM, as shown in Figure 3.8. Beneficial from the rastering of the beam across the sample, some analytical techniques can be performed in STEM , such as dark-field imaging based on Z-contrast, spectroscopic mapping by electron energy loss spectroscopy (EELS) and energy dispersive X-ray (EDX) spectroscopy.

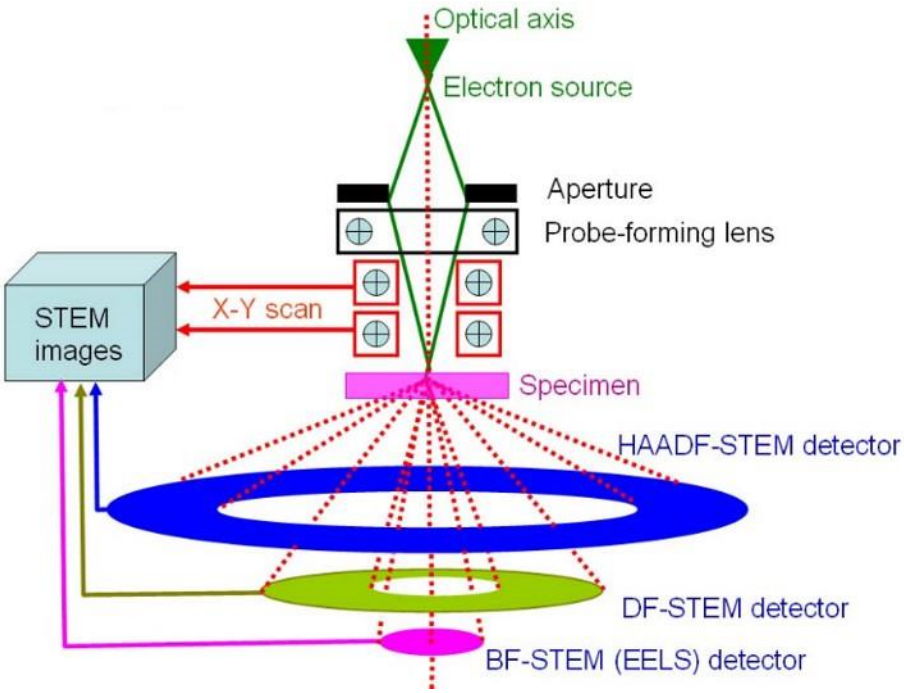

Figure 3.8 Schematic of scanning transmission electron microscopy.[10]

3.3.3 Scanning electron microscopy (SEM)

Scanning electron microscopy (SEM) is widely used to characterize the surface information of the samples by means of the scanning of a focused electrons beam. As we know, the interaction between the electrons and the atoms in the samples can produces varieties of signals (secondary electrons and backscattered electrons et al) that can be used

to interpret the information of the samples' morphology and composition et al. As shown in Figure 3.9, two detectors are located on top of the sample to collect the secondary electrons and backscattered electrons signals.

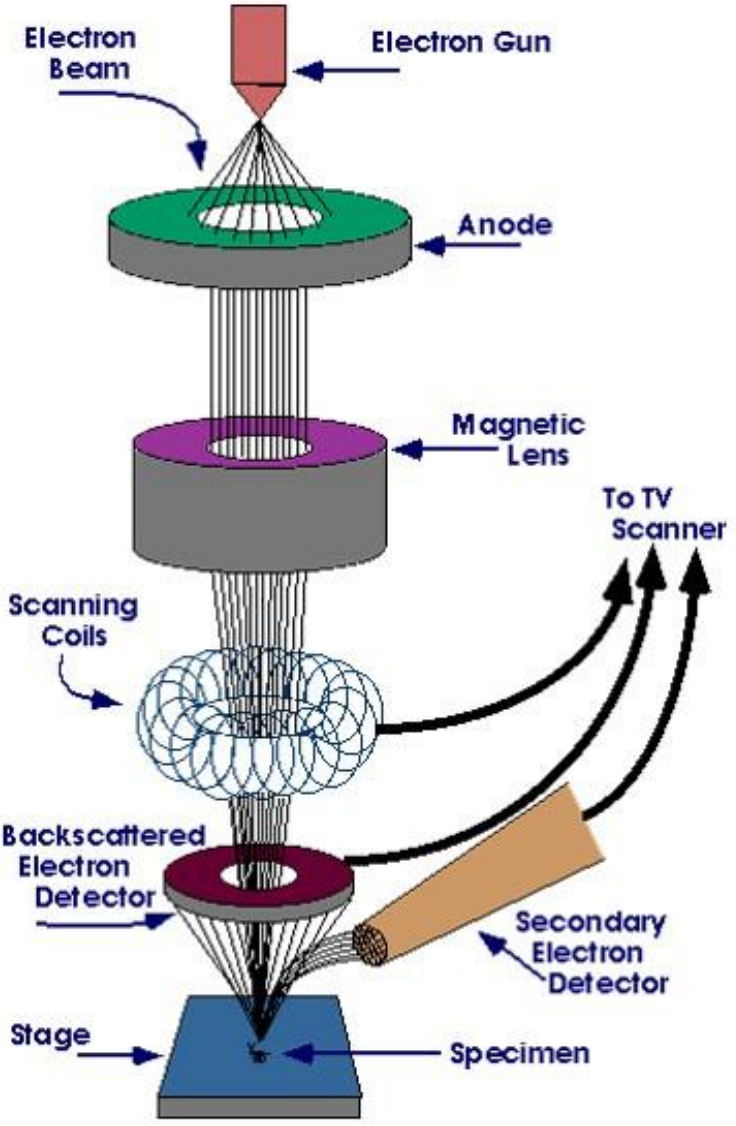

Figure 3.9 Schematic of scanning electron microscopy.[11]

Among the signals, secondary electrons that are emitted from the atoms by inelastic scattering excitation is the most common source to be used to analyze the sample. In the secondary electron imaging (SEI) mode, the topological image of the sample can be produced ascribed to the difference of the detected number of secondary electrons on the sample surface. Owing to the fine size of the electron beam, SEM images can present a 3D

appearance with a large depth of the sample surface, which can facilitates the understanding of the structure of the specimen. Different from SEI mode, backscattered electrons that are directly reflected from the specimen surface by elastic scattering can also be used to produce image. However, the resolution of the image taken in backscattered electron imaging (BEI) mode is usually less than that in the SEI mode since the backscattered electrons emerge from the deeper positions of the samples. What's more, the BEI mode is commonly applied to characterize the samples with different elements because the BE signal is highly dependent to the atomic number of the elements. Based on this feature, the BEI mode can be used to investigate the elemental distribution on the sample surface.

3.3.4 Powder X-ray diffraction (XRD)

X-ray powder diffraction (XRD) is a technique to characterize the phase information of a crystalline material by revealing the unit cell information. Beneficial from the discovery that crystalline substances could be used as 3D diffraction grids for the X-ray wavelengths that are close to the spacings in the crystal lattices, XRD has long been applied as a common technology in revealing the crystal structures of materials. In the typical measurement process, X-rays sources are generated from a cathode ray tube by using electrons generated from the filament to bombard the target materials (Cu, Co et al). Characteristic X-rays can be generated as long as the electrons are strong enough to dislodge the inner shell electrons of target materials. The as-obtained X-rays are then going through the monochromatic filtering and concentrating before reaching the surface of the samples. The incident X-rays will interact with the crystal specimen and a diffracted X-ray is thus produced as long as the condition of Bragg's Law is satisfied, which is illustrated as followed:

$$n\lambda = 2d \sin \theta$$

The Bragg's Law reveals the relationship among the wavelength of X-ray, the lattice d-spacing in the target crystal material and the diffraction angle. The diffracted X-rays will be collected by the detector and processed by the calculating system and interpreted into

the XRD patterns. Since the materials are powders with random orientations, the sample is characterized through a scanning angle range of 2θ, where all possible diffracted X-rays from the lattice can be collected. Subsequently, the identification of the materials can be realized by the conversion of the diffraction peaks to d-spacings since each crystalline material possesses its own particular d-spacings, which is usually used as the standard reference patterns.

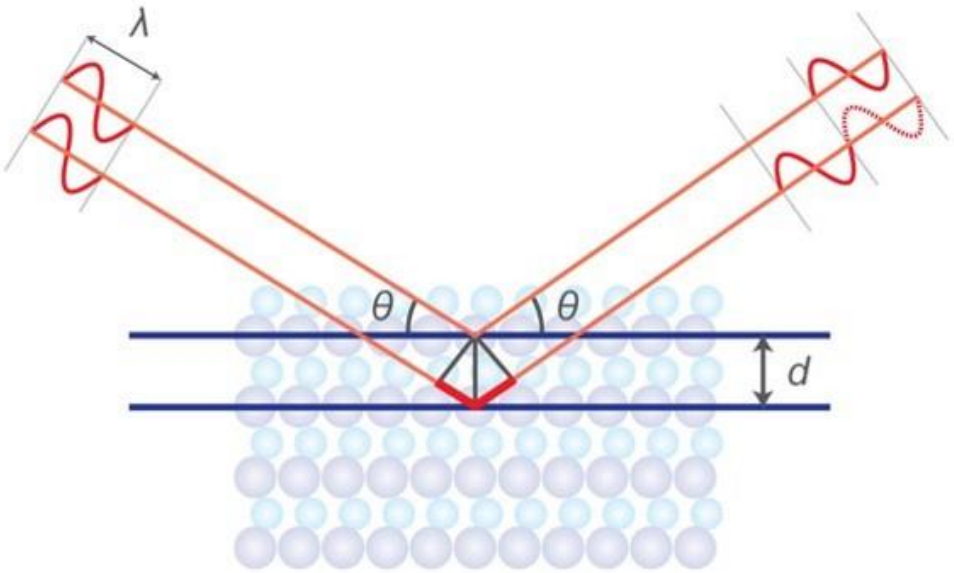

Figure 3.10 Mechanism of Bragg's Law in XRD measurement.[12]

3.3.5 X-ray photoelectron spectroscopy (XPS)

X-ray photoelectron spectroscopy (XPS) is a powerful technique that can provide quantitative analysis of the samples with various information such as elemental composition, chemical state, electronic state et al. within a material. Since the X-ray beam in XPS measurement is much weaker than the electron beams in SEM and TEM, the detected signals come from the outmost positions of the sample, which is from 0 to 10 nm deep.

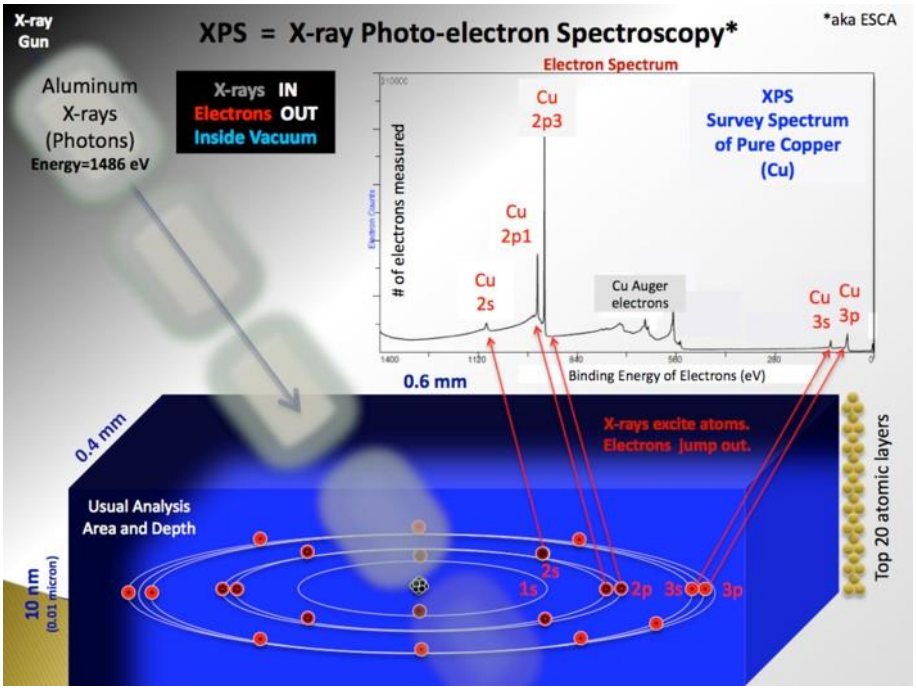

Figure 3.11 Rough schematic of XPS physics.[13]

The schematic of XPS physics is known as "Photoelectric Effect", as illustrated in Figure 3.11. The X-rays beam with a particular wavelength bombards the atoms of the sample and facilitates the jumping out of the electrons in the atoms. Since the energy of the X-ray beam is known (such as Al K_α X-rays, E_{photon}= 1486.7 eV) and the emitted electrons' kinetic energies can be measured by the analyzer, the electron binding energies of all the excited electrons could thus be calculated based on the equation below:

$$E_{binding} = E_{photon} - (E_{kinetic} + \phi)$$

where $E_{binding}$, E_{photon} and $E_{kinetic}$ correspond to the binding energy of the electron, the energy of the X-ray photons and the measured kinetic energy of the electron, respectively. ϕ is the working function that is determined by the material and spectrometer.

XPS has been widely employed to investigate the chemical states and make quantitative analysis of the nanomaterials. Specifically, "chemical state" is associated with the actual bonding environment of the investigating species, which can be influenced by oxidation

state of the species, the identity and the bonding hybridization status of the nearest neighbor atom et al. Due to the possible factors above, there may be a binding shift of the species in question compared to its nominal value for the binding energy of the target element. The measured chemical shift will provide more information about the chemical state of the species analysis.

3.3.6 Raman spectroscopy

Raman spectroscopy is a common technique in studying the chemistry of materials by providing a structural fingerprint on the basis of identified molecules. The Raman spectroscopy is based on inelastic scattering of monochromatic light, which comes from a laser source at different ranges. In the Raman system, the laser beam interacts with the molecular vibrations, phonons et al of the materials so that a positive or negative shift of the energy of the laser phonon appears, which will provide information on the mode of the molecular vibration in the system.[14]

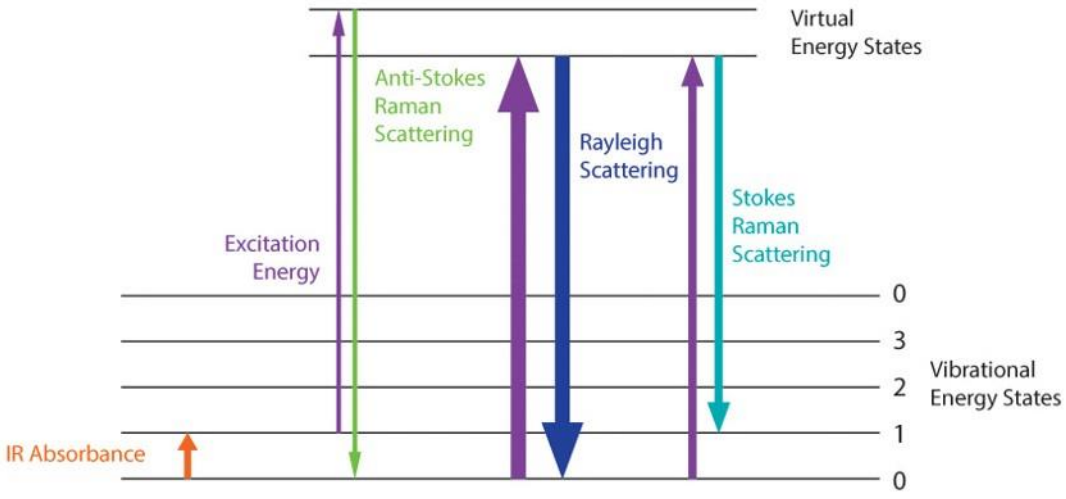

Figure 3.12 Energy-level diagram showing the states involved in Raman spectra.[14]

The polarizability of the electrons, which is caused by the interaction between the electron cloud of the specimen and the external electrical field of the laser beam, plays a very important role in the happen of Raman effect of a molecule. The magnitude of the Raman effect is determined by the intensity of the inelastic scattering by exciting the sample with

a photon. During the excitation process, the molecule can stays at a virtual energy state within a short time until the photon is emitted from the sample. After inelastic scattering, the sample will turn into another vibrational or rotational state since the energy of emitted photon is different from the incident photon, where either a higher or lower energy shift appears. If the energy of the final rovibronic states of a molecule is higher than its initial state, the emitted photon will turn to be with lower energy or frequency than the incident photon in order to maintain the total energy conservation, which is called Stokes shift. On the contrary, a higher shift of the scattered photon is called anti-Stokes shift (Figure 3.12).

3.3.7 Cyclic voltammetry (CV)

Cyclic voltammetry (CV) is a typical method in electrochemical measurement. Specifically, CV is to apply a linear potential with a constant scanning rate to the working electrode. When the scan reach the termination potential and continue the inverse scan to the starting potential as a cycle. When the scan is carried out from a lower potential to a high potential, anodic peaks may occur due to the oxidation process of the target material.[15] This technique can help us to determine the potential of the oxidation and reduction reactions on the working electrode.

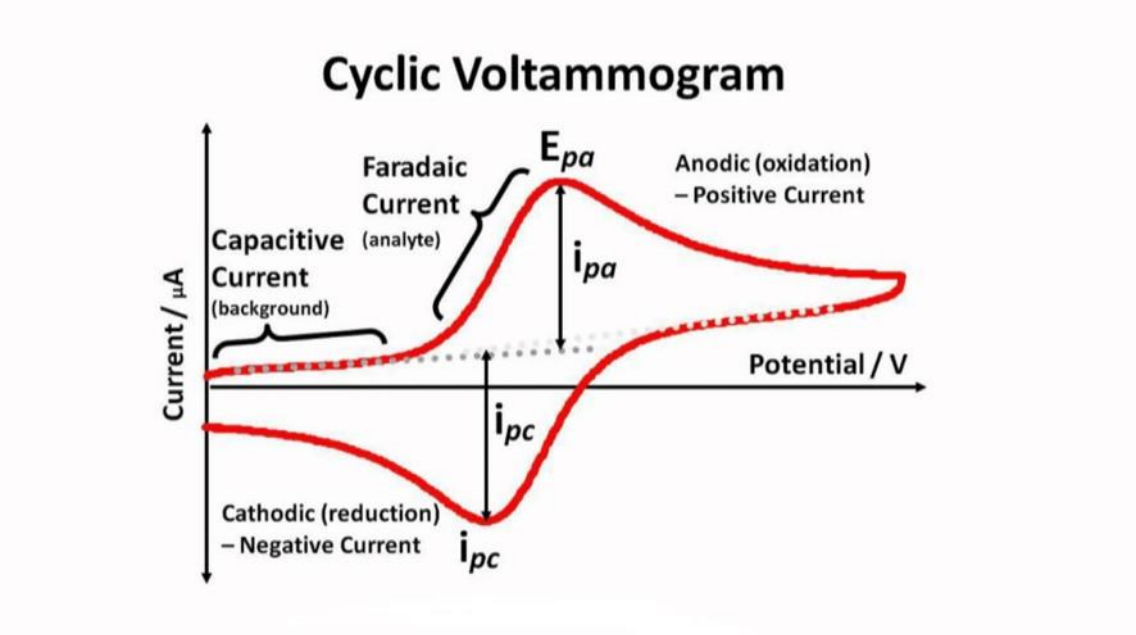

Figure 3.13 A typical CV profile.[15]

Figure 3.13 presents a typical CV profile of a simple system. For instance, the electrode reaction is

$$O + e^- \rightleftarrows R$$

Before the applied potential can drive the oxidation of O, there may be a capacitive current as the background. When the electrode potential approach positively to E_{pa}, specie O start to be oxidized on the electrode and thus a Faradaic current is generated. The oxidation reaction become more and more fierce with the increase of applied potential, resulting in the continuous increase of the current density on the electrode. At the same time, the concentration of O on the electrode will drop rapidly so that it turns to be much lower than the O concentration in the electrolyte due to the intense oxidation reaction. When the O concentration on the electrode becomes zero, the current density will not increase with the positive scanning of the potential but will be determined by the diffusion rate of O from the electrolyte to the electrode surface. Therefore, the current density will gradually drop ascribed to the decrease of the concentration gradient of O in the electrolyte so that an oxidation peak appears. In the reverse scan, the reduction of O (oxidation of R) will experience a similar process to the O oxidation process above to form a reduction peak. The whole profile is called cyclic voltammetry curve.

According to correlation of the values of summit current i_p, summit E_p, summit difference between i_{pa} and i_{pc}, and the scan rate, the reversibility could be determined through calculation.

3.3.8 Oxygen evolution reaction (OER)

The hydrogen evolution reaction (HER) and oxygen evolution reaction (OER) by electrochemical water splitting are regarded as promising approaches for the generation of renewable energies. During the past decades, various electrocatalysts have been applied to improve the efficiency of oxygen evolution. In order to develop high-efficiency catalysts for OER, it is significant to understand the principles of the oxygen evolution process on the anode.

There are many difficulties in investigating the oxygen evolution reaction since the process is a poly-electron electrochemical reaction involving many intermediate steps and products. Furthermore, the oxygen evolution reactions in acidic media and alkaline media are different:

In acid electrolyte: $2H_2O \rightleftarrows O_2 + 4H^+ + 4e^-$

In alkaline electrolyte: $4OH^- \rightleftarrows O_2 + 2H_2O + 4e^-$

Under a certain current density (j), the difference between the practical potential of oxygen evolution (φ_i) and its equilibrium potential (φ_e) is called overpotential (η_o)of oxygen evolution:

$$\eta_o = \varphi_i - \varphi_e$$

Usually, under a constant current density j, η_o tend to increase with the increase of the reaction time due to the formation of the oxide layer on the surface of the working electrode. As a result, the η_o is generally referred to its average value.

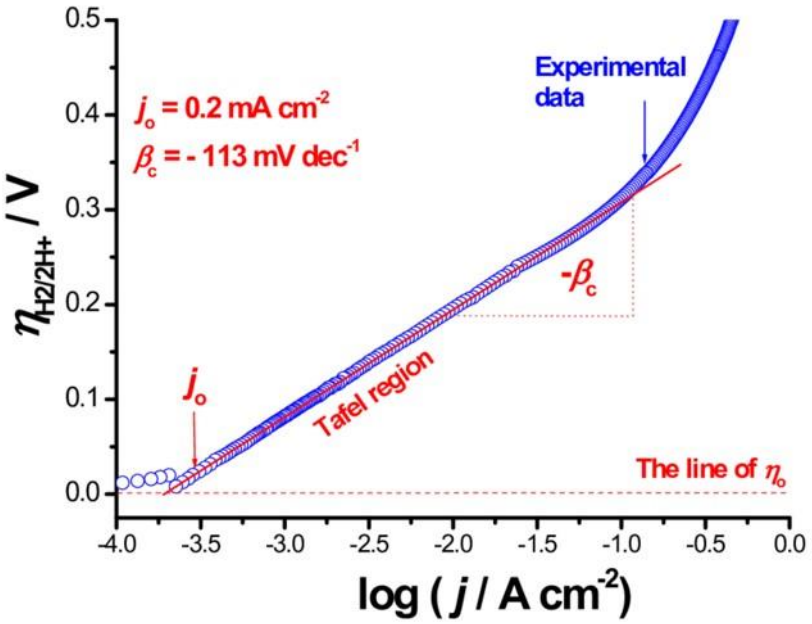

Figure 3.14 Tafel equation fitting the red solid line to the experimental curve.[16]

The overpotential and the current density follow the Tafel equation:

$$\eta_o = a + b \log j$$

where constants a and b are dependent to the type of electrode material, temperature, the composition of the electrolyte and the value of current density. And the slope of the curve has different values at different sections.

In alkaline solutions, the order for the overpotentials on metals is as followed: Co< Fe< Ni< Cd< Pb< Au< Pt. The difference of overpotential between Pt and Co is as high as 0.7 V. As shown in Figure 3.14, a Tafel region is found to present during the electrochemical polarization. The formation of this linear region is controlled by the discharge of O^-. A lower Tafel slope indicates a better kinetics for OER.

References

[1] Bhanushali, S.; Ghosh, P.; Ganesh, A.; Cheng, W., *Small* **2015,** 11 (11), 1232-1252.

[2] Guo, Y.-G.; Wan, L.-J.; Zhu, C.-F.; Yang, D.-L.; Chen, D.-M.; Bai, C.-L., *Chem. Mater.* **2003,** 15 (3), 664-667.

[3] Huan, T. N.; Rousse, G.; Zanna, S.; Lucas, I. T.; Xu, X.; Menguy, N.; Mougel, V.; Fontecave, M., *Angew. Chem.* **2017,** 129 (17), 4870-4874.

[4] Wang, X.; Han, G.-R., *Microelectron. Eng.* **2003,** 66 (1-4), 166-170.

[5] Aastrup, T.; Wadsak, M.; Leygraf, C.; Schreiner, M., *J. Electrochem. Soc.* **2000,** 147 (7), 2543-2551.

[6] Fernandez, D.; Maurer, P.; Martine, M.; Coey, J.; Möbius, M. E., *Langmuir* **2014,** 30 (43), 13065-13074.

[7] Kitagawa, S., *Chem. Soc. Rev.* **2014,** 43 (16), 5415-5418.

[8] Kisielowski, C.; Freitag, B.; Bischoff, M.; Van Lin, H.; Lazar, S.; Knippels, G.; Tiemeijer, P.; van der Stam, M.; von Harrach, S.; Stekelenburg, M., *Microsc. Microanal.* **2008,** 14 (05), 469-477.

[9] Van Loan, C., Computational frameworks for the fast Fourier transform. *Siam*: **1992**; Vol. 10.

[10] Fultz B, Howe J M. Transmission electron microscopy and diffractometry of materials[M]. *Springer Science & Business Media*, **2012**.

[11] Reimer L. Scanning electron microscopy: physics of image formation and microanalysis[M]. *Springer*, **2013**.

[12] Jenkins R, Snyder R L. Diffraction theory[M]. *John Wiley & Sons, Inc.*, **2012**.

[13] Watts J F. X-ray photoelectron spectroscopy. *Surface science techniques*, **1994**: 5-23.

[14] Long, D. A.; Long, D., Raman spectroscopy. *McGraw-Hill New York*: **1977**; Vol. 206.

[15] Kissinger, P. T.; Heineman, W. R., *J. Chem. Educ.* **1983,** 60 (9), 702.

[16] Modern aspects of electrochemistry[M]. *Springer Science & Business Media*, **2012**.

Chapter 4

Electrochemical behavior of single crystalline CuNWs

In this chapter, single crystalline CuNWs are synthesized by electrodeposition into AAO template. The diameter of the as-prepared CuNWs is ~ 50 nm. Their electrochemical behaviors in atmospheric air and alkaline solution are subsequently studied. The TEM characterization reveals that, a uniform compact Cu_2O layer is formed as a function of exposure time following the logarithmic law and epitaxially covers the CuNW surfaces in 40% RH atmosphere. It is also found that the oxide layers on CuNWs are sequentially grown when subjected to the cyclic voltammetry measurement in 0.1 M NaOH solution.

*This section published substantially as: The Electrochemical Response of Single Crystalline Copper Nanowires to Atmospheric Air and Aqueous Solution (Small, 2017, 13(10), 1603411.)

4.1 Introduction

Copper, one of the most commonly used metals, is playing critical roles in electronic devices due to its excellent physical properties. By taking advantages of the high electrical and thermal conductivity, copper nanowires (CuNWs) show promising applications in constructing high performance transparent conductive electrodes,[1-3] polymer solar cell,[4] chemical nanosensor,[5] lithium ion battery conductive agent[6] and heat dissipation devices.[7] It is well known that nanomaterials possess large surface-to-volume ratio, leading to higher proportion and reactivity of surface atoms than the counterpart bulk materials. So, the surface atoms of CuNWs are more sensitive to surrounding environment and likely to react with the chemical species, which will cause deteriorations of the composition and performance of CuNWs in the practical applications. Therefore, it is of great importance to study the chemical stability of CuNWs when they are exposed to environments.

Surface passivation is a self-protection behavior by forming a thin layer (usually several nanometers thickness) on the metal surface. Studying the evolutions of the composition and structure of the surface passivation film on the metal exposed in different gaseous[1, 8-12] or liquid[13-19] corrosive environments are helpful to understand the degradation mechanism of metals. Direct observations of the microstructure and crystalline orientations of the surface passivation film on the metallic nanomaterials are essential to understand its growth and formation mechanism in various corrosive environments. It is well known that transmission electron microscope (TEM) has the powerful capacity to direct observe the microstructure details of materials with high resolution. Therefore, it can be conveniently used to study the surface passivation behaviors on CuNWs.

Herein, we firstly fabricate high quality single crystalline CuNWs with uniform diameter by electrochemical depositing Cu inside the nanochannels of anodic aluminum oxide (AAO) template. Subsequently, TEM examinations on CuNWs were conducted on completion of their atmospheric (in 40 % relative humidity (RH)) and electrochemical (0.1 M NaOH solution) exposure, respectively. According to the TEM observation results, it is

found that a uniform compact cuprous oxide (Cu_2O) layer epitaxially covers the surface of CuNWs when exposed in 40 % RH atmosphere. With the increase of exposed time, the formed Cu_2O passivation layer on CuNWs gradually thicken complying with a logarithmic law relationship, while showing rapider growth rate than that of Cu_2O layer on the counterpart bulky copper. Cyclic voltammetry was performed to study the formation and evolution of the passivation film on CuNW in alkaline NaOH aqueous solution. A epitaxial Cu_2O layer firstly coat on the CuNWs under the low anodic potential and then further oxidized into disordered $CuO/Cu(OH)_2$ outer layer when increasing the anodic potential prior to the occurrence of oxygen evolution. The growth orientation of the ordered Cu_2O inner layer at low anodic potential is found to be parallel to the CuNW substrate under a solid-state reaction (SSR) mechanism. In contrast, the disordered $CuO/Cu(OH)_2$ outer layer appears random orientation following a dissolution-redeposition (DR) formation mechanism. Through the study of the surface passivation behaviors of CuNWs, it can present the guidance and insights into the surface protection and anti-corrosion of CuNWs in the practical applications.

4.2 Experimental Methods

4.2.1 Preparation of AAO template

The AAO templates with straight nanochannels were fabricated by using a two-step anodizing process we reported previously (anodized at 40 V in 0.3 M oxalic acid solution at 10 °C, the pore diameter of nanochannels of AAO template is about 50-60 nm).[20] The back thin Al_2O_3 barrier layer of the AAO template need to be removed in 5 wt % H_3PO_4 solution (40 °C) so as to obtain the through-hole AAO template.

4.2.2 Electrodeposition of CuNWs

A gold layer (~200 nm thickness) was sputtered onto one planar surface of the through-hole AAO templates to completely cover the pores and serve as working electrode. The electrolyte for deposition of CuNWs contains 0.2 M $Cu(NO_3)_2$, 0.1 M H_3BO_3 and 0.05 M

ethylenediaminetetraacetic acid. ECD of Cu NWs inside the nanochannels (~ 50 nm) of AAO templates was performed under a constant 1.3V deposition voltage for 30 mins, where an AAO template and a graphite rod were used as cathode and anode, respectively. The as-prepared CuNWs were released by removing of the AAO template in 2 M NaOH solution at 45 °C for 1 hour. The obtained CuNWs were immersed in 1M HCl solution for 10 min to thoroughly remove the possible surface oxide layer. The schematic of the preparation process of CuNWs is illustrated in Figure. 4.1.

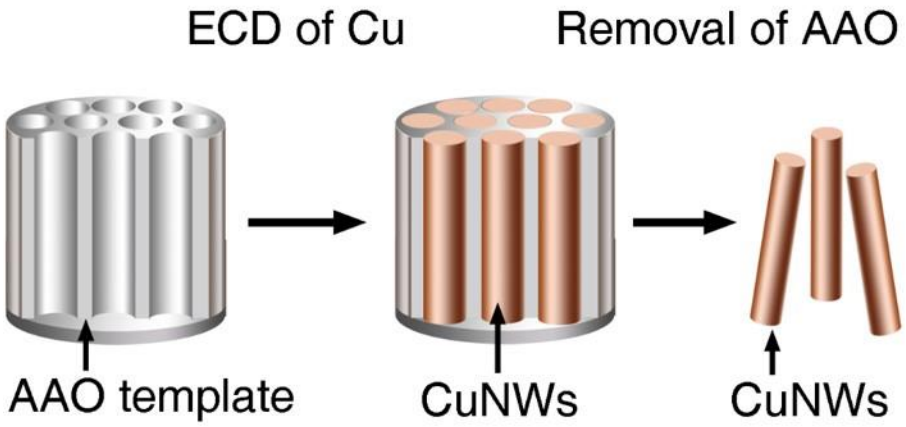

Figure 4.1 Schematic of the fabrication of CuNWs by AAO template strategy.

4.2.3 Stability test of CuNWs in 40% RH atmosphere

The CuNWs were dispersed on a copper grid and then placed in a cabinet with constant 40 % RH condition at room temperature, followed by TEM observations on different CuNWs with 3, 6, 24, 48 and 96 hours exposure durations, respectively.

4.2.4 Electrochemical measurement of CuNWs in 0.1 M NaOH solution

Screen-printed electrodes (SPEs, DRP-110, DropSens, Spain), which include a carbon counter electrode and a silver solid pseudo reference electrode, were employed to set up the electrochemical system (Figure 4.2). CuNWs were dispersed in 0.1 M NaOH solution then dropped on SPEs as working electrode. Cyclic voltammetry measurement was carried

out by AUTOLAB PGSTAT 302N (Metrohm Pte Ltd.) at room temperature (25 ± 1 °C) with a scan rate of 10 mV/s. The CuNWs that had been electrochemically polarized to different potentials were rinsed and dried before being transfered into TEM.

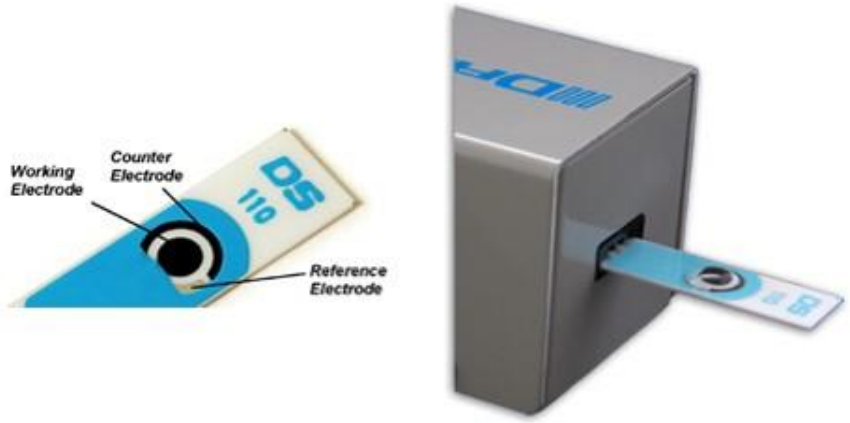

Figure 4.2 Sketch of the Screen-printed electrodes.

4.2.5 Transmission electron microscopy (TEM)

As the most important equipment in the thesis project, two TEM instruments JEOL JEM 2010 and JEM 2100F with 200 kV accelerating voltage were employed to collect the (HR)TEM images. TEM was used to characterize the CuNWs before and after atmospheric exposure and electrochemical treatment experiments. By charactering the oxide layers on the CuNWs, the structure and composition of the oxide species coupled with their orientation relationship could both be clarified based on the FFT patterns that were derived from the HRTEM images, which contributed to the revelation of the electrochemical oxidation mechanism of the CuNWs in alkaline solutions. To ensure the accuracy of the results, TEM characterizations were carried out on more than five CuNWs for each case.

4.2.6 Powder X-ray diffraction (XRD)

X-ray powder diffractometer (Bruker D8 Advance, Germany) with Cu Kα radiation (λ=1.5406 Å) was employed to characterize the phase information of the as-fabricated CuNWs and confirm the purity of the CuNWs before the electrochemical measurements.

4.3 Principle Outcomes

4.3.1 Electrochemical behavior of CuNWs in 40% RH atmosphere

After thoroughly removing the possible surface oxide of the as-prepared NWs samples in dilute HCl aqueous solution, NWs with extremely clean surface are obtained. As shown in the low-magnification bright-field TEM image (Figure 4.3a), the as-obtained NWs present uniform diameter (~ 50 nm) and smooth surface. HRTEM image of one typical NW (Figure 4.3b) clearly displays the extremely clean surface of the NW without any oxidation. Furthermore, the fast fourier transform (FFT) patterns of the NW (inset in Figure 4.3b) illustrate the single crystalline nature of the resultant NW in the projection plane of {1 0 1}.

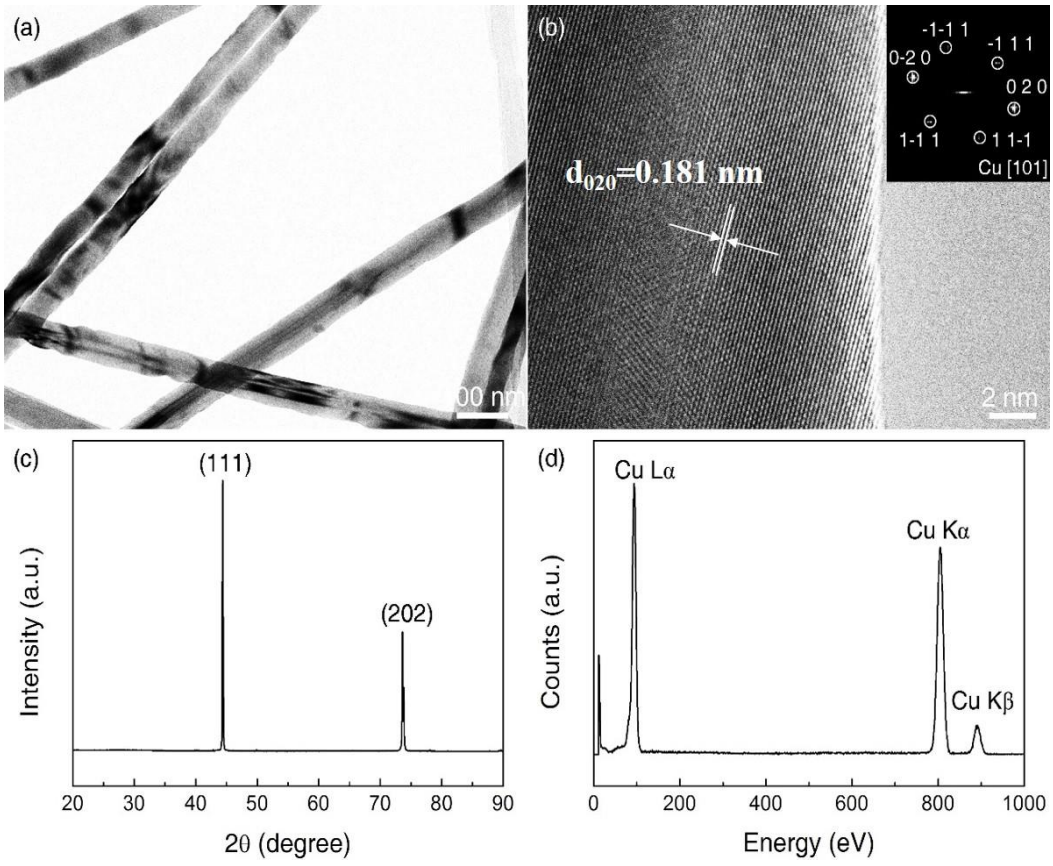

Figure 4.3 (a) Low-magnification TEM image of the as-fabricated CuNWs; (b) HRTEM image of one typical CuNW and the inset shows the FFT pattern of the CuNW; (c) XRD patterns of the samples embedded in AAO template; (d) EDX spectrum of the CuNW.

X-ray diffraction (XRD) pattern of the samples (Figure 4.3c) reveals the sharp diffraction peaks that can be indexed to (1 1 1), (2 0 2) planes of metallic Cu with cubic phase, being consistent with the standard values of Cu (JCPDS 00-003-1015). Energy dispersive X-ray spectrum (EDX) measurement (Figure 4.3d) in TEM confirms the obtained NW is purely composed of Cu. These results indicate that the obtained product is single crystalline CuNWs without any surface oxide.

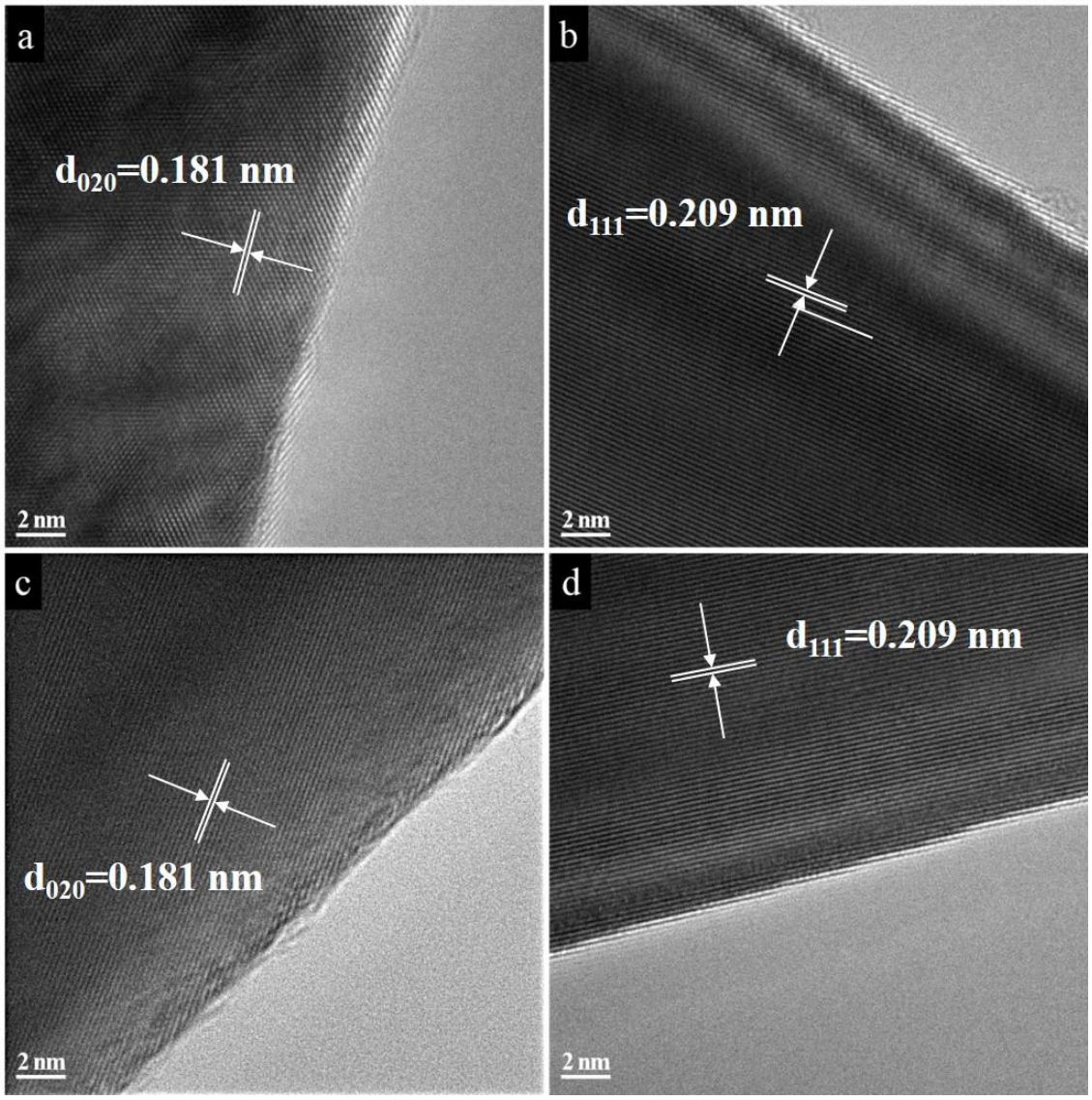

Figure 4.4 HRTEM images of fresh CuNWs. (a)- (d) correspond to II-V, respectively.

In order to minimize the damage to surface oxide films caused by the repeated TEM observation on the same one CuNW under high-energy electron beams, we chose five

different CuNWs (I- V) located on the TEM grid to study the surface oxide films. HRTEM image of sample I is illustrated Figure 4.5a in order to make direct comparison with its HRTEM image after 3 hours' exposure. The other four different CuNWs samples (II- V) (shown in Figure 4.4) also clearly demonstrate their extremely clear surfaces without any oxidation before the exposure experiment.

Figure 4.5b shows the HRTEM image of CuNW sample I after being exposed to 40 % RH atmosphere for 3 hours. From the lattice-resolved HRTEM image in Figure 4.5b, the oxide film is easily distinguished and d-spacing differences from the inner Cu substrate in the phase contrast. The discontinuous feature of the film (Figure 4.5b) indicates that it is at the initial nucleation/growth stage. The composition of the oxide film is identified to be Cu_2O by indexing the FFT pattern (inset in Figure 4.5b). In addition, the surface Cu_2O film is epitaxially grown along the {1 1 1} planes of the inner CuNWs substrate and mismatch due to the slight different d-spacings between them results in dislocations across their interface.

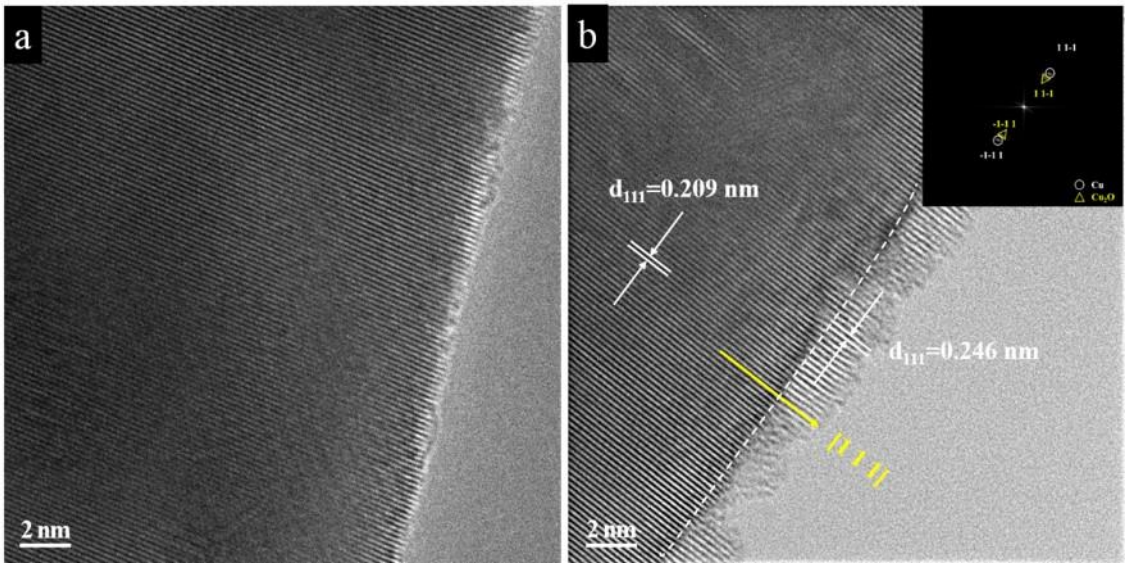

Figure 4.5 HRTEM images of (a) the fresh CuNW (I) and (b) after it was exposed to air for 3 hours.

The panels a- d of Fig 4.6 show the HRTEM images of the CuNWs samples II-V after being exposed to 40% RH atmosphere for 6, 24, 48 and 96 hours, respectively. With the 6 hours' exposure, the epitaxial Cu_2O surface oxide film on sample II (Figure 4.6a) becomes

slightly thicker and more uniform than the passive film that are formed after 3 hours, which can be easily distinguished by the contrast between the CuNW substrate and its adjacent copper oxide film. According to the HRTEM images in Figure 4.6b-d, it is seen that the thickness of the formed Cu_2O film will continuously increase with further exposure (up to 24, 48, 96 hours) in 40 % RH atmosphere. Meanwhile, it is worth to note that the epitaxially grown Cu_2O films for different CuNWs samples (II- V) are all oriented in perfect parallel to the CuNWs substrate planes, i.e.{1 0 0}, {1 1 0}and {1 1 1}, respectively. This suggest the fact that the growth of Cu_2O films on CuNWs in 40% RH atmosphere is always epitaxial to the CuNWs substrate with any exposed facet.

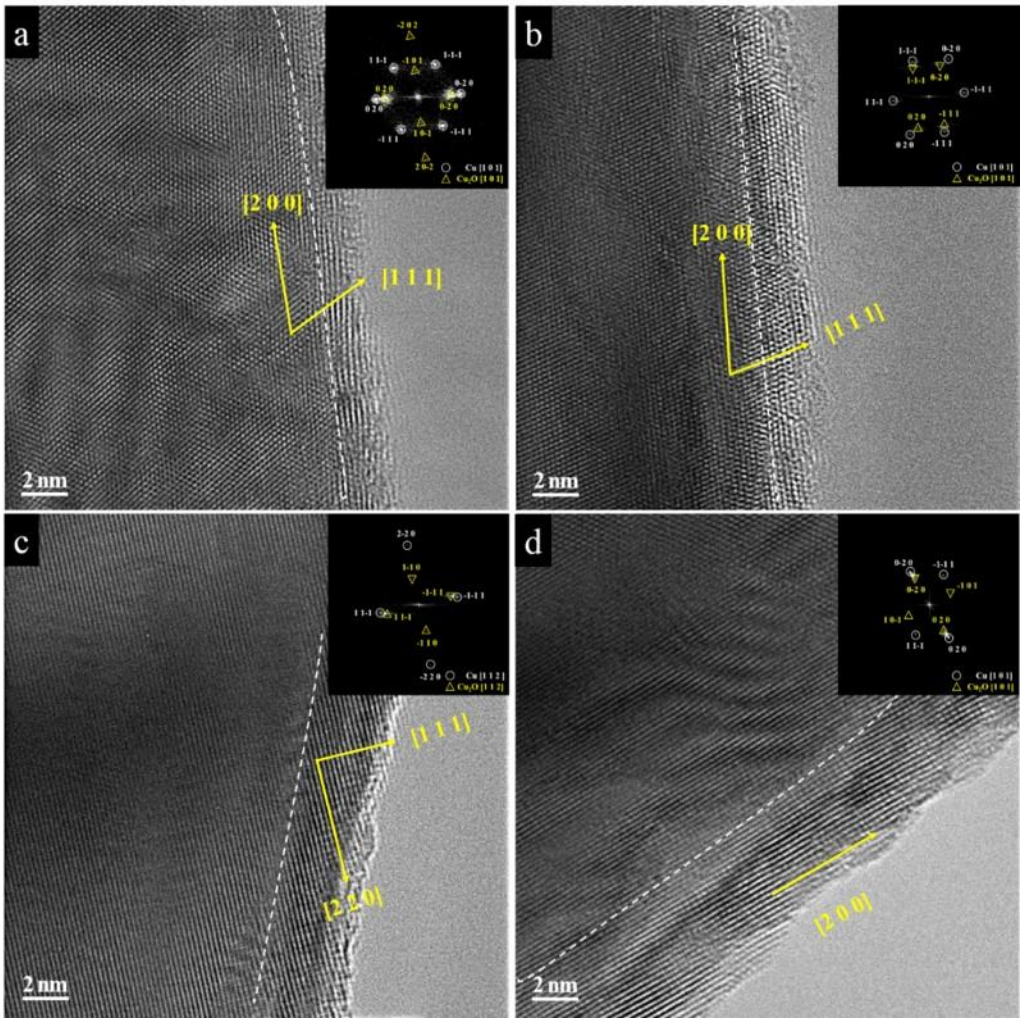

Figure 4.6 HRTEM images of CuNWs II-V after being exposed in air 40% RH after (a-d) 6, 24, 48, and 96 h, respectively. Each inset on the top right corner is the corresponding FFT patterns. The white dotted line in each panel represents the interface between the outer layer and the inner CuNW substrate.

Based on the measurement of the thickness of Cu_2O films from TEM images, the growth rate of Cu_2O films on CuNWs exposed to 40% RH atmosphere (Figure 4.7) follow approximately a logarithmic law relationship as below:

$$T=1.028+0.064\times\ln(t+0.02) \quad (1)$$

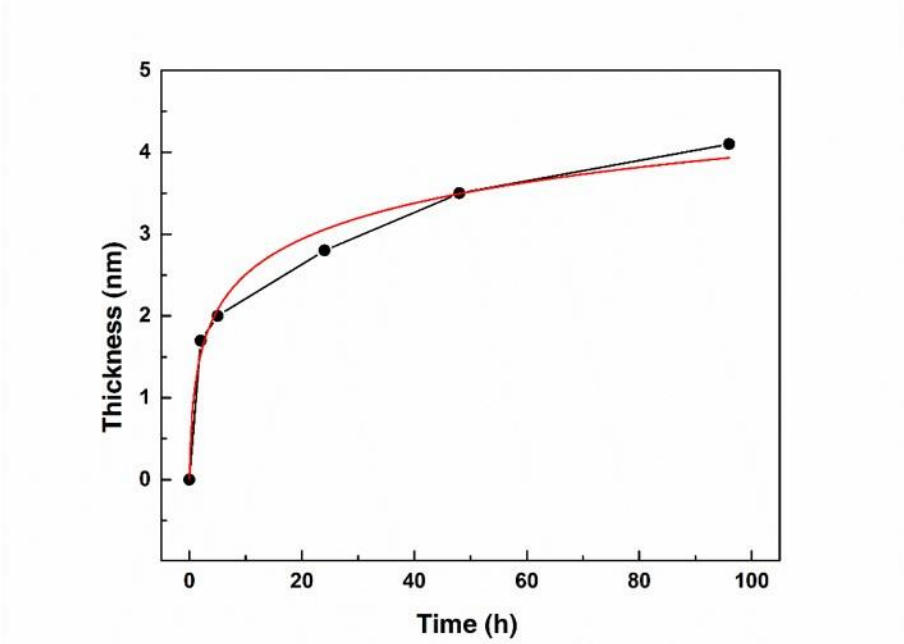

Figure 4.7 Experimental plots and fitting curve of the film thickness on CuNWs *vs* the exposure time in 40% RH atmosphere.

where T and t correspond to the film thickness and the exposure time, respectively. This is similar to the thickness increase relationship of the oxide films on bulk copper materials in the air.[8] The gradual decreased growth rate of the film demonstrates that the formed Cu_2O film is able to provide the protection and therefore slow down the further oxidation of the CuNWs. The growth and evolution of Cu_2O layer on CuNWs follow the electrochemical process-a thin electrolyte film is initially formed on top of the CuNWs surface, and then two separate reactions will happen as followed, respectively.

Cathodic reaction: $O_2 + 2H_2O + 4e \rightarrow 4OH^-$ (2)

Anodic reaction: $Cu \rightarrow Cu^{2+} + 2e$ (3)

Since the CuNWs were exposed to 40 % RH air, the electrolyte film on the CuNW surface is so thin that only limited amount of oxygen could be dissolved into the electrolyte, leading to the inhibition of cathodic reaction (2) and the gradually decreased film growth rate on CuNWs surface. As reported previously, the Cu_2O film thickness on the bulky Cu is only 0.2 nm after 24 hours' exposure to 40% RH air. In contrast, the growth rate of Cu_2O films on CuNWs is much higher than that situation on the counterpart bulky copper under the same condition (2.7 nm thickness Cu_2O on CuNWs when exposed in 40 % RH air for 24 hours), which is apparently attributed to the higher reactivity of the surface atoms on CuNWs than the bulky Cu.

4.3.2 Electrochemical behavior of CuNWs in 40% RH atmosphere

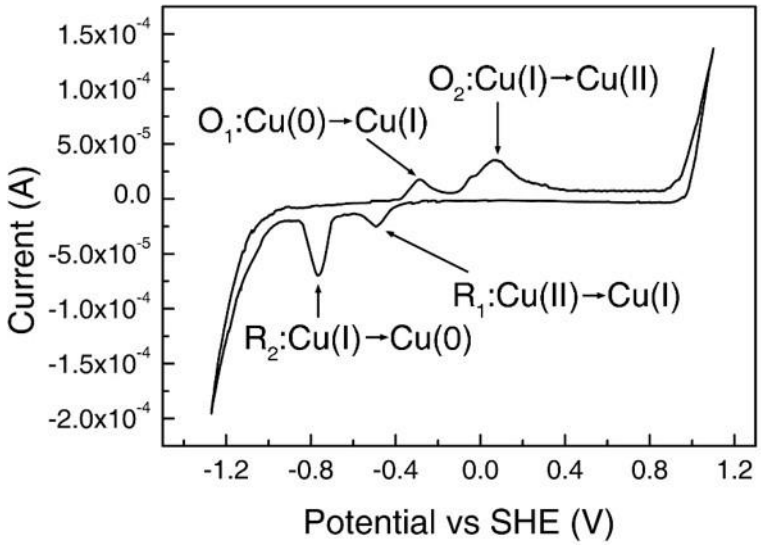

Figure 4.8 A cyclic voltammetry profile of CuNWs in 0.1 M NaOH aqueous solution.

Cyclic voltammetry (CV) was carried out to study the electrochemical properties of CuNWs in 0.1 M NaOH aqueous solution. The forwards can ranges from the potential of –1.27 V to +1.1 V, followed by the reverse scan back to the onset potential (–1.27 V). The scan rate in the whole process is constantly set at 10 mV/s. As shown in the cyclic voltammogram (Figure 4.8) after a single complete cyclic scan, there are two anodic peaks(O_1 andO_2) and two cathodic peaks (R_1 and R_2) in the potential range between hydrogen and oxygen evolutions, which refer to the oxidation and reduction processes occurring on the CuNWs surface[8]. The two oxidation peaks O_1 and O_2 in the CV profile

mainly correspond to the formation of Cu(I) and Cu(II) specimens. The R_1 and R_2 reduction peaks in CV profile are associated with the reductions of Cu(II) to Cu(I) and Cu(I) to Cu (0), respectively. Comparing to the CV profile of bulk copper materials scanned in 0.1 M NaOH aqueous solution under the same scanning rate,[13] the oxidation peaks of CuNWs are shifted to the more negative potentials, suggesting the higher reactivity of CuNWs than the bulky counterpart.

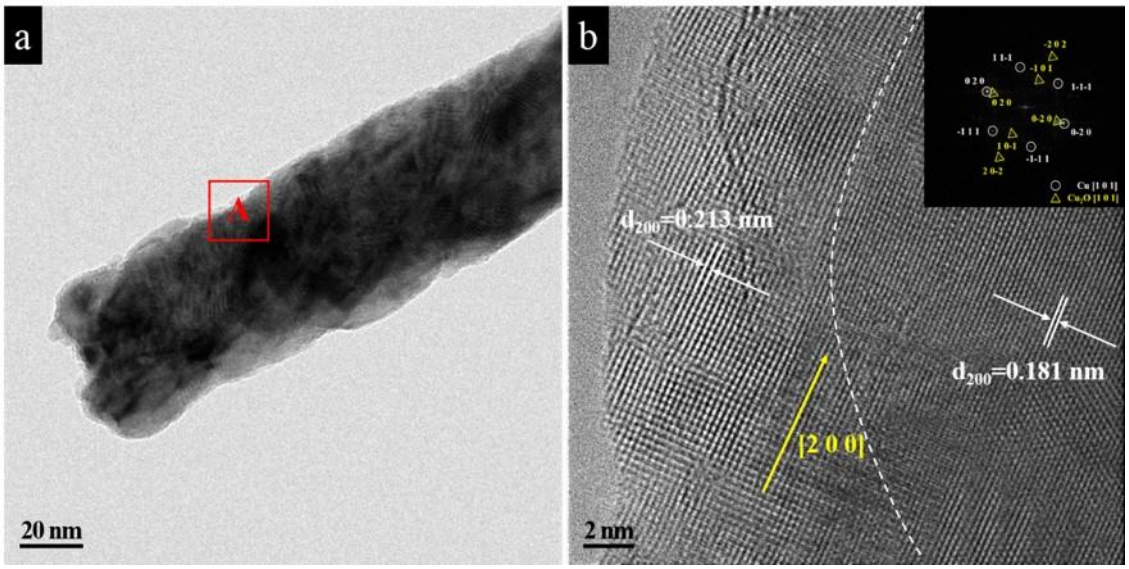

Figure 4.9 (a) Low- magnification TEM image of one typical CuNW after being polarized to –0.15 V; (b) HRTEM image of the square A in panela and the inset on the top right corner is the corresponding FFT pattern.

To investigate the formation and evolution of the surface oxide films on CuNWs, three different groups of CuNWs were used for electrochemical polarization to –0.15 V (behind O_1 peak), +0.45 V (behind O_2 peak), and +0.8 V (prior to the occurrence of oxygen evolution), respectively. After the electrochemical oxidation for the CuNWs by sweeping the different anodic potential, the obtained samples were immediately centrifuged, washed and dispersed in absolute ethanol, and dried for a short time in vacuum desiccators prior to the TEM characterizations. Figure 4.9a is the bright-field TEM image of one typical CuNW electrochemical polarized to –0.15 V (beyond the first oxidation peak O_1) in 0.1 M NaOH solution, showing the rougher surface comparing to the surface morphology of the as-obtained smooth CuNWs, which is brought about by the formation of oxide film. The composition and structure of the film is revealed to be Cu_2O from the HRTEM image

Figure 4.9b, which is taken from the square region A in Figure 4.9a. Importantly, the FFT patterns (Figure 4.9b) suggest that the epitaxial Cu_2O film growth orientation is along (2 0 0) and parallel to the (2 0 0) direction of the inner Cu substrate. The formation of this ordered Cu_2O layer is ascribed to the SSR mechanism, where the surficial reaction takes place between Cu and OH^- as following:

$$2Cu + 2OH^- \rightarrow Cu_2O + H_2O + 2e \quad (4)$$

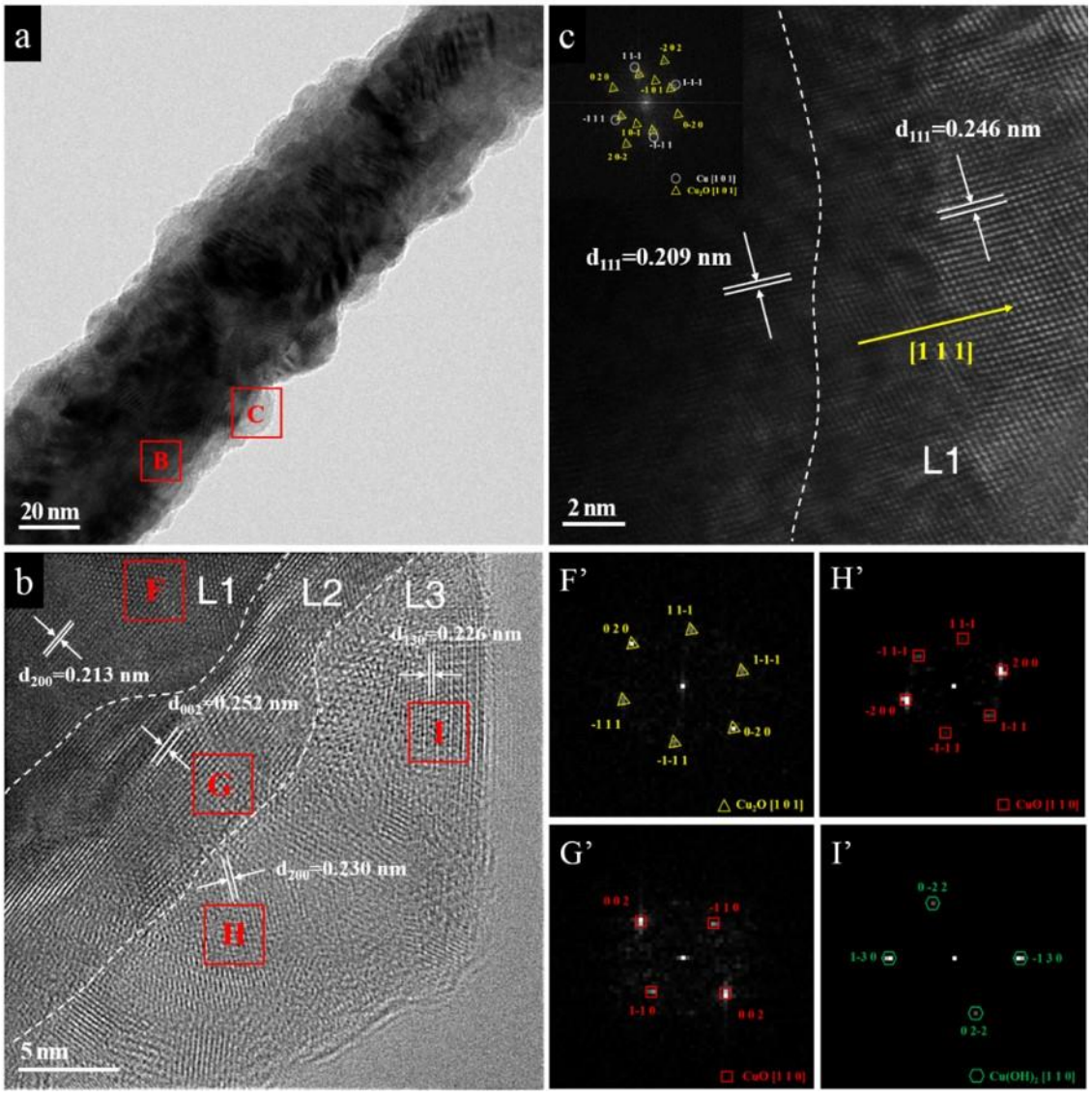

Figure 4.10 (a) Low- magnification TEM image of one typical CuNW after being polarized to + 0.45 V. (b) and (c) are the HRTEM images taken from the marked areas B and C in panel c. The FFT patterns (F', G', H' and I') correspond to the marked area F, G, H and I in panel e.

In addition, the Cu_2O film on CuNWs at this potential (– 0.15 V) is much thicker than that on the bulk copper sample at even more positive potentials (+ 0.8 V)[13], indicating the higher surface reactivity of CuNWs.

When the polarization potential reaches the potential (+ 0.45 V) behind peak O_2, the surface of CuNW appears much rougher as shown in Figure 4.10a. The surface oxide film on CuNW consists of three layers, which are labelled in Figure 4.10b as L1, L2 and L3.The analysis of the respective three layers is performed by indexing their corresponding reciprocal lattices. F' and G' are FFT patterns collected from the L1 and L2 in the marked square areas F and G in Figure 4.10b are indexed and they are determined to be generated from Cu_2O and CuO, respectively. It is also determined that the CuO layer (L2) is epitaxial with Cu_2O layer (L1) in the projection lattice plane of {2 0 0}. The growth of this epitaxial CuO layer is attributed to the following reaction under SSR mechanism:

$$Cu_2O + 2OH^- \rightarrow 2CuO + H_2O + 2e \quad (5)$$

Further analysis shows that the Cu_2O layer (L1) has also parallel orientation relationship (i.e. {1 1 1} lattice plane) with the CuNW matrix, as proved by the HRTEM image (Figure 4.10c). The formation of the L1 also follows the SSR mechanism as shown in equation (4).[21] H' and I' are two FFT reciprocal patterns that are transformed from L3 in the areas marked as H and I in Figure 4.10d, which are identified to be reflected from randomly oriented CuO and $Cu(OH)_2$, respectively. This indicates that L3 is a polycrystalline layer and consists of $Cu(OH)_2$ incorporated with CuO nanocrystals. The formation of the L3 is probably governed by a DR mechanism. In the typical DR process, CuO and $Cu(OH)_2$ are generated in the solution near the CuNWs surface through the possible reactions as followed:

$$Cu + 2OH^- \rightarrow CuO + H_2O + 2e \quad (6)$$

$$Cu + 2OH^- \rightarrow Cu(OH)_2 + 2e \quad (7)$$

The formation sequence of Cu_2O and CuO can also be explained in thermodynamics view

point:

The Gibbs free energies of the substances involved in the electrochemical reactions are listed in the table below:

Table 4.1 Gibbs free energies of the substances involved in the electrochemical reactions.

Substance (form)	Gibbs at 298K Δ_fG (kJ)
OH^-(aq)	-157.30
H_2O(l)	-237.192
Cu(g)	301.4
Cu_2O	−550.01
CuO	−307.002

The formation of Cu_2O follows the reaction (4): $2Cu + 2OH^- \rightarrow Cu_2O + H_2O + 2e^-$, in which Δ_fG_4= -550.01+ (-237.192) - [2*301.4+ 2*(-157.30)] = -1075.402 kJ;

The formation of CuO follows the reaction (6): $Cu + 2OH^- \rightarrow CuO + H_2O + 2e^-$, in which Δ_fG_6= -307.002+ (-237.192) - [301.4+ 2*(-157.30)] = -530.994 kJ.

According to the calculated Δ_fG of the reactions above, the Cu_2O-formation reaction with lower Δ_fG suggests that it is easier to take place since less energy is required.

Subsequently, the obtained species will redeposit onto the CuNWs surface forming L3.[13,20] As a result, the oxide film formed on CuNW subject to the high potential of + 0.45 V becomes much thicker than the thickness of the film formed on CuNW at the low potential of – 0.15 V.

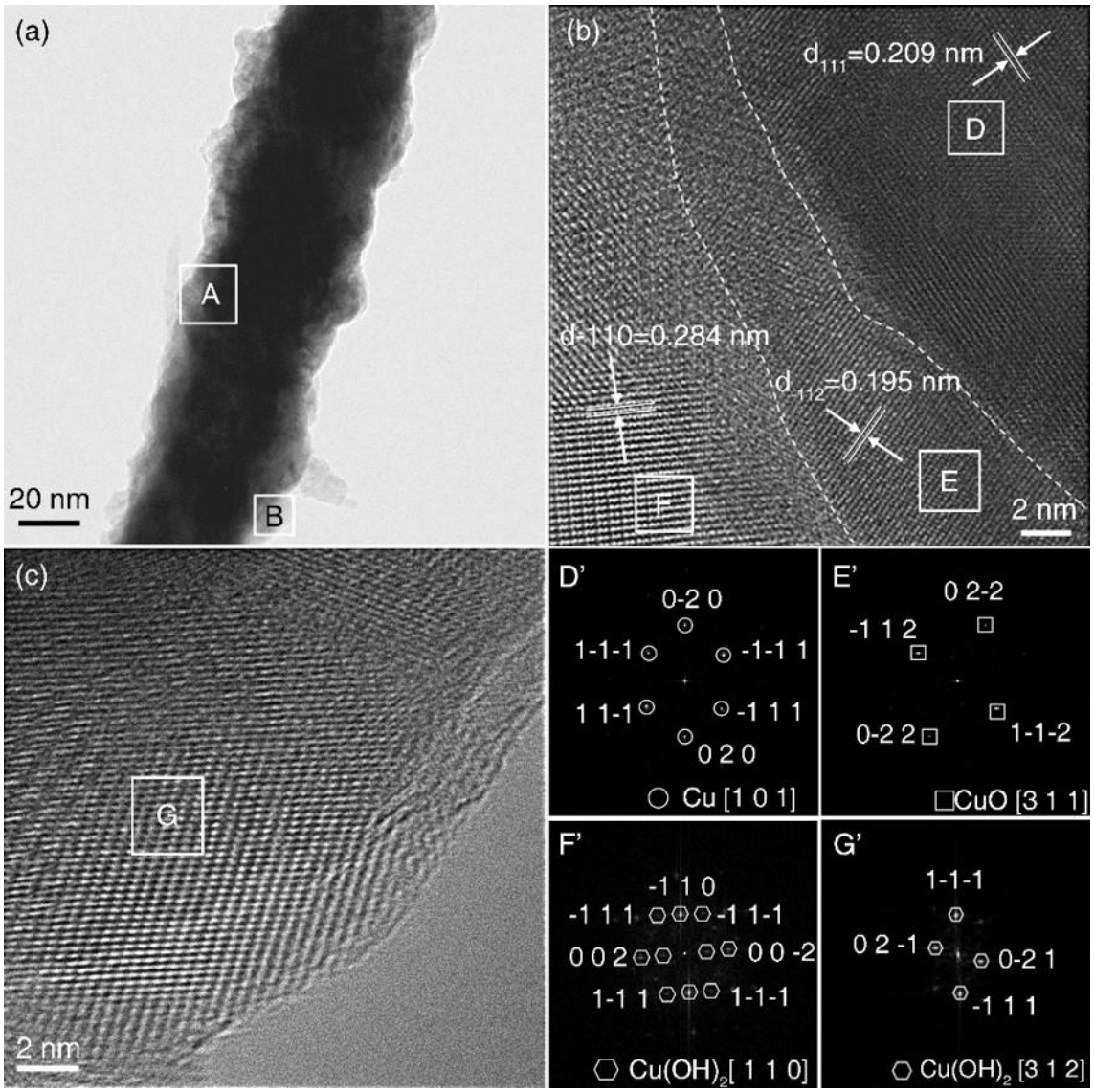

Figure 4.11 (a) Low- magnification TEM image of one typical CuNW after being polarized to + 0.8V; (b) and (c) HRTEM image of the square A and B in panela. The FFT patterns (D', E', F', and G') correspond to the marked area D, E, F in panel b and region G in panel c, respectively.

When the polarization potential rises up to + 0.8 V prior to the occurrence of oxygen evolution, the oxide film on CuNW appears less uniform (see TEM image in Figure 4.11a) than those formed at low potentials. The surface of CuNW is observed to be much rougher where the peaks and troughs are clearly visible. Figure 4.11b is a HRTEM image taken from the square area marked as A in Figure 4.11a, which shows double oxide layers (i.e. inner layer and outer layer). No orientation relationship is found between these two layers. The inner layer is identified to be CuO by indexing FFT pattern (Figure 4.11E'), equivalent

to L2 in Figure 4.10b. The analysis of FFT patterns generated from this area (Figure 4.11F' and G' taken from the square areas marked as F in Figure 4.11b and G in Figure 4.11c) demonstrates that outer layer, identical with L3 in Figure 4.10c, only consists of $Cu(OH)_2$. There is lack of L1-like layer in Figure 4.11b, which is due to the complete conversion of Cu_2O to CuO through the reaction equations of (5) above. CuO and $Cu(OH)_2$ are also the products of the reactions between Cu and OH^- through the equation (6) and (7). Meanwhile, the hydration and dehydration processes are responsible for the formation of $CuO/Cu(OH)_2$ double-layer structure[21], i.e.

$$CuO+H_2O \rightleftarrows Cu(OH)_2 \quad (8)$$

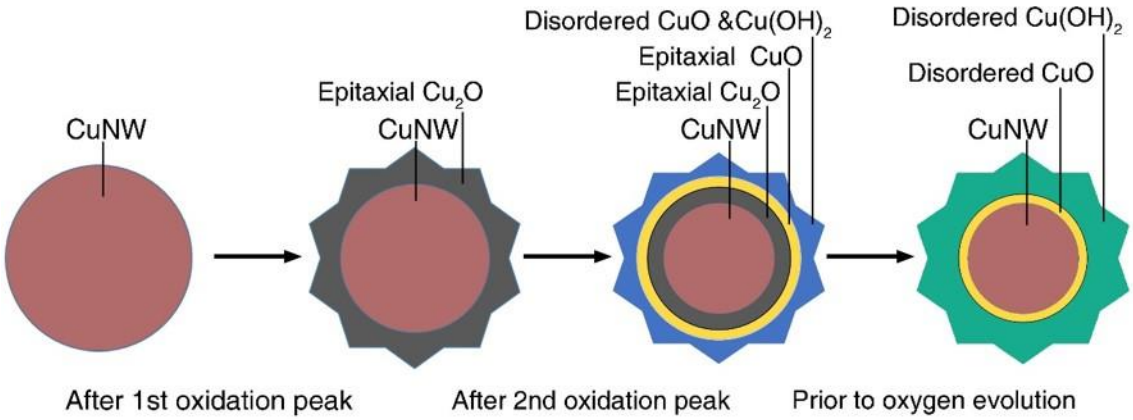

Figure 4.12 Schematic evolution of the oxide films on CuNWs under the different electrochemical potentials in 0.1 M NaOH solution.

On the basis of TEM characterizations, the evolution of oxide films on CuNWs subject to potentiodynamic sweep in 0.1 M NaOH solution can be summarized as the schematic in Figure 4.12. Initially, a homogeneously epitaxial Cu_2O layer is formed on the CuNW substrates achieved by interfacial electrochemical reaction following the SSR mechanism[20]. With the increment of applied potential, a compact CuO layer is developed and sticks to the epitaxial Cu_2O layer with parallel alignment to the inner layer. At the same time, heterogeneous nano-crystals composed of CuO and $Cu(OH)_2$ are also produced at the outmost surface following DR mechanism[9]. When the applied potential arrives the potential prior to oxygen evolution, the homogeneous Cu_2O layer disappears and is

replaced by heterogeneous dual-layer ($CuO/Cu(OH)_2$) structure.

4.4 Conclusions

The electrochemical response of single crystalline CuNWs to 40 % RH atmosphere and 0.1 M NaOH solution has been studied by TEM. With the elongation of exposure duration of CuNWs in 40 % RH atmosphere environment, a uniform Cu_2O film is found to epitaxially grow on the CuNW surfaces following the logarithmic law growth rate, demonstrating their higher growth rate in comparison with the bulky copper. The electrochemical stability test of CuNWs when subject to the cyclic sweep in 0.1 M NaOH aqueous solution, a homogeneously epitaxial Cu_2O layer is initially formed and covers the CuNW substrates at low potentials. The conversion of Cu_2O into CuO occurs at higher polarization potentials whilst the DR process of the partial CuO results in the formation of outer layer of $Cu(OH)_2$ mixed with CuO. The thickness of outer layer will increase at the expense of inner Cu_2O layer due to the increased potential. In addition, no parallel alignment CuO layer adjacent to the CuNW substrate exists prior to the oxygen evolution potential. Instead, a dual-layer ($CuO/Cu(OH)_2$) film is formed on the CuNW surface. The study of the environmental stability of single crystalline CuNWs in the atmospheric air and alkaline aqueous solution is meaningful, and can offer some fundamental references for the environmental stability in the CuNWs-based nanodevices.

References

[1] Aastrup, T.; Wadsak, M.; Leygraf, C.; Schreiner, M., *J. Electrochem. Soc.* **2000**, *147* (7), 2543-2551.

[2] Dou, L.; Cui, F.; Yu, Y.; Khanarian, G.; Eaton, S. W.; Yang, Q.; Resasco, J.; Schildknecht, C.; Schierle-Arndt, K.; Yang, P., *ACS nano* **2016**, *10* (2), 2600-2606.

[3] Chu, H.-C.; Chang, Y.-C.; Lin, Y.; Chang, S.-H.; Chang, W.-C.; Li, G.-A.; Tuan, H.-Y., *ACS Appl. Mater. Interfaces* **2016**, 8(20): 13009-13017.

[4] Zhai, H.; Wang, R.; Wang, W.; Wang, X.; Cheng, Y.; Shi, L.; Liu, Y.; Sun, J., *Nano Res.* **2015**, *8* (10), 3205-3215.

[5] Stortini, A.; Moretto, L.; Mardegan, A.; Ongaro, M.; Ugo, P., *Sens. Actuators, B* **2015**, *207*, 186-192.

[6] Han, D.; Li, X.; Zhao, X.; Feng, J.; Qian, Y., *J. Nanosci. Nanotechnol.* **2015**, *15* (9), 7177-7180.

[7] Jung, S. M.; Preston, D. J.; Jung, H. Y.; Deng, Z.; Wang, E. N.; Kong, J., *Adv. Mater.* **2016**, *28* (7), 1413-1419.

[8] Aastrup, T.; Wadsak, M.; Schreiner, M.; Leygraf, C., *Corros. Sci.* **2000**, *42* (6), 957-967.

[9] FitzGerald, K.; Nairn, J.; Skennerton, G.; Atrens, A., *Corros. Sci.* **2006**, *48* (9), 2480-2509.

[10] Rice, D.; Peterson, P.; Rigby, E. B.; Phipps, P.; Cappell, R.; Tremoureux, R., *J. Electrochem. Soc.* **1981**, *128* (2), 275-284.

[11] Sharma, S., *J. Electrochem. Soc.* **1978**, *125* (12), 2005-2011.

[12] Tran, T. T.; Fiaud, C.; Sutter, E.; Villanova, A., *Corros. Sci.* **2003**, *45* (12), 2787-2802.

[13] Kunze, J.; Maurice, V.; Klein, L. H.; Strehblow, H.-H.; Marcus, P., *Corros. Sci.* **2004**, *46* (1), 245-264.

[14] He, J.-B.; Lu, D.-Y.; Jin, G.-P., *Appl. Surf. Sci.* **2006**, *253* (2), 689-697.

[15] Zhang, B.; Hao, S.; Wu, J.; Li, X.; Huang, Y., *RSC Adv.* **2016**, *6* (24), 19937-19943.

[16] Yu, B.; Woo, P.; Erb, U., *Scripta Mater.* **2007**, *56* (5), 353-356.

[17] Hollmark, H.; Keech, P.; Vegelius, J.; Werme, L.; Duda, L.-C., *Corros. Sci.* **2012**, *54*, 85-89.

[18] Zelinsky, A.; Pirogov, B. Y.; Yurjev, O., *Corros. Sci.* **2004**, *46* (5), 1083-1093.

[19] Bastidas, J.; Cano, E.; Mora, N., *Contraception* **2000**, *61* (6), 395-399.

[20] Chen, B.; Xu, Q.; Zhao, X.; Zhu, X.; Kong, M.; Meng, G., *Adv. Funct. Mater.* **2010**, *20* (21), 3791-3796.

[21] Ambrose, J.; Barradas, R.; Shoesmith, D., *J. Electroanal. Chem. Interfacial Electrochem.* **1973**, *47* (1), 65-80.

Chapter 5

Electrochemical behavior of hierarchical CuNDs

In this chapter, 3D copper foam consisting of hierarchical CuNDs is synthesized by electrodeposition on copper foil. Its electrochemical behaviors in alkaline solution is subsequently studied. It is found that the CuNDs experience a non-equilibrium oxidation process when subject to the cyclic voltammetry (CV) measurement. The SEM, XRD and TEM characterization reveal that the oxidation of the CuNDs is occurred accompanied by the nucleation and growth of $Cu(OH)_2$ nanoneedles during the electrochemical oxidation process.

*This section published/submitted substantially as: Electrochemical behaviors of hierarchical copper nano-dendrites in alkaline media (Nano Research, 2018, 11, 4225).

5.1 Introduction

Copper is one of the most promising metals in multiple applications such as electronic devices, fuel cells and electrocatalysts et al.[1-6] During the past decade, various Cu-based nanomaterials with different structures have been successfully developed as high-efficiency electrocatalysts. In electrocatalytic process, hierarchical structures are regarded as one of the most effective constructions due to the existence of sufficient active sites.[7-9] Nevertheless, the large exposure surface area of Cu-based catalysts with abundant active sites will in turn increase the risk of degradation since they are sensitive to the harsh environments.[10-12] As a consequence, the study on the electrochemical behaviors of the hierarchically structured Cu nanomaterials is significant, especially when they are employed as electrocatalysts.

Electrochemical method is considered as one of the most efficient way to fabricate nanomaterials. Variety of Cu-based nanostructures with uniform or hierarchical structures can be prepared via electrochemical deposition by modulating the parameters of electrochemical methods. Templated from a uniform Cu template, Cu/Cu_2O, $Cu/Cu_2O/CuO$, $Cu/CuO\&Cu(OH)_2$ core/shell structures have been fabricated and successfully applied in O_2 evolution,[13] H_2 production,[14] CO_2 reduction,[15, 16] and lithium ion batteries[17] et al. Furthermore, core-shell $Cu\text{-}CuO_x$ systems with more complicated hierarchical microstructures have been found to be more efficient in the electrochemically driven water splitting.[18-20] However, the fundamental understanding of the electrochemical processes on such core-shell $Cu\text{-}CuO_x$ systems like as-prepared CuNDs is still in lack of direct evidence.

Herein, hierarchical CuNDs with absolutely clean surface were electrodeposited followed by acid washing. To investigate the electrochemical behaviors of as-prepared CuNDs, SEM, TEM and XRD characterizations on the CuNDs were subsequently conducted on the completion of the electrochemical treatments in 0.1 M NaOH aqueous solution.

5.2 Experimental Methods

5.2.1 Electrodeposition of CuNDs

A Cu foil was firstly polished by SiC abrasive paper, followed by rinsing with deionized water and ethanol for several times to thoroughly remove the natural oxide layer on the foil surface. The galvanostatic electrodeposition was carried out in a two-electrode system, where a platinum foil (1.5 cm^2) and Cu foil (1 cm^2) were used as the counter electrode and working electrode, respectively. The porous CuNDs were then fabricated in solution of 0.5 M H_2SO_4 + 0.1 M $CuSO_4$ + 0.2 mM hexadecyltrimethylammonium bromide (CTAB) at a current density of 0.5 A cm^{-2} for 120 s at room temperature. The fabricated CuNDs were immersed in dilute HCl solution for 10 mins to remove the Cu_2O layer that was formed in the electrodeposition process.[19] Prior to electrochemical measurement, the CuNDs were rinsed with deionized water and ethanol before dying in vacuum oven at 60 °C. The schematic of the preparation process of CuNDs is illustrated in Figure. 5.1.

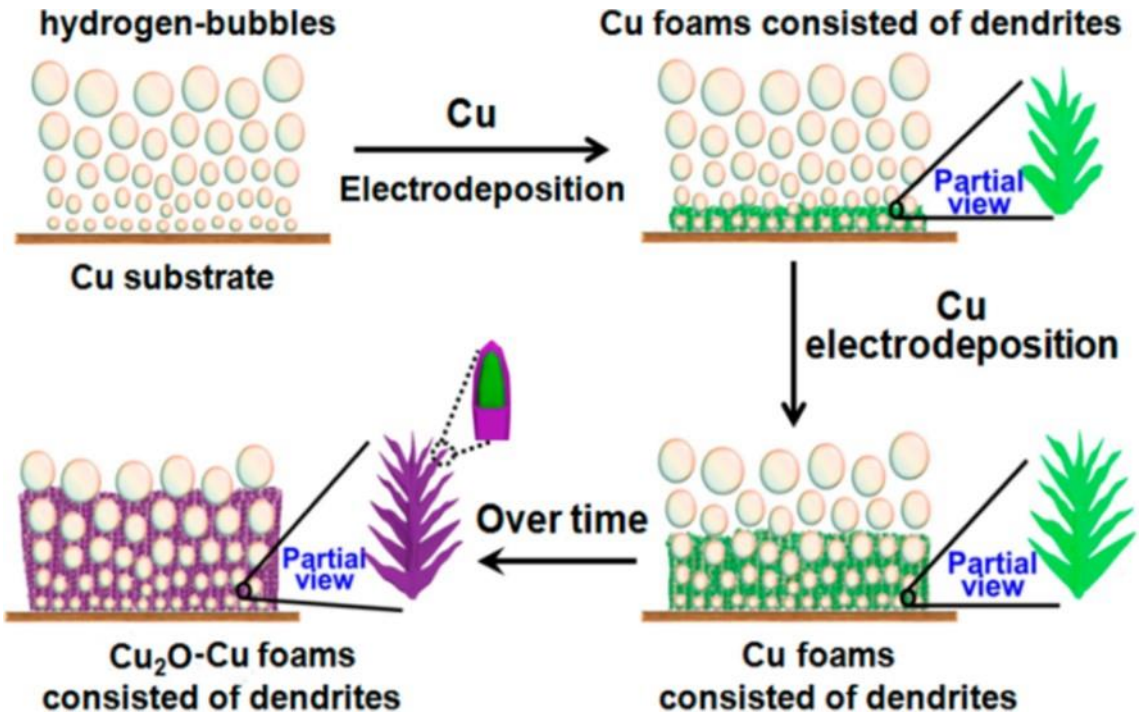

Figure 5.1 Schematic of the fabrication of CuNDs by hydrogen-bubbles assist strategy.[19]

5.2.2 Electrochemical measurement

Cyclic voltammetry measurements were carried out by AUTOLAB PGSTAT 302N (Metrohm Pte Ltd.) at room temperature (25 ± 1 °C) in a typical three-electrode system, in which the CuNDs electrode, a platinum foil and Ag/AgCl electrode with saturated KCl solution were used as working electrode, counter electrode and reference electrode, respectively. The scan rate is 10 mV/s. All the potentials mentioned below are versus the Ag/AgCl reference electrode.

5.2.3 Scanning electron microscopy (SEM)

SEM images were all taken using FESEM (JEOL JSM-7600F, Japan) at SEI mode to reveal the morphologies of the samples. SEM were employed to observe the morphological evolution of the CuNDs after electrochemical polarization in 0.1 M NaOH solution.

5.2.4 Transmission electron microscopy (TEM)

In this part, the role of the TEM is quite similar to that in the first part. JEM 2100F was employed to collect the (HR)TEM images. TEM images were taken to characterize the structural evolution of the CuNDs after being subjected to the electrochemical polarization in 0.1 M NaOH solution. At the same time, the composition of the oxide species that were formed on the CuNDs was also revealed by the combination of HRTEM images and the corresponding FFT patterns generated on them. To ensure the accuracy of the results, TEM characterizations were carried out on more than five CuNDs and nanoneedles for each case.

5.2.5 Powder X-ray diffraction (XRD)

X-ray powder diffractometer (Bruker D8 Advance, Germany) with Cu Kα radiation (λ=1.5406 Å) was employed to characterize the phase information during the evolution of the CuNDs after being subjected to the electrochemical polarization in 0.1 M NaOH solution.

5.3 Principle Outcomes

5.3.1 Electrochemical behavior of CuNDs in 0.1 M NaOH solution

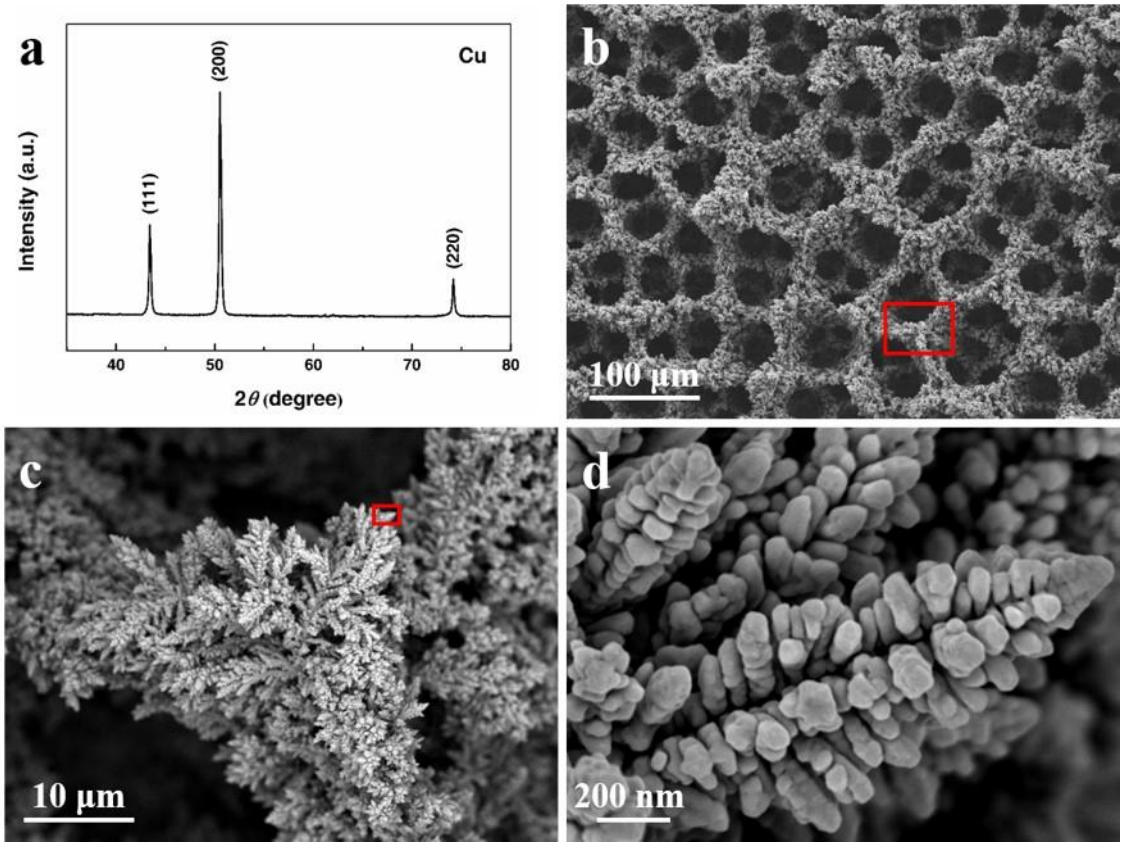

Figure 5.2 (a) XRD pattern of CuNDs after surface cleaning; (b-d) SEM images of CuNDs at different magnifications; (e, f) Low magnification and high resolution TEM images of CuNDs.

After thoroughly cleaning in the dilute HCl solution, CuNDs electrode was verified to be composed of pure metallic Cu by the XRD patterns (Figure 5.2a), where three sharp peaks are visible and correspond to (1 1 1), (2 0 0) and (2 2 0), respectively. Morphology of the as-prepared CuNDs was revealed by SEM at different magnifications. Figure 5.2b shows that the electrodeposited electrode has a uniform porous structure, in which the size of pores is around 20- 80µm. The formation of the porous structure is a result of Cu electrodeposition coupled with hydrogen evolution at a high cathodic current on the Cu foil surface.[21] The walls of the porous structure are viewed at a high magnification to be consisted of a large amount of nano-dendrites (Figure 5.2c).

Further zoomed-in SEM image (Figure 5.2d) along with TEM image (Figure 5.3a) reveals that the CuNDs are orderly assembled by Cu nanoparticles. High-resolution TEM (HRTEM) image (Figure 5.3b) taken from the marked region in Figure 5.3b shows that CuND nanoparticles present a completely clean surface. Furthermore, the fast Fourior transform (FFT) pattern in Figure 1f determines the particle is pure Cu and oriented at a zone axis of [1 0 1].

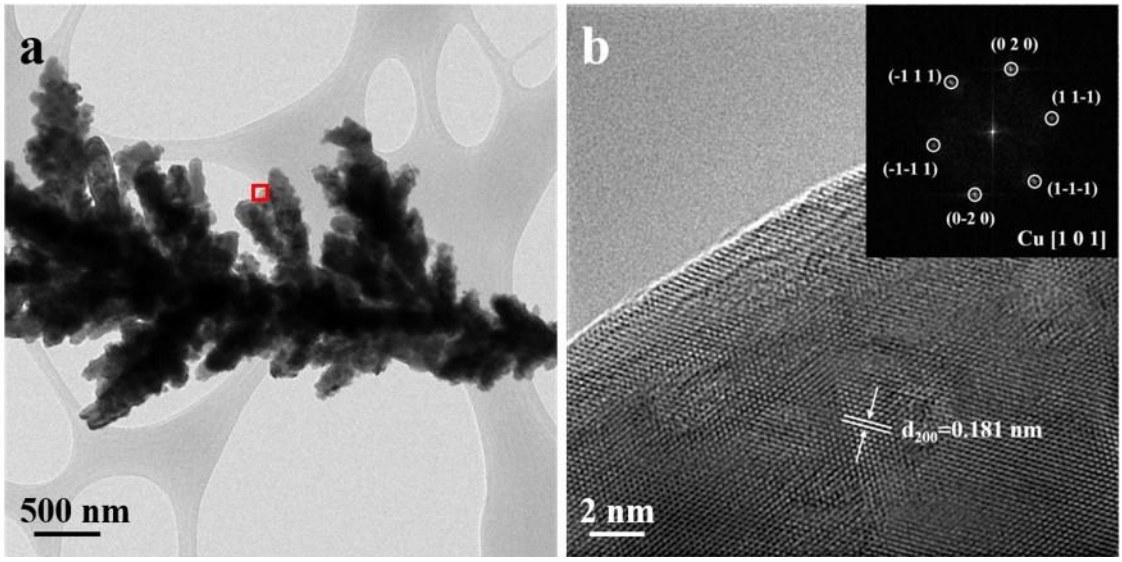

Figure 5.3 (a) Low magnification and (b) high resolution TEM images of CuNDs.

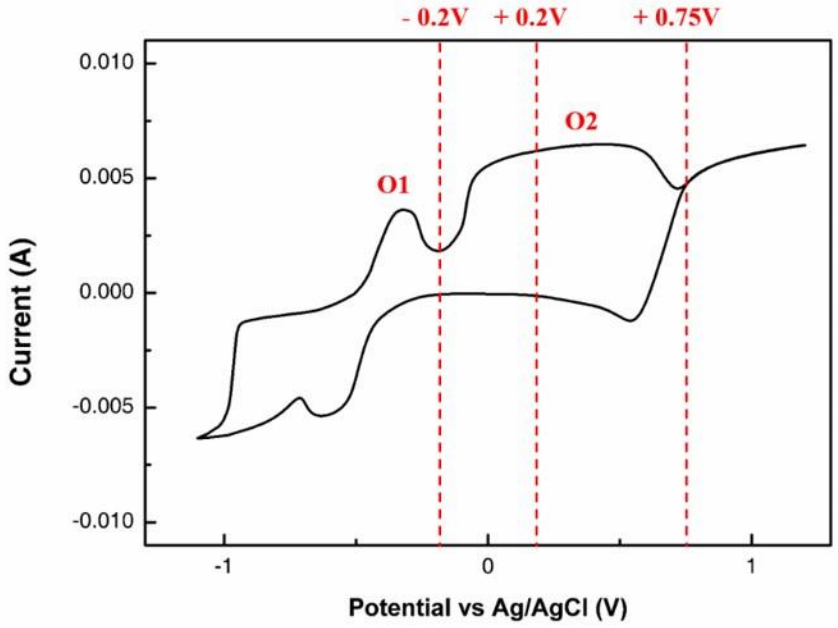

Figure 5.4 A cyclic voltammetry curve of CuNDs electrode in 0.1 M NaOH aqueous solution.

Cyclic voltammetry (CV) measurement was carried out to investigate the electrochemical behaviors of CuNDs in 0.1 M NaOH aqueous solution. The CV profile of hierarchical CuNDs electrode in Figure 5.4 shows two oxidation peaks O1 and O2 in the anodic sweep, which correspond to the formation of Cu(I) and Cu(II) oxide species, respectively. However, compared to the first oxidation peak O1, the second peak O2 turns out to be more like a plateau than a peak, which starts at -0.2 V and ends at + 0.75 V, indicating an complex electrochemical process on CuNDs electrode occurs at this potential range. In order to further clarify the electrochemical behavior of the hierarchical CuNDs electrode in 0.1 M NaOH electrolyte, morphological and structural characterizations have been conducted after the electrodes were anodically polarized to three different potentials (i.e. -0.2 V (behind O1), + 0.2 V (on O2) and + 0.75 V (behind O2)). Prior to the XRD, SEM and TEM characterizations, the polarized CuNDs were immediately washed by deionized water and ethanol before they were dried for a short time in vacuum desiccators.

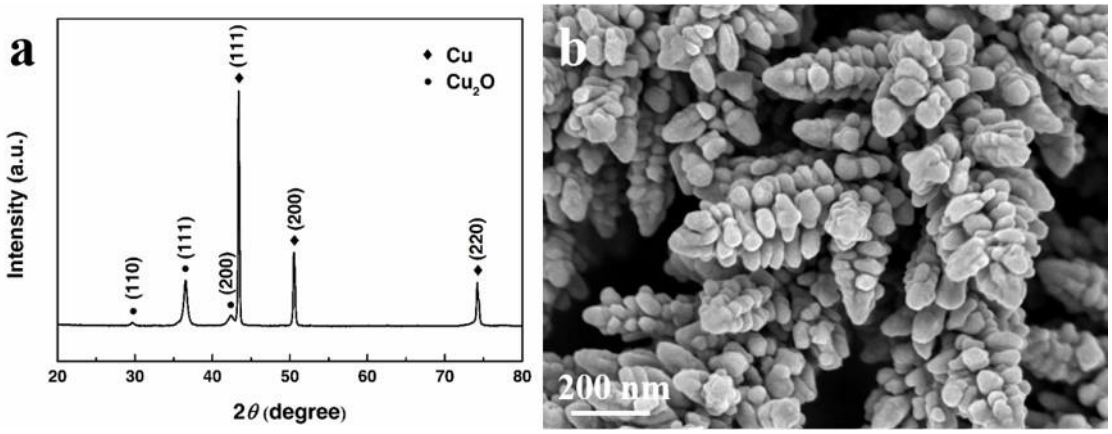

Figure 5.5 (a) XRD pattern, (b) SEM image of CuNDs after being polarized to – 0.2 V.

Figure 5.5a presents the XRD pattern of the CuNDs after subject to electrochemical polarization to – 0.2 V in 0.1 NaOH aqueous solution, which is just beyond the first oxidation peak O1. Except the three strong peaks reflected from Cu, three more peaks are also visible, which are generated from cubic Cu_2O. The result indicates that the first peak O1 in Figure 5.4 is associated with the oxidation of Cu into Cu_2O, which is consistent with the electrochemical process happened on Cu materials with regular structures in the same conditions. According to the SEM image in Figure 5.5b, the surface of the CuNDs remains smooth and no obvious morphological change on CuNDs is observed.

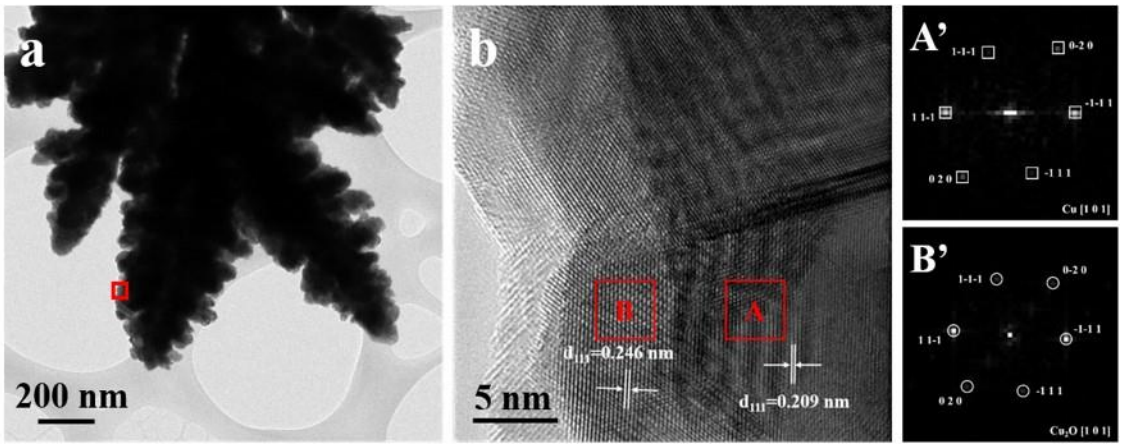

Figure 5.6 (a) Low magnification and (b) high resolution TEM images of CuNDs after being polarized to – 0.2 V. The FFT patterns (A' and B') correspond to the marked areas A and B in panel d.

Figure 5.6b is a magnified HRTEM image that was taken from the marked square on the surface of a copper dendrite in Figure 5.6a. The difference between the Cu substrate and its adjacent oxide layer can be easily distinguished from the phase contrast in the HRTEM image. Furthermore, more compositional and structural information is acquired from the FFT patterns that are derived from square A of Cu matrix and B of the oxide film. By indexing the FFT patterns A' and B', the oxide film is identified to be cubic Cu_2O imaged in the projection plane of [1 0 1], which is epitaxially grown on the cubic Cu substrate along (1 1 1) and (2 0 0) lattice planes. This result is identical to the previous uniform Cu nanowire that we reported[11]. The formation of this Cu_2O layer also follows the solid-state reaction (SSR) mechanism,[11] where the surface Cu atoms are oxidized by OH^- to Cu_2O through the reaction below:

$$2Cu + 2OH^- \rightarrow Cu_2O + H_2O + 2e \quad (1)$$

When the potential is polarized to the second oxidation peak O2 and reaches + 0.2 V, diffraction peaks of the CuNDs are remained the same and are produced from both Cu and Cu_2O (Figure 5.7a). The surface of CuNDs appears slightly rougher and several nanoneedle-like products are grown from the CuNDs (Figure 5.7b). Some nanoneedles with various diameters are also found to attach to the CuNDs, where the thick nanoneedles

are bundled by several thin nanowires with an average diameter of ~ 10 nm.

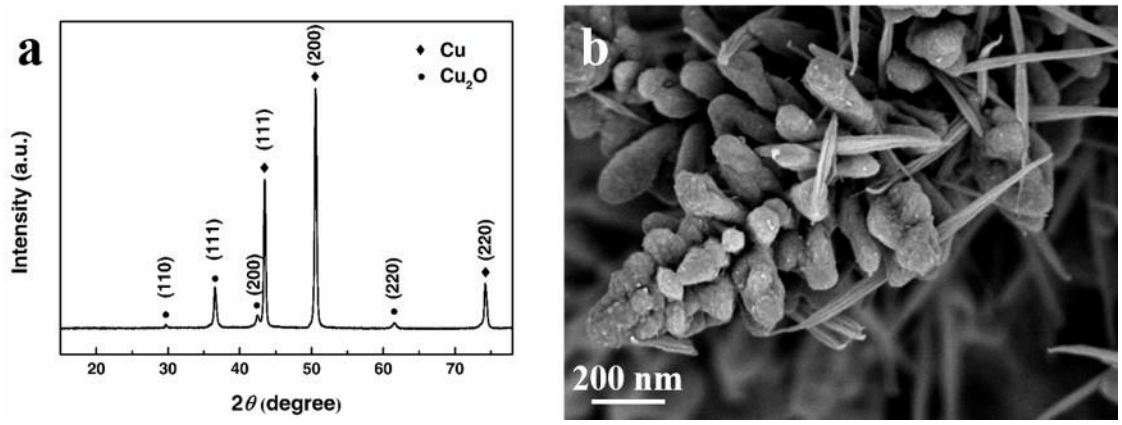

Figure 5.7 (a) XRD pattern, (b) SEM image of CuNDs after being polarized to + 0.2 V.

More detailed examination by TEM with higher resolution reveals that the surface of CuNDs is covered by a non-uniform thin layer (Figure 5.8a). Based on the inset FFT pattern transformed from the marked region at the substrate-oxide layer interface (Figure 5.8b), the thin layer formed on CuNDs is determined to be still Cu_2O, suggesting that no further oxidation reaction has happened on the previously formed epitaxial Cu_2O layer when the applied potential increases to + 0.2 V. Figure 4e is a bright-field TEM image of multiple nanowires that are bundled together along the same direction as a single nanoneedle. These nanowires can be simply differentiated from both mass thickness and phase contrasts (Fig. 5.8c). According to the inset FFT pattern in Figure 5.8d, the nanoneedle is identified to be $Cu(OH)_2$ and grown along [0 2 2] direction. However, due to the small amount of $Cu(OH)_2$ nanoneedles incorporated with the oxidized CuNDs and their low crystallinity, no diffraction of $Cu(OH)_2$ can be resolved by x-rays in Figure 5.7a. The plausible mechanism for the formation of the $Cu(OH)_2$ nanoneedles will be discussed below.

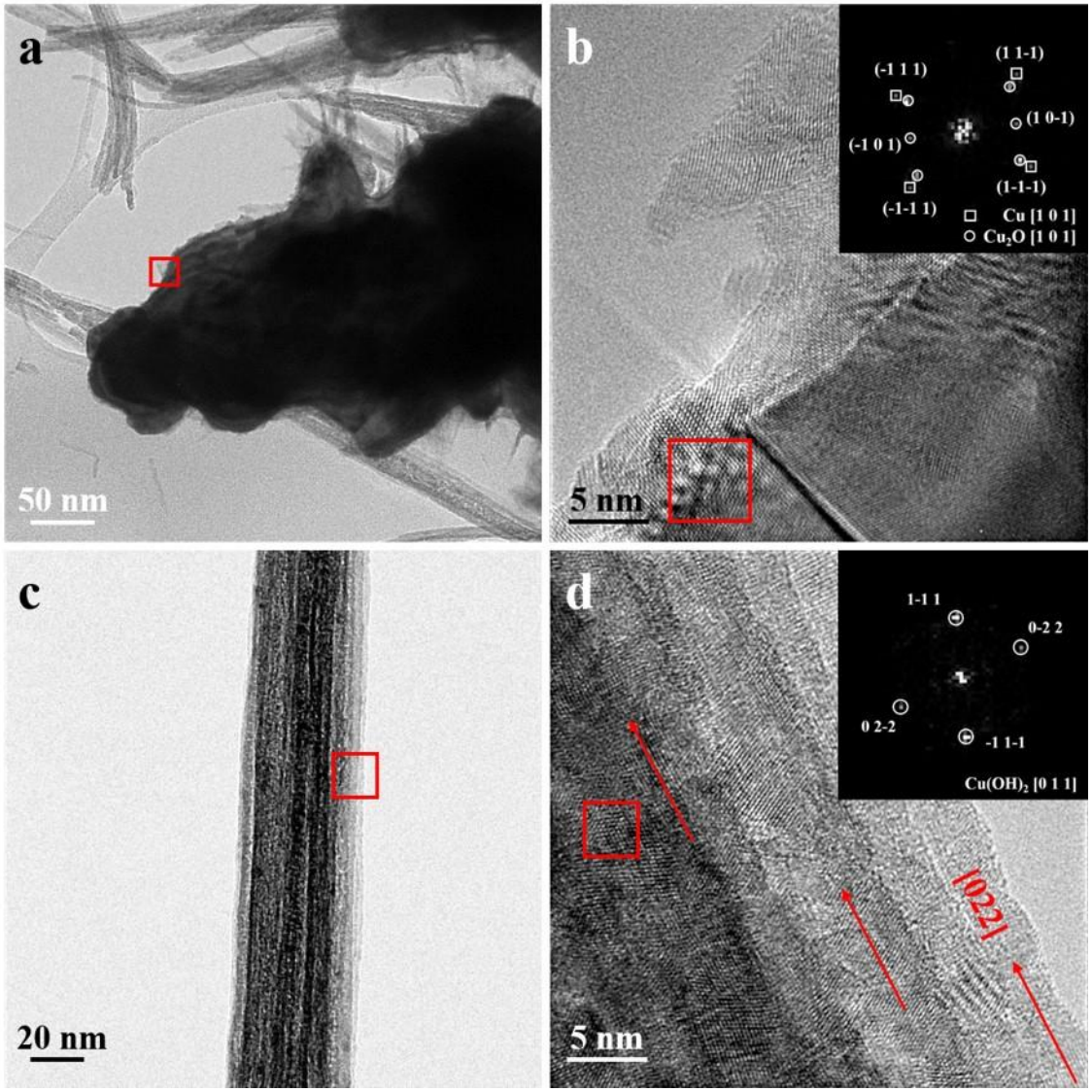

Figure 5.8 (a) Low magnification TEM image of CuNDs after being polarized to + 0.2 V; (b) HRTEM image taken from the marked area in panel a; (c) Low magnification image of a nanoneedle that grown during the electrochemical oxidation process; (d) HRTEM image taken from the marked area in panel c. The FFT patterns in (b) and (d) are transformed from the squares marked in the corresponding image, respectively.

With the further increase of applied potential, the broad second oxidation peak O2 terminates at + 0.75 V. The XRD pattern of the CuNDs presents additional peaks that are contributed from CuO and $Cu(OH)_2$. Due to the adherence of nanoflakes, the surface of the CuNDs appears much rougher and more number of $Cu(OH)_2$ nanoneedles are seen and decorated on the CuNDs (Fig.5.9b).

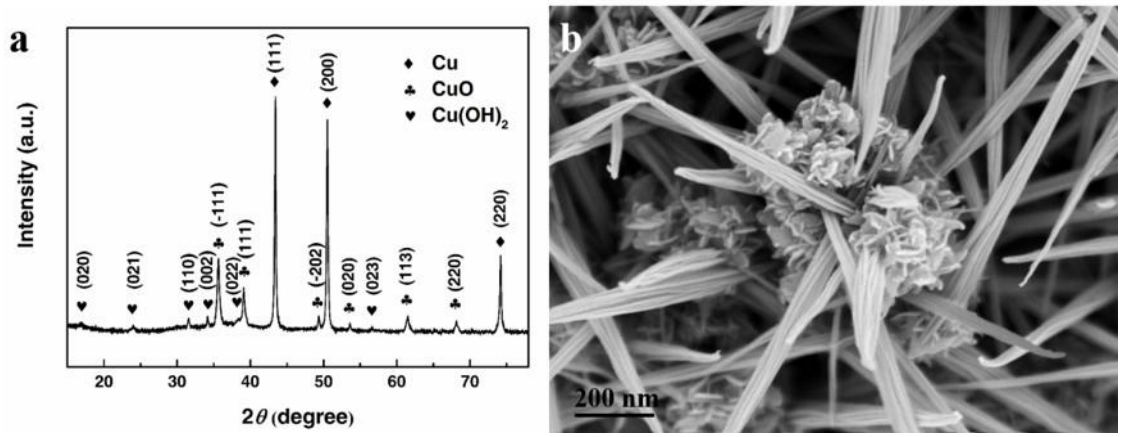

Figure 5.9 (a) XRD pattern, (b) SEM image of CuNDs after being polarized to + 0.75 V.

Figure 5.10a is a low magnification TEM image of the tip area of a CuND (as shown in the inset) after oxidation. Three regions A, B and C represented nanoflakes, inner interface and outer interface are selected in order to analyze their respective compositions. Nanoflakes are determined to be $Cu(OH)_2$ through indexing the FFT pattern (inset) that is transformed from square D in Figure 5.10b, where the d-spacing 0.249 nm corresponds to the lattice plane (1 1 1) of $Cu(OH)_2$. The overlap of nanoflakes gives rise to a lot of moire fringes (Figure 5.10b). Figure 5.10c shows a HRTEM image taken from the inner interface between the Cu substrate and the inner oxide layer. The corresponding FFT patterns E' and F' generated from square marked regions of E and F are reflected from CuO and Cu. This analysis illustrates that high potential allows the full conversion of Cu_2O into CuO which then forms the inner layer adjacent to the Cu matrix as proved by the XRD result in Figure 5.9a. Random orientation between the Cu substrate and CuO layer suggests that the formation of the inner CuO follows dissolution-redeposition (DR) mechanism.[11] Meanwhile, polycrystalline $Cu(OH)_2$ layer at the outmost layer is seen to cover the CuO inner layer (Figure 5.10d), as confirmed by the corresponding FFT patterns as well as the lattice d-spacings. Based on the results above, the oxide film formed on CuNDs after they are polarized to + 0.75 V is found to have a double-layer structure (i.e. CuO inner layer and non-uniform nanoflake-like $Cu(OH)_2$ layer). Besides, more $Cu(OH)_2$ nanoneedles are simultaneously grown on CuNDs when higher applied potential is applied.

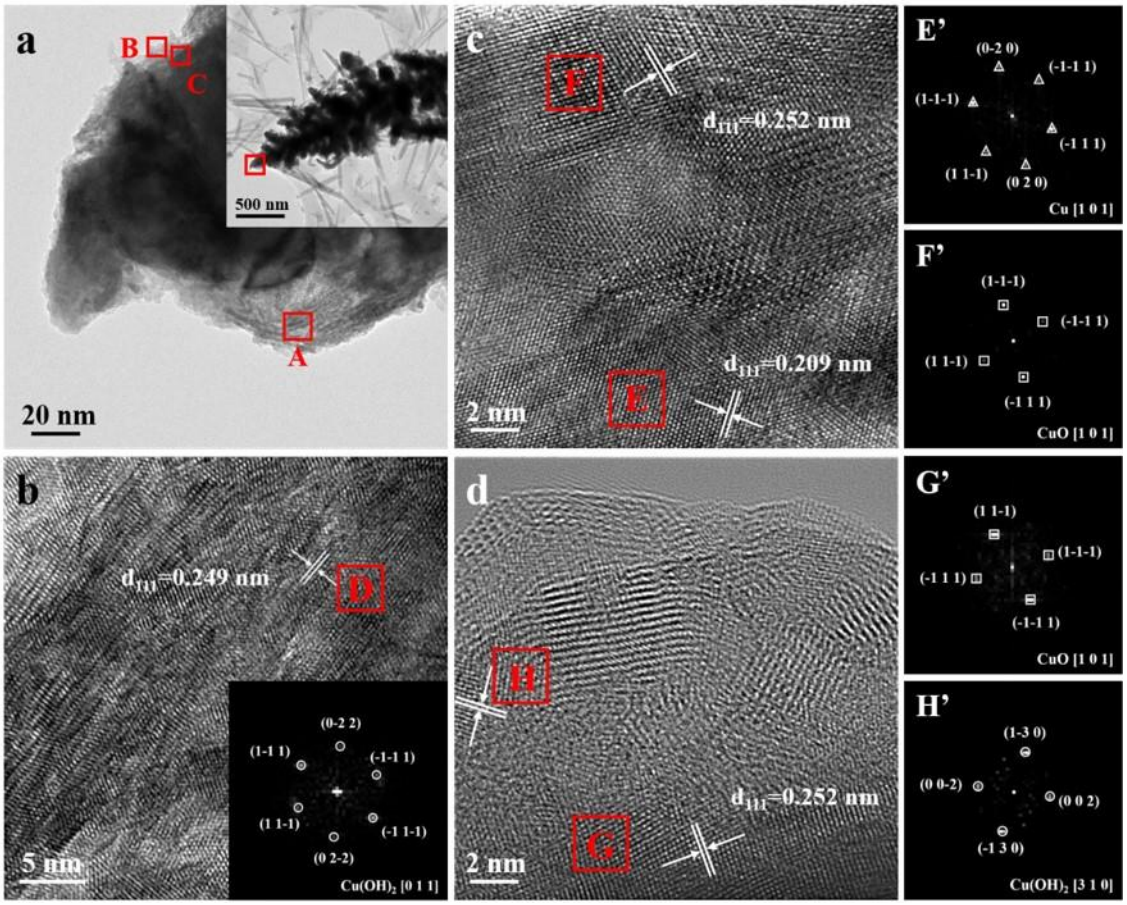

Figure 5.10 (a) Low magnification TEM images of CuNDs after being polarized to + 0.75 V; (b-d) HRTEM images taken from the marked area A,B and C in panel a, respectively. The inset FFT patterns in panel b is transformed from the square marked in the corresponding image. The FFT patterns E', F', G' and H' are derived from the squares E, F, G and H, respectively.

On the basis of XRD, SEM and TEM characterizations, the oxidation process on CuNDs subject to electrochemical scan in 0.1 M NaOH aqueous solution can be schematically illustrated in Figure 5.11. After the first oxidation peak O1, an epitaxial Cu_2O layer is first formed on the surface of CuNDs ascribed to the direct oxidation of OH^- following the SSR mechanism. Since the CuNDs are electrochemically constructed with numerous Cu nanoparticles, the Cu_2O layer that is formed at the boundaries between particles must be less compact and stable than that grown on the surface of individual particles. Thus, the vulnerable Cu_2O layer at the boundaries will become much more active when the applied potential is increased. With the more anodic sweep, the active boundary Cu_2O layer is preferentially destroyed, which will accelerate the dissolution of Cu into Cu^{2+}. As a

consequence, the abundant Cu^{2+} at boundary regions tend to react with the OH^- in the solution, leading to the locally nucleation and growth of $Cu(OH)_2$ through the following reaction:[22-24]

$$Cu^{2+} + 2OH^- \rightarrow Cu(OH)_2 \quad (2)$$

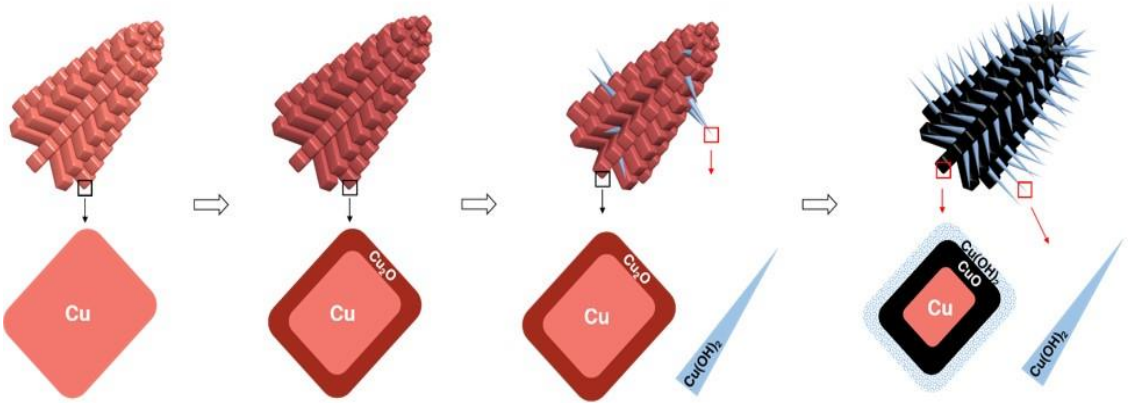

Figure 5.11 The oxidation process on CuNWs with the increase of electrochemical potential in 0.1 M NaOH aqueous solution.

Meanwhile, the priority of the reaction above allows the compact Cu_2O layer on the Cu particles free from the OH^- attack when the external potential is sufficient low. However, the increase of anodic potential will supply more energy that activates the Cu_2O layer and drives the reaction between Cu_2O and OH^-. When the potential reaches + 0.75 V, a sufficient high value, the compact Cu_2O layer will be completely consumed and transformed into CuO and $Cu(OH)_2$. Finally, a dual-layer (i.e. inner CuO layer /outer $Cu(OH)_2$ layer) structure is formed on the CuNDs surface.[11] In the meantime, more $Cu(OH)_2$ nanoneedles nucleate and grow from the localized regions of CuNDs.

5.3.2 OER Electrocatalysis Evaluation of bare CuNDs

Based on the understanding of the electrochemical evolution mechanism of the bare CuNDs in alkaline solution. The activity of the as-polarized CuNDs electrode for oxygen evolution reaction was subsequently performed. As shown in Figure 5.12a and b, the

untreated Cu_2O-Cu NDs requires a much higher overpotential (~ 400 mV) to reach a current density of 10 mA^{-2} and shows a considerably larger Tafel slope (> 200 mV dec^{-1}) compared to the the Cu_2O based electrocatalysts in the previous studies,[25, 26] indicating its poor essence as an OER catalyst. The low OER performance of the Cu_2O-Cu NDs is probably inhibited by these nanoneedles with low water oxidation activity. Therefore, surface modification on the CuNDs is essentially required to improve the performance of CuNDs-based electrocatalysts.

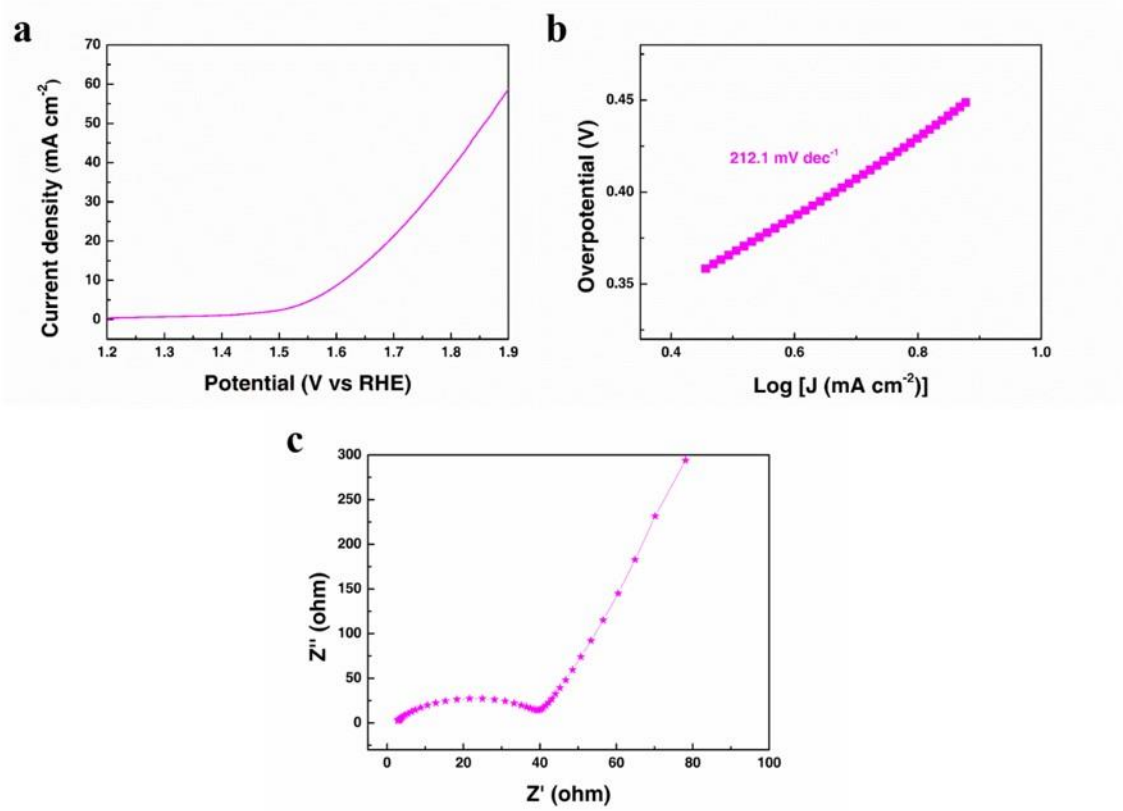

Figure 5.12 (a) LSV curves of polarized CuNDs electrode in 1.0 M KOH solution at a scan rate of 5 mV s^{-1}; Tafel plots (b) and Nyquist plots (c) of the NDs electrode.

5.4 Conclusions

The electrochemical behaviors of hierarchical CuNDs when subject to 0.1 M NaOH aqueous solution are studied by CV in combination with XRD, SEM and TEM. In the first stage, an epitaxially thin layer of Cu_2O is initially formed on the CuNDs surface after the first oxidation peak. $Cu(OH)_2$ nanoneedles then start to nucleate and grow from CuNDs

and oxidation of Cu_2O subsequently occurs. With the increase of potential, Cu_2O is completely transformed into CuO and $Cu(OH)_2$ forming a dual-layer structure whilst $Cu(OH)_2$ nanoneedles sustain the rapid growth. In the electrochemical water splitting experiment, the catalytic activity of as-polarized CuNDs electrode for OER was quite poor due to the surface degradation during the electrochemical oxidation process.

References

[1] Du, J.; Chen, Z.; Ye, S.; Wiley, B. J.; Meyer, T. J., *Angew. Chem. Int. Ed.* **2015,** *54* (7), 2073-2078.

[2] Chen, Z.; Meyer, T. J., *Angew. Chem.* **2013,** *125* (2), 728-731.

[3] Coggins, M. K.; Zhang, M. T.; Chen, Z.; Song, N.; Meyer, T. J., *Angew. Chem. Int. Ed.* **2014,** *53* (45), 12226-12230.

[4] Liu, X.; Sui, Y.; Yang, X.; Wei, Y.; Zou, B., *ACS Appl. Mater. Interfaces* **2016,** *8* (40), 26886-26894.

[5] Periasamy, A. P.; Liu, J.; Lin, H.-M.; Chang, H.-T., *J. Mater. Chem. A* **2013,** *1* (19), 5973-5981.

[6] Heli, H.; Jafarian, M.; Mahjani, M.; Gobal, F., *Electrochim. Acta* **2004,** *49* (27), 4999-5006.

[7] Xia, L.-P.; Guo, P.; Wang, Y.; Ding, S.-Q.; He, J.-B., *J. Power Sources* **2014,** *262*, 232-238.

[8] Gawande, M. B.; Goswami, A.; Felpin, F.-X.; Asefa, T.; Huang, X.; Silva, R.; Zou, X.; Zboril, R.; Varma, R. S., *Chem. Rev* **2016,** *116* (6), 3722-3811.

[9] Jia, X.; Yang, X.; Li, J.; Li, D.; Wang, E., *Chem. Commun.* **2014,** *50* (2), 237-239.

[10] Wu, J.; Li, X.; Yadian, B.; Liu, H.; Chun, S.; Zhang, B.; Zhou, K.; Gan, C. L.; Huang, Y., *Electrochem. Commun.* **2013,** *26*, 21-24.

[11] Zhang, B.; Chen, B.; Wu, J.; Hao, S.; Yang, G.; Cao, X.; Jing, L.; Zhu, M.; Tsang, S. H.; Teo, E. H. T., *Small* **2017,** *13* (10).

[12] Zhang, B.; Hao, S.; Wu, J.; Li, X.; Huang, Y., *RSC Adv.* **2016,** *6* (24), 19937-19943.

[13] Cheng, N.; Xue, Y.; Liu, Q.; Tian, J.; Zhang, L.; Asiri, A. M.; Sun, X., *Electrochim. Acta* **2015,** *163*, 102-106.

[14] Zhang, S.; Ma, Y.; Zhang, H.; Zhou, X.; Chen, X.; Qu, Y., *Angew. Chem. Int. Ed.* **2017,** *56* (28), 8245-8249.

[15] Huan, T. N.; Simon, P.; Benayad, A.; Guetaz, L.; Artero, V.; Fontecave, M., *Chem. Eur. J.* **2016,** *22* (39), 14029-14035.

[16] Brito, J. F. d.; Silva, A. A. d.; Cavalheiro, A. J.; Zanoni, M. V. B., *Int. J. Electrochem. Sci.* **2014**, 5961-5973.

[17] Zhao, Y.; Zhang, Y.; Zhao, H.; Li, X.; Li, Y.; Wen, L.; Yan, Z.; Huo, Z., *Nano Res.* **2017**, 1-3.

[18] Dubale, A. A.; Pan, C.-J.; Tamirat, A. G.; Chen, H.-M.; Su, W.-N.; Chen, C.-H.; Rick, J.; Ayele, D. W.; Aragaw, B. A.; Lee, J.-F., *J. Mater. Chem. A* **2015,** *3* (23), 12482-12499.

[19] Xu, H.; Feng, J.-X.; Tong, Y.-X.; Li, G.-R., *ACS Catal.* **2016,** *7* (2), 986-991.

[20] Huan, T. N.; Rousse, G.; Zanna, S.; Lucas, I. T.; Xu, X.; Menguy, N.; Mougel, V.; Fontecave, M., *Angew. Chem.* **2017,** *129* (17), 4870-4874.

[21] Shin, H.-C.; Liu, M., *Chem. Mater.* **2004,** *16* (25), 5460-5464.

[22] Wu, X.; Bai, H.; Zhang, J.; Chen, F. e.; Shi, G., *J. Phys. Chem. B* **2005,** *109* (48), 22836-22842.

[23] Zhang, W.; Wen, X.; Yang, S.; Berta, Y.; Wang, Z. L., *Adv. Mater.* **2003,** *15* (10), 822-825.

[24] La, D.-D.; Park, S.-Y.; Choi, Y.-W.; Kim, Y.-S., *Bull. Korean Chem. Soc.* **2010,** *31* (8), 2283-2288.

[25] Hou, C. C.; Fu, W. F.; Chen, Y., *ChemSusChem* **2016,** *9* (16), 2069-2073.

[26] Deng, Y.; Handoko, A. D.; Du, Y.; Xi, S.; Yeo, B. S., *ACS Catal.* **2016,** *6* (4), 2473-2481

Chapter 6

Hollow shell coated hierarchical CuNDs for OER catalysis

In this chapter, 3D copper foam consisting of hierarchical CuNDs is initially synthesized by electrodeposition. A thin layer of Cu-MOFs is subsequently in-situ grown on the surface of the as-prepared CuNDs and transformed into a nanostructured CuO/C hollow shell via heat treatment. This electrode is claimed to provide an extraordinary electrocatalysis for oxygen evolution reaction (OER) in alkaline media due to its fast electronic transmission networks, rich redox sites, porous structure and robust architecture.

*This section submitted to ACS Applied Materials & Interfaces.

6.1 Introduction

Electrochemical water splitting has been widely recognized as one of the most promising routes for the generation of sustainable energies with high efficiency.[1-3] In particular, the water oxidation, also known as oxygen evolution reaction (OER), plays a crucial role since its slow kinetics nature limits the whole decomposition process of water.[4-6] To boost the overall efficiency of water splitting, various metal-oxide electrocatalysts based on non-noble transition metals (Ni, Co, Mn, Cu) have been developed with efficient performance.[7-13] Nevertheless, individual metal oxides can hardly realize fast electron transportation and OER kinetics on account of their intrinsic low electrical conductivity. In this regard, extensive efforts have been devoted to improve the electrical conductivity of the metal oxide catalysts, where the incorporation of highly conductive materials (graphene, carbon and conducting polymer et al) to form a hybrid electrocatalysts[14-17] and the employment of conductive substrates (metal foil, metal foam et al)[18-21] are proved to be feasible in promoting the rates of charge transfer and catalytic reactions. However, it is widely agreed that the catalytic efficiency is not only determined by the intrinsic activity and electrical conductivity of the catalysts, but also proportional to their surface area and active-site density.[22-24] On the basis of this consensus, nanostructure engineering has been deemed as another significant research interest in catalyst development although it remains challenging. Over the past decade, rational design and fabrication of hollow structures from metal-organic frameworks (MOFs) templates has been demonstrated as a practical approach to efficient energy storage and conversion applications.[25-31] Beneficial from the internal void space and high surface-to-volume ratio, open channels with large surface area are able to access sufficient active sites for surface catalytic reactions. In addition, the inner void is capable of buffering the structural strain caused by ion transportation and electrochemical reactions so that a robust framework could be maintained for a long-term catalysis. Thus, the fabrication of a hierarchical system constituted of hollow structures on a conductive substrate is desirable to ameliorate the performance of transition metal oxide electrocatalysts.

In terms of Cu-based electrocatalytic system, utilizing metallic Cu as a highly conductive

support has been demonstrated to be an efficient way to improve the catalytic activity of Cu-oxide complexes (Cu_2O, CuO, $Cu(OH)_2$ et al).[18, 19, 32-35] Due to low-resistance substrate, fast charge-transfer rate could be readily reached between the substrate and active materials. The effort in the optimization of Cu-based morphological structure with a high surface area and sufficient active sites can then be made to lower the overpotential for water splitting.

Herein, we report a three-step approach to fabricate a hollow shell coated 3D copper oxide nano-dendrites (NDs) as an extraordinary catalyst for water oxidation. Specifically, a 3D porous template that consists of Cu/Cu_2O core-shell NDs was firstly constructed via electrodeposition.[36] In-situ growth of a thin Cu-MOFs (metal-organic frameworks) layer on top of Cu/Cu_2O NDs was subsequently conducted, followed by precisely controlled heat treatment to form a nanostructured CuO/C hollow shell on the surface, where sufficient active sites were created (Figure 6.1). The incorporation of carbon within the hollow shell contributes to an enhanced conductivity among active CuO nanomaterials as well as a stable structure without collapse. In addition, the formation of an inner passive film further enhances its stability in alkaline solution. Thus, it is not strange that this ideal hierarchical Cu-based system presents extraordinary electrocatalytic activity and durability for oxygen evolution.

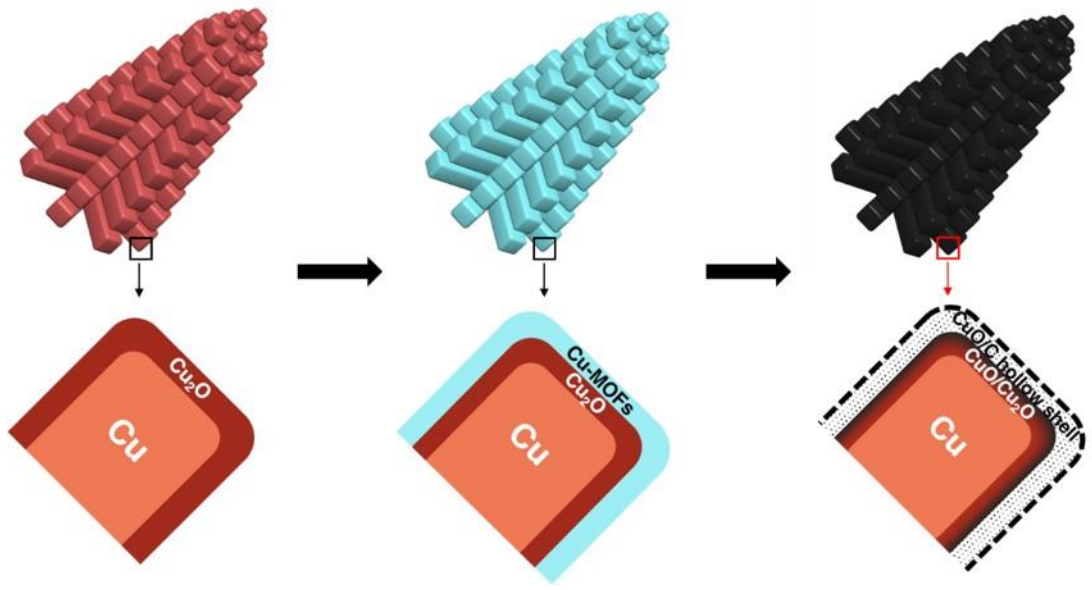

Figure 6.1 Schematic of the fabrication of HS-CuO/C NDs.

6.2 Experimental Methods

6.2.1 Electrodeposition of CuNDs

The electrodeposition method is exactly the same as that in **5.2.1.**

6.2.2 Synthesis of MOFs coated NDs

HKUST-1 MOFs was coated on the NDs by solvent-thermal method. The as-deposited NDs was dried and transferred into a glass bottle with 8 mg Trimesic acid (BTC) dissolved 20 mL benzyl alcohol.[37] Subsequently, the glass bottle was placed in the oven at a constant temperature of 60 ℃ for 12 hours. The as-obtained 3D foam was rinsed with ethanol and deionized water for several time and dried in the oven.

6.2.3 Synthesis of HS-CuO/C NDs and PS-CuO/C NDs and PS-CuO NDs

HS-CuO/C NDs was obtained by a two-step heat treatment approach: MOFs coated NDs was annealed at 350℃ for 30 mins under Ar flow followed by a calcination at 250 ℃ under air flow for 2 hours. PS-CuO/C NDs was prepared by calcinating the MOFs coated NDs at 350℃ for 2 hours under Ar flow then annealed at 250 ℃ under air flow for 1 hour. PS-CuO NDs was fabricated by a direct heat treatment on the MOFs coated NDs at 350 ℃ for 2 hours under air flow.

6.2.4 Scanning electron microscopy (SEM)

SEM images were all taken using FESEM (JEOL JSM-7600F, Japan) at SEI mode to reveal the morphologies of the samples. SEM observation were also employed to characterize the overall morphologies of the Cu-based NDs. First, the as-prepared CuNDs were found to be composed of a large amount of nanoparticles. The overall and detailed morphologies of the MOFs coating and their derived hollow shell and porous shell on the CuNDs were also characterized under SEM. Furthermore, the surface condition of the HS-CuO/C NDs after

long term electrolysis was also revealed by SEM observation.

6.2.5 Transmission electron microscopy (TEM)

JEM 2100F was employed to collect the (HR)TEM images in order to characterize the structure of the Cu-based NDs. First, the as-prepared CuNDs were found to be covered with a thin layer of Cu_2O by HRTEM observation. The MOFs coating and their derived hollow shell and porous shell were also characterized under TEM, including the thickness and overall structures. Furthermore, the main phase of the hollow shell and porous shell were also reveal by means of HRTEM images.

6.2.6 Powder X-ray diffraction (XRD)

X-ray powder diffractometer (Bruker D8 Advance, Germany) with Cu Kα radiation (λ=1.5406 Å) was employed to characterize the structure of the Cu-based NDs. First, the as-prepared CuNDs were found to be covered with a thin layer of Cu_2O by XRD characterization. The CuNDs with MOFs coating and their derived hollow shell and porous shell were also characterized under XRD. Furthermore, the overall phases of the Cu-based NDs were also reveal by means of XRD patterns.

6.2.7 X-ray photoelectron spectroscopy (XPS)

XPS (Omicron analyzer EA 125) was used to analyze the surface element electron states of elements Cu, O and C in sample HS-CuO/C NDs.

6.2.8 Raman spectroscopy

Raman spectroscopy has been intensively applied to investigate the nature of various carbon-based materials. In the current thesis, Raman spectra (Renishaw) were obtained with an excitation laser wavelength of 532 nm to study the states of carbon that is incorporated with the CuO nanoparticles in the hollow shell coated CuNDs.

6.2.9 Electrochemical measurement of Cu-based NDs catalysts for OER

All electrochemical measurements were performed by Autolab PGSTAT30 Electrochemical Workstation with a three-electrode cell system at room temperature (25 ℃), where the NDs electrode, a platinum foil, an Ag/AgCl (sat. KCl) electrode were used as the working, counter and reference electrode, respectively. All the potentials were recorded with respect to the reversible hydrogen electrode (RHE) by converting the measured potentials vs. Ag/AgCl (sat. KCl) electrode based on the equation below:

$$E\,(RHE) = E\,(Ag/AgCl) + 0.197 + 0.059 * pH \quad (1)$$

The double-layer capacitance (C_{dl}) was measured to estimate the electrochemically-active surface area (ECSA) of HS-CuO/C NDs and HS-CuO/C NDs electrodes by cyclic voltammetry (CV) in 1.0 M KOH. The cyclic voltammograms were measured in a non-Faradaic region (1.185~ 1.315 V vs. RHE) at the scan rates of 1, 2, 5, 10, 15 and 20 mV s^{-1}. The double-layer capacitance of NDs electrocatalyst is taken as the value of slope of the linear fits, which is proportional to the ECSA of electrocatalyst.[7]

6.3 Principle Outcomes

6.3.1 Characterization of CuNDs-based Materials

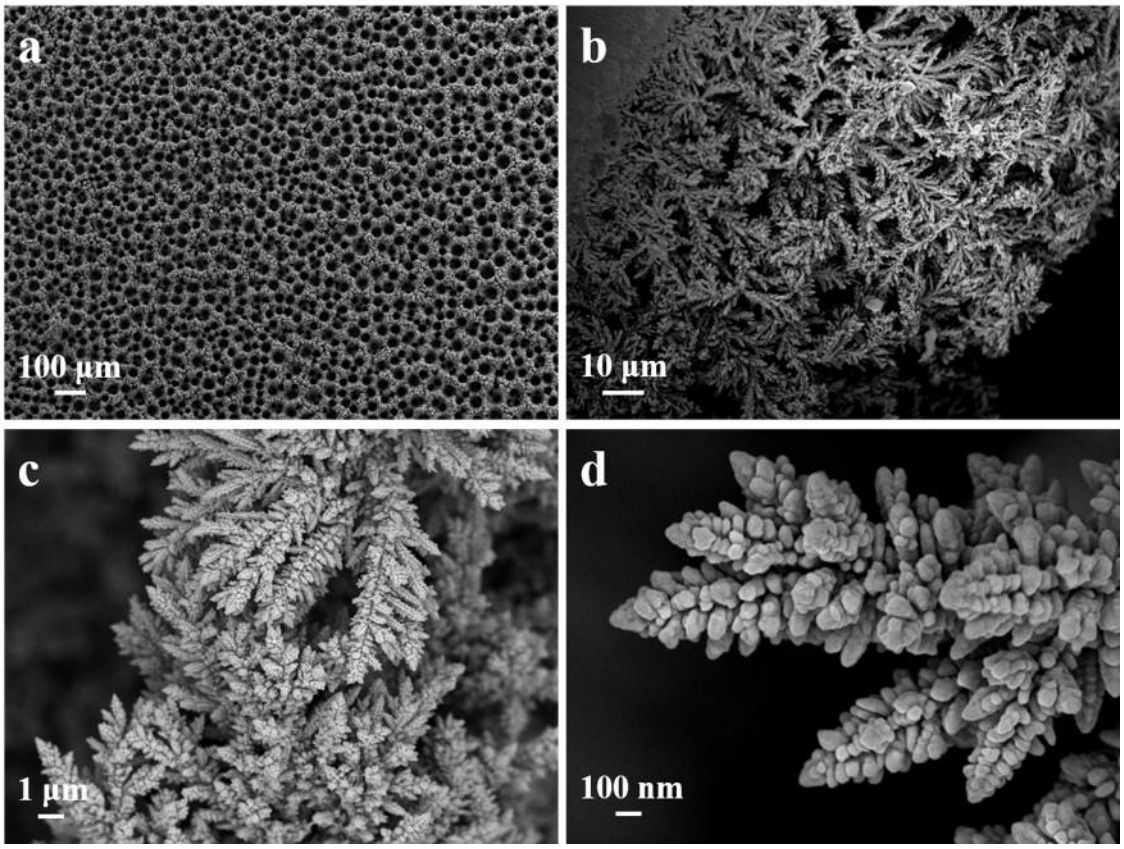

Figure 6.2 (a) Top view, (b) side view and (c) low magnification and (d) high magnification SEM images of as-prepared Cu_2O-Cu NDs.

A 3D copper foam with uniform porous structure covered a copper foil as shown in the top-view SEM image (Figure 6.2a) is coated by hydrogen-bubble templated electrodeposition[38], The pores are macro and have a size of ~ 20- 80 µm. The thickness of the 3D Cu foam is around 100 µm as measured in the cross-sectional SEM image (Figure 6.2b). The zoomed-in SEM image (Figure 6.2c) reveals that the walls of the Cu foam are clustered with abundant nano-dendrites. These NDs are further viewed at a higher magnification in respective SEM and TEM and are seen to be regularly stacked with Cu nanoparticles (Figure 6.2d, Figure 6.3a).

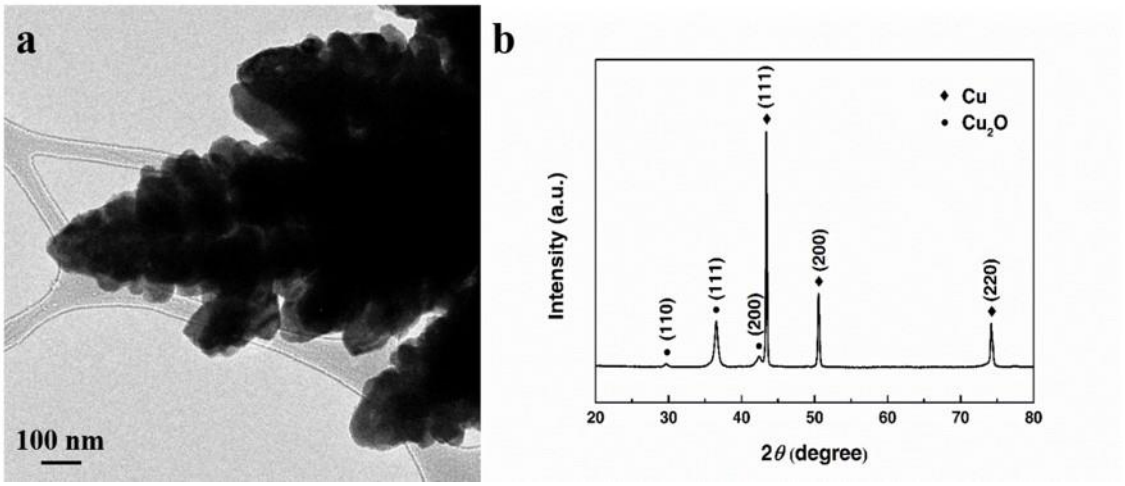

Figure 6.3 TEM image (a) and XRD pattern (b) of as prepared Cu_2O-Cu NDs.

Apparently, such a copper-based hierarchical architecture composed of sufficient macro/micro pores and nano-dendrites is an ideal catalyst candidate since it provides both a high surface area but also and the high-speed transportation of electrocatalysis-involving species. X-ray diffraction (XRD) patterns of the copper foam illustrate the presence of both Cu and Cu_2O (Figure 6.3b). The three relatively weak peaks at lower degrees correspond to cubic Cu_2O, which is formed on the surface of Cu NDs during the electrodeposition process in the oxidizing electrolyte.[38]

Taking advantage of the intrinsically high-activity of Cu_2O, in-situ growth of a Cu-MOFs thin layer on top of Cu/Cu_2O NDs is achieved via a solvothermal approach.[38, 39] SEM image in Figure 6.4a clearly shows that the MOFs coating over NDs is fairly uniform without destroying the dendritic structure and overall porosity of the original templates. The compact adherence of a MOFs thin layer (~ 50 nm) on the surface of NDs is further confirmed by the bright-field TEM image (Figure 6.4c), which can be easily distinguished based on their mass-thickness contrast. XRD analysis reveals that the core/shell NDs are composed of HKUST-1, Cu_2O and Cu. The existence of Cu_2O peaks suggests its incomplete transformation into Cu-MOFs, which can also be reflected by the several weaker peaks corresponding to HKUST-1 (Figure 6.4b).

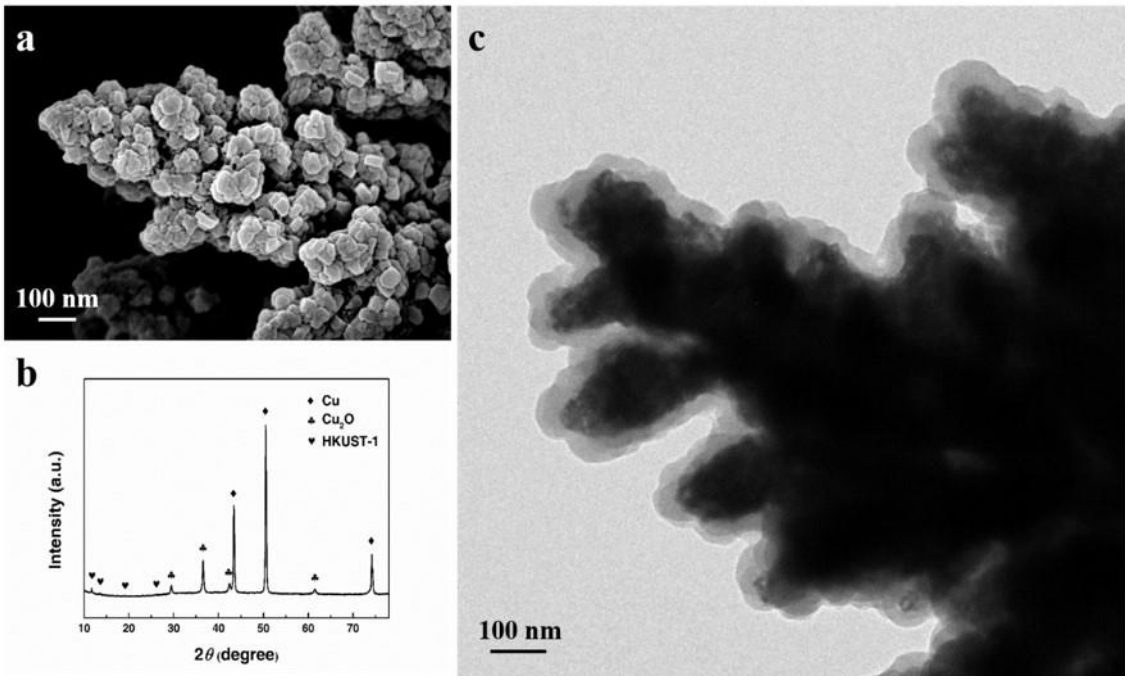

Figure 6.4 SEM image (a), XRD pattern (b) and TEM image (c) of as prepared MOFs coated NDs.

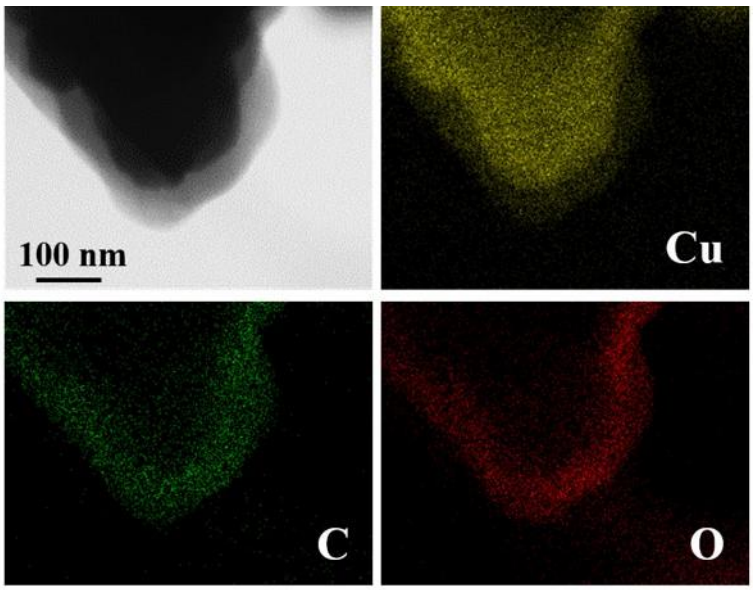

Figure 6.5 STEM image (a) and EDX mapping images (b-d) of MOFs coated NDs.

The ideal MOFs-coating precursor, where the elements Cu, C and O are homogeneously distributed (Figure 6.5) is subsequently transformed into a uniform CuO/C hollow shell surrounding NDs when subjected to a two-step annealing.

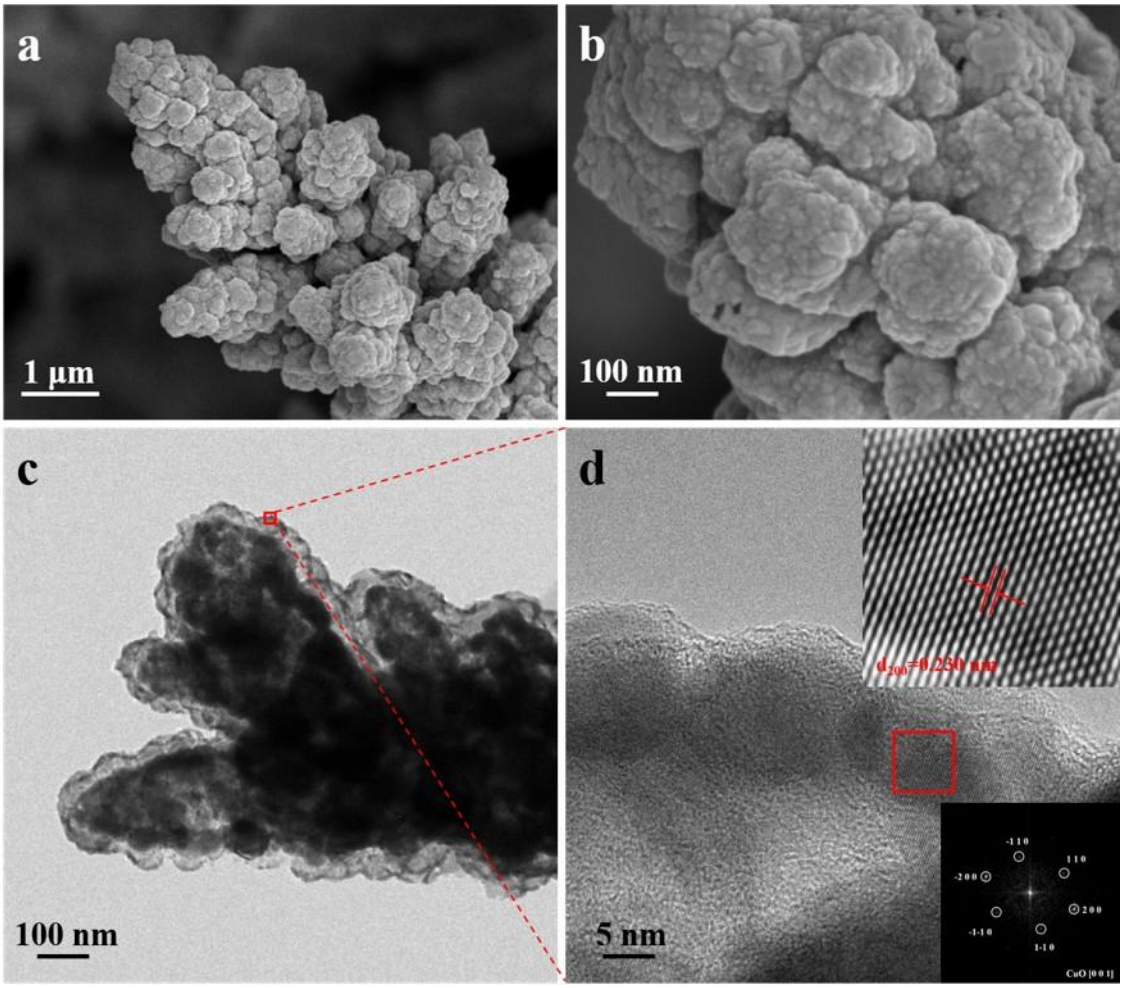

Figure 6.6 Low (a) and high magnification (b) SEM images of HS-CuO/C NDs; low magnification (c) and HRTEM (d) images of HS-CuO/C NDs.

The MOFs coated NDs were annealed in Ar atmosphere to induce the decomposition of HKUST-1, followed by the low-temperature heat treatment in air to form the CuO/C hollow shell coated NDs (HS-CuO/C NDs). For comparison, porous shell coated NDs (i.e. PS-CuO/C NDs and PS-CuO NDs) were also implemented by manipulating the annealing conditions (Figure 6.7). As a result, the smooth MOFs layer is converted into abundant nanoparticles but the dendritic morphology of the annealed samples is seen to be still preserved well (Figure 6.6a, b). TEM observation reveals that the hollow structure consisting of nanoparticles covers the dendrites as a shell (as shown in Figure 6.6c). The HRTEM image (Figure 6.6d) shows the hollow shell that is highly distinguishable from internal void identified from their strong TEM mass-thickness contrast. The fast fourier

transform (FFT) pattern generated from the marked area on the shell determines that the particle is CuO and oriented in the projection plane of (0 0 1). In addition, these crystalline CuO nanoparticles are found to be incorporated with amorphous carbon, which can be further verified by the scanning transmission electron microscopy-energy dispersive X-ray (STEM-EDX) mapping analysis (Figure 6.8).

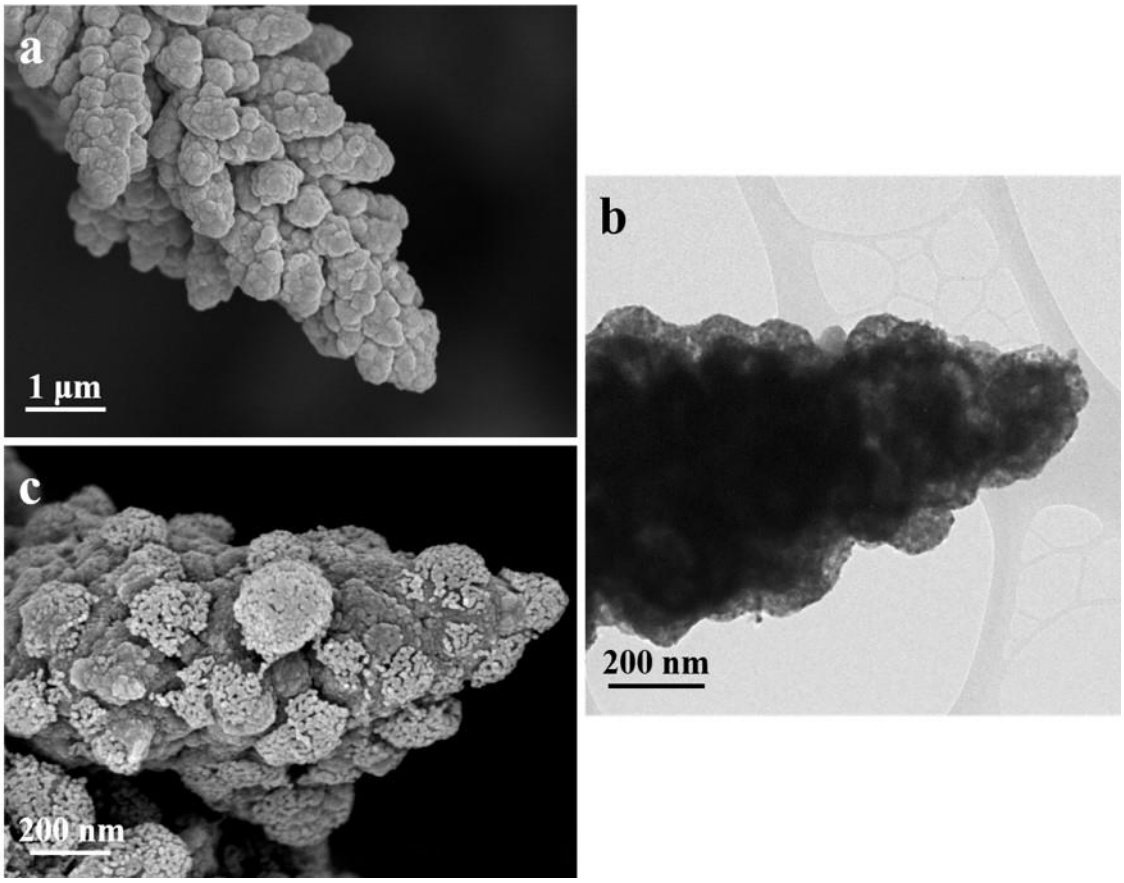

Figure 6.7 SEM (a) and TEM (b) images of PS-CuO/C NDs; (c) SEM image of PS-CuO NDs.

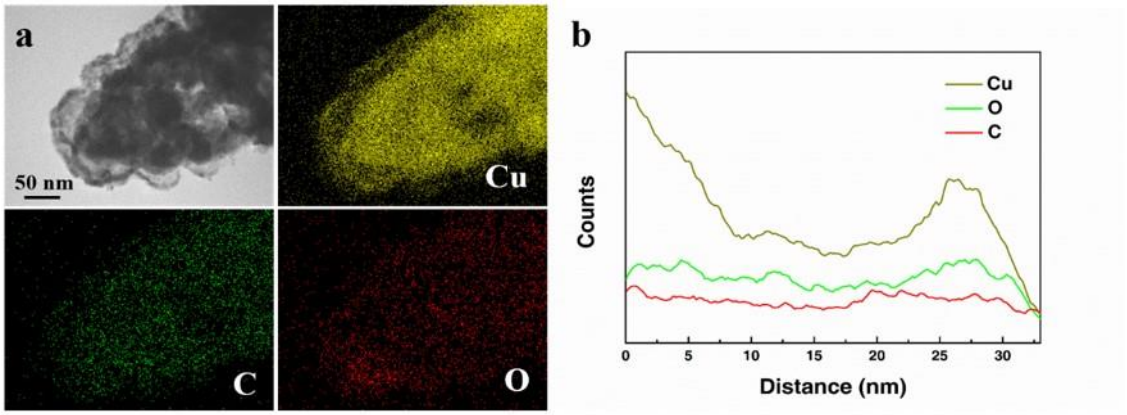

Figure 6.8 STEM-EDX mapping (a) and inside-out line scan (b) of HS-CuO/C NDs.

To further understand the composition and valence states of the CuO/C hollow shell, X-ray photoelectron spectroscopy (XPS) was employed. The XPS survey of HS-CuO/C NDs shows the existence of C, O and Cu elements (Figure 6.9a). The C 1s spectrum can be deconvoluted into three peaks at around 284.6, 286.2 and 288.7 eV (Figure 6.9d). The peak located at 284.6 eV corresponds to the C–C bond of graphitized carbon, whilst the peaks at 286.2 and 288.7 eV are assigned to the C–O and C=O bonds, respectively.[39] Moreover, two characteristic peaks at 1360 and 1580 cm^{-1} in Raman spectrum (Figure 6.10) indicate the coexistence of amorphous carbon and graphitized carbon within the hollow shell.[40] As shown in Figure 6.9b, two spin-orbit doublets are fitted well with the Cu 2p spectrum, where two characteristic peaks at 933.9 eV and 953.8 eV are respectively allocated to Cu $2p_{3/2}$ and Cu $2p_{1/2}$. Typical shake-up peaks are also detected to accompany two Cu 2p peaks, indicating the Cu-species in the hollow shell is CuO.[41]

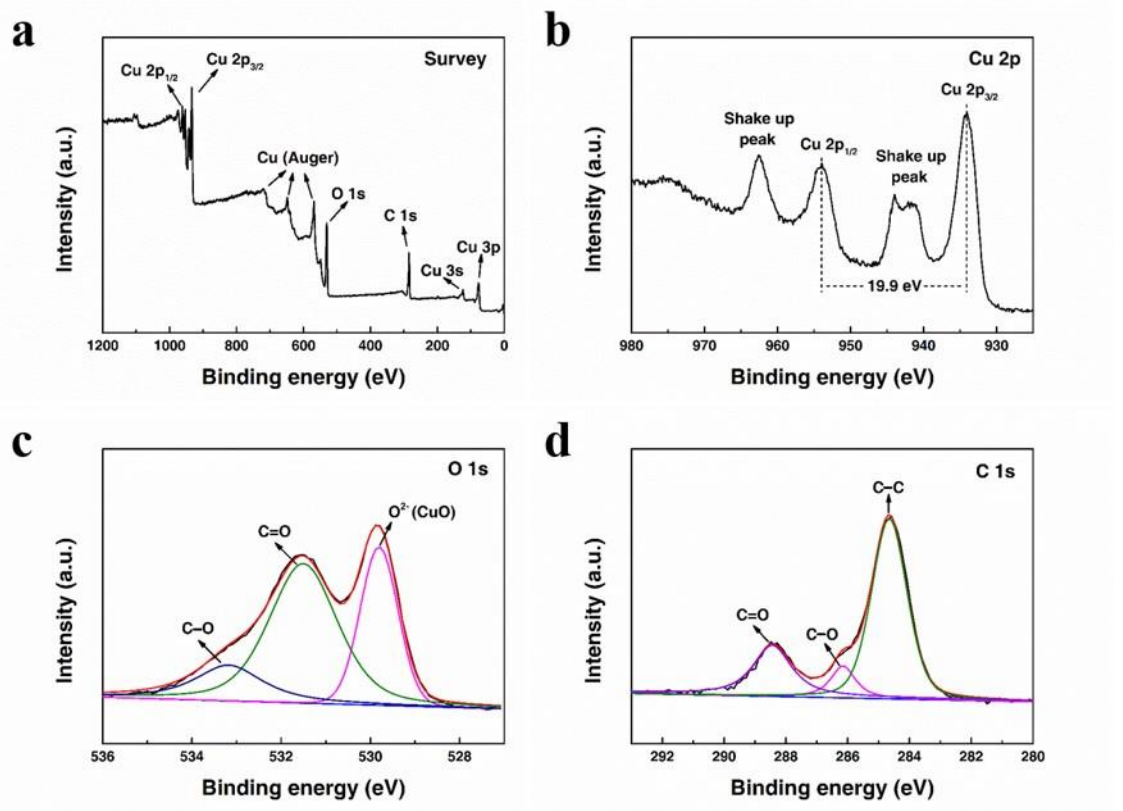

Figure 6.9 Survey XPS spectrum (a), high resolution XPS spectra of Cu 2p (b) O 1s (c) and C 1s (d).

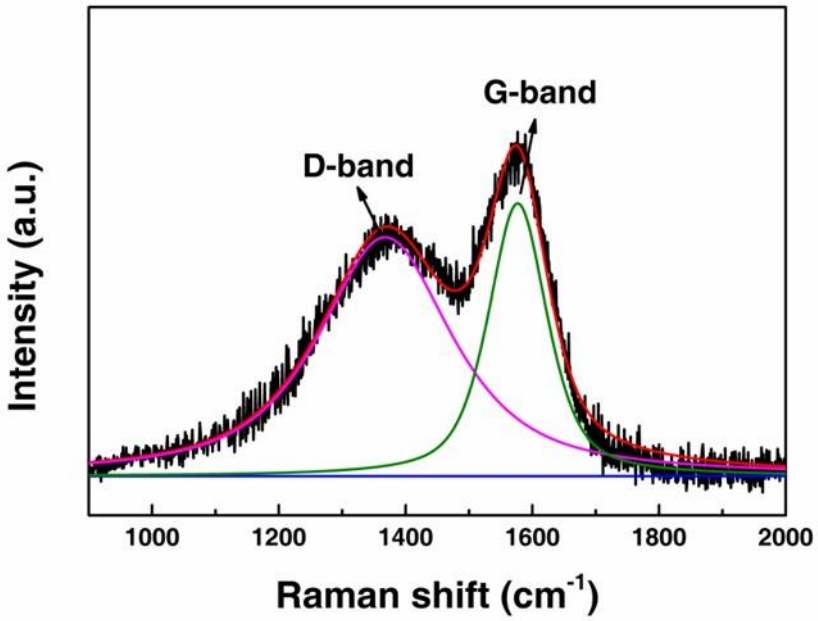

Figure 6.10 Raman spectra of HS-CuO/C NDs.

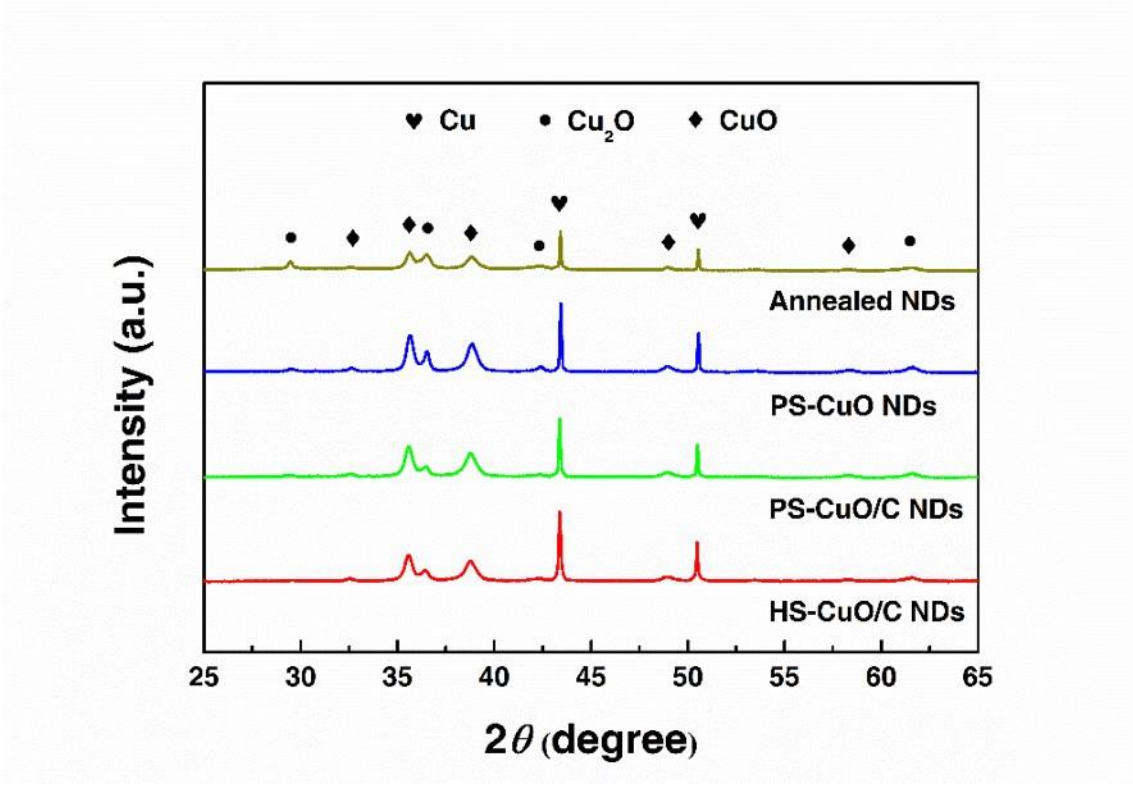

Figure 6.11 XRD patterns of HS-CuO/C NDs, PS-CuO/C NDs, PS-CuO NDs and Annealed NDs.

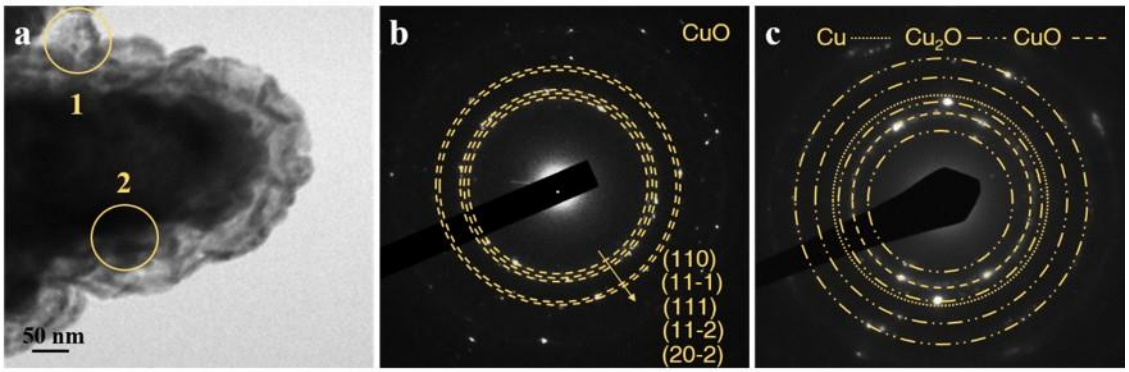

Figure 6.12 (a) TEM image of HS-CuO/C NDs; SAED patterns of circle 1 (b) and 2 (c) in sub-figure a.

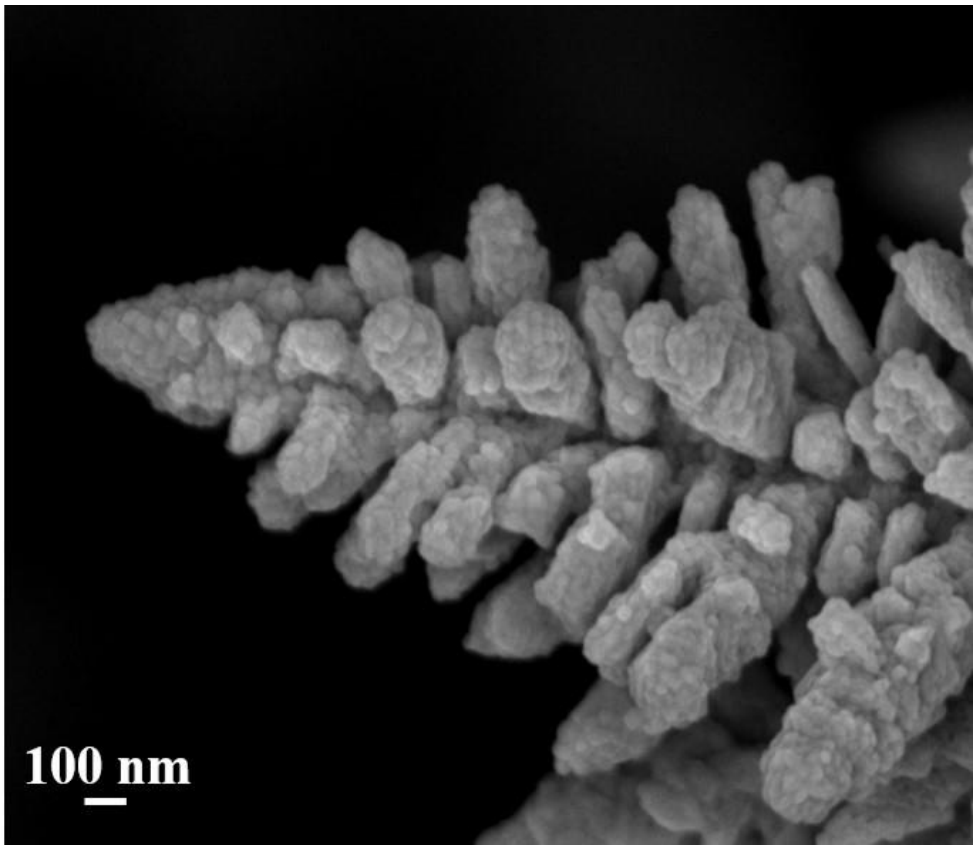

Figure 6.13 SEM image of Annealed NDs.

XRD measurement has been carried out to explore the phase information of the as-prepared NDs. As shown in Figure 6.11, the diffraction patterns of all NDs samples appear similar. Besides the peaks attributed to Cu and CuO, several Cu_2O peaks are also visible but were not determined in the hollow shell by HRTEM observation.

To gain better understanding of the internal structure of this CuO/C hollow-shell, selected area electron diffraction (SAED) was performed inside-out on the NDs. Based on the SAED patterns (Figure 6.12), a polycrystalline Cu_2O/CuO layer is grown adjacent to the Cu NDs as a stable core whilst only CuO exists in the hollow shell. During the low-temperature annealing in air, O_2 molecules penetrate the hollow shell and partially oxidize the inner Cu_2O film to form a Cu_2O/CuO passive layer. This robust passive layer plays a key role in sustaining the stability of HS-CuO/C NDs for water oxidation in alkaline media, which will be discussed below.

6.3.2 OER Electrocatalysis Evaluation of CuNDs-based Materials

The OER activities of the 3D dendritic catalysts were carried out in 1.0 KOH solution. As illustrated in Chapter 5, the bare CuNDs would undergo a non-equilibrium oxidation process during the electrochemical polarization in alkaline solution and produces a composites with very low activity for OER. To overcome this problem, MOFs layer is coated over the surface of annealed NDs catalysts. This coating, on the one hand, acts as a protective layer to stabilize the annealed NDs in alkaline solution (Figure 6.13). One the other hand, this layer further improves activities for water oxidation of NDs. PS-CuO/C NDs only requires an overpotential of 308 mV to reach a current density of 10 mA^{-2} (Figure 6.14b), which is 15 mV lower than PS-CuO NDs due to the better conductivity fulfilled by carbon incorporation. Moreover, HS-CuO/C NDs with finely tuned hollow shell presents an even superior OER activity, where current densities of 10 and 100 mA cm^{-2} are achieved only at overpotentials of 286 mV and 482 mV, respectively. To our best knowledge, this activity is among the best of Cu-based OER electrocatalysts (Table 6.1). The kinetic analysis of OER is performed by measuring the Tafel slope gradients that are calculated from the LSV profiles (Figure 6.14c). Among the NDs catalysts, HS-CuO/C NDs exhibits the lowest Tafel slope gradient (66.3 mV dec^{-1}), suggesting its best reaction kinetics for OER, which is consistent to the LSV results.

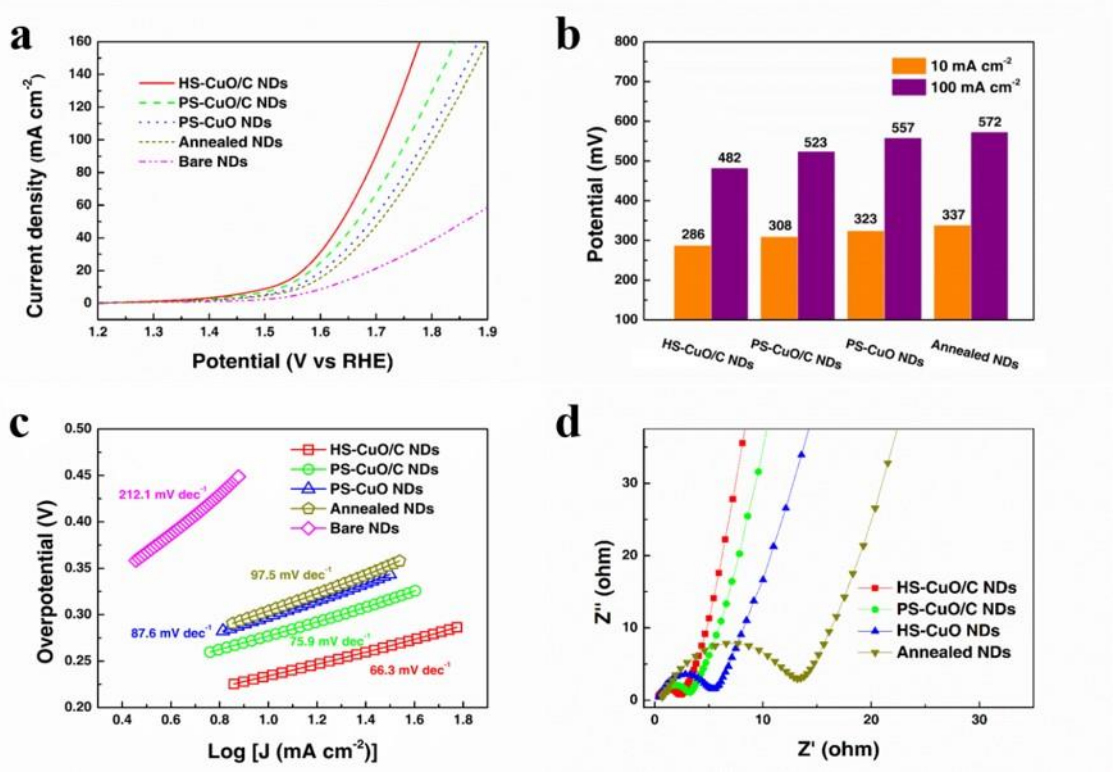

Figure 6.14 (a) LSV curves of as-prepared NDs electrodes in 1.0 M KOH solution at a scan rate of 5 mV s^{-1}; (b) comparison of overpotential required for the NDs electrodes at 10 mA cm^{-2} and 100 mA cm^{-2}; Tafel plots (c) and Nyquist plots (d) of the NDs electrodes.

In order to further investigate the superior electrochemical performance offered by the nanostructured hollow shell, electrochemical double layer capacitance (C_{dl}) of both HS-CuO/C NDs and PS-CuO/C NDs is measured to estimate their electrochemically active surface area (ECSA).[42] As illustrated in Figure 6.15, the calculated C_{dl} of HS-CuO/C NDs 173.2 mF cm^{-2} is much higher than that of PS-CuO/C NDs 128.6 mF cm^{-2}, which is enriched with the abundant active sites within the hollow space, where a larger ECSA of HS-CuO/C NDs is achieved. Figure 6.14d shows the electrochemical impedance spectroscopy (EIS) spectra of the NDs electrodes. All the EIS spectra exhibit similar tendency, consisting of a semicircle and a straight line, which represents high frequency region and low frequency region respectively. The diameter of the semicircle corresponding to the charge transfer resistance (R_{ct}) is associated with the redox reactions on the surface of the catalyst whilst the straight line is attributed to the electrolyte diffusion within the electrode. Owing to the highly conductive inner Cu core, the charge-transfer

resistance of the NDs electrodes all show low with the R_{ct} value of the HS-CuO/C NDs being only ~ 2.6 Ω, lower than those of PS-CuO/C NDs (3.5 Ω) and PS-CuO NDs (5.7 Ω). It is reasonable that the lowest R_{ct} of HS-CuO/C NDs serves as an electrode where the redox reactions occur, leading to the extraordinary electrocatalytic activity.

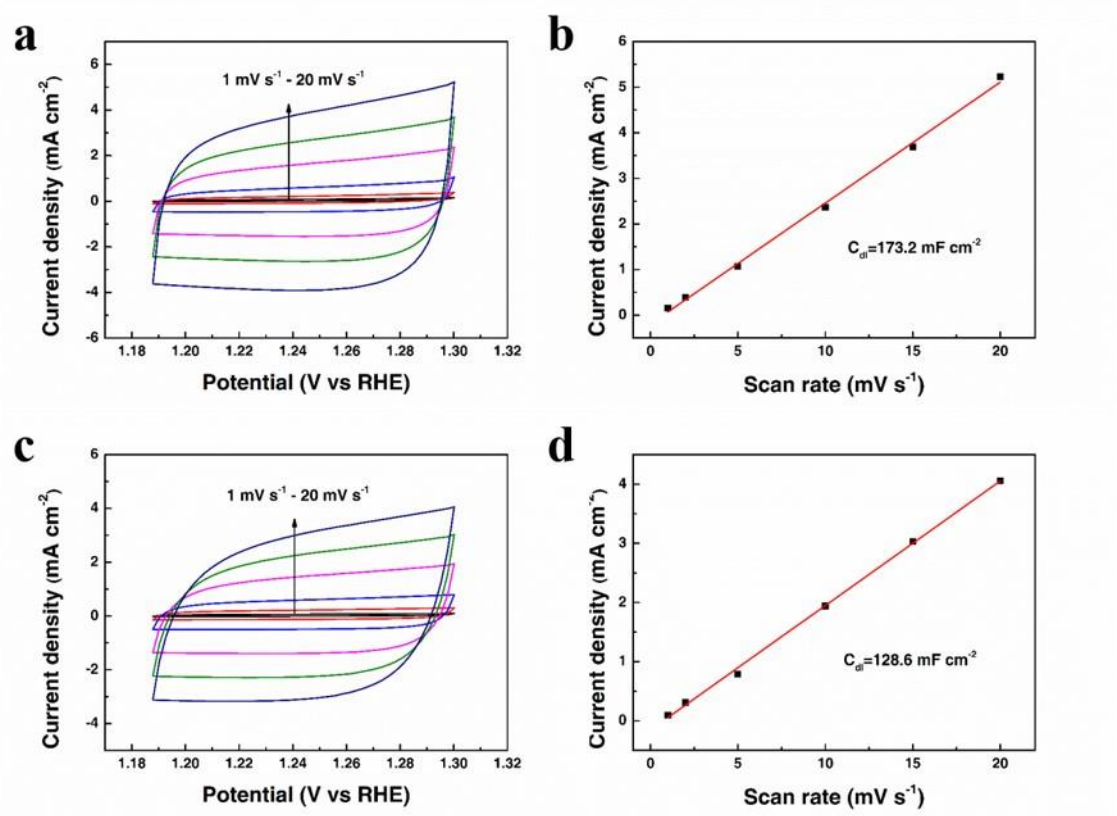

Figure 6.15 CVs at different scan rates (a) and capacitive current as a function of scan rate (b) for HS-CuO/C NDs; CVs at different scan rates (c) and capacitive current as a function of scan rate (d) for PS-CuO/C NDs.

As one of the most vital criteria for an electrocatalyst in water splitting, the electrochemical long-term stability of electrode is required. As such, three NDs electrodes were tested using chronopotentiometric method in 1.0 KOH at 10 mA cm^{-2} for 50 hours. As illustrated in Figure 6.16, HS-CuO/C NDs and PS-CuO/C NDs electrodes with carbon incorporation only show slightly increase in potential to sustain the 10 mA cm^{-2} current density. In contrast, an obvious potential rise of over 200 mV is observed for bare PS-CuO NDs. The distinct different responses above demonstrates the crucial role that carbon is played in the stability of electrodes.

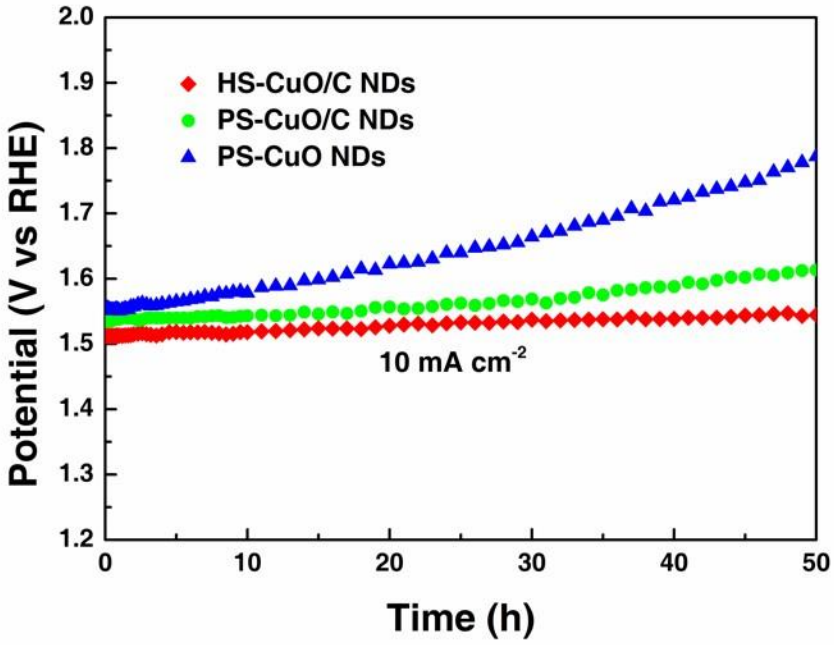

Figure 6.16 Chronopotentiometry curves of HS-CuO/C NDs, PS-CuO/C NDs and PS-CuO NDs at a constant current density of 10 mA cm^{-2}.

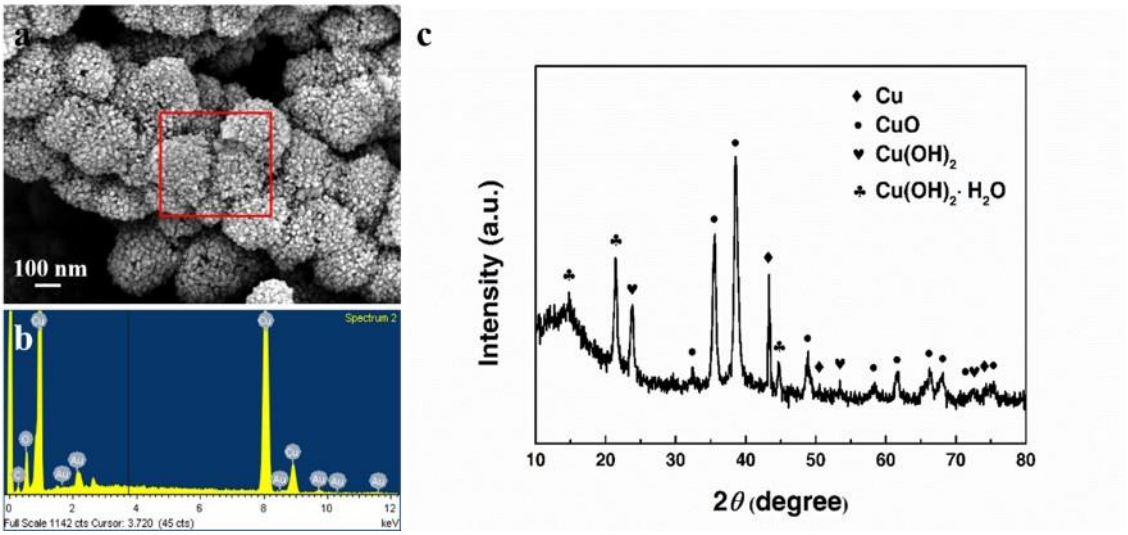

Figure 6.17 SEM image (a), EDX spectrum (b) and XRD pattern (c) of HS-CuO/C NDs after stability test.

In addition, the morphology and phase information of HS-CuO/C NDs after 50 hours' electrolysis at 10 mA cm^{-2} were performed by SEM and XRD. As shown in Figure 6.17a,

the overall dendrite feature and the nanostructured hollow shell coated on the surface remain intact. It is noticeable that the long-term electrolysis allows the high-density transportation of electrolyte and subsequent generation process of O_2 bubbles across the hollow shell, leading to a more porous surface of HS-CuO/C NDs compared to the original ones. Based on the EDX result in Figure 6.17b, the existence of carbon within the hollow shell is confirmed, greatly contributing to the stability of the HS-CuO/C NDs electrode. In the XRD pattern (Figure 6.17c), $Cu(OH)_2$ species are identified due to the hydration of the copper oxides in alkaline solution.[43, 44]

Table 6.1 Comparisons of electrocatalytic activities of some reported Cu-based OER electrocatalysts in alkaline media.

Catalyst	**Electrolyte**	**Overpotential at 10 mA cm^{-2} (η_{10}, mV)**	**Tafel slope (mV dec^{-1})**	**Reference**
HS-CuO/C NDs	1.0 M KOH	286	66.3	This work
PS-CuO/C NDs	1.0 M KOH	308	75.9	This work
Cu-N-C/graphene	0.1 M KOH	>770	N.A.	[45]
$Cu/Cu(OH)_2$-CuO nanorods	0.1 M KOH	417	76	[46]
$Cu(OH)_2$ nanowires/copper foam	0.1 M NaOH	430	86	[18]
Cu oxide film	1.0 M KOH	430	N.A.	[47]
2D CuO nanosheet	1.0 M KOH	350	59	[34]
$Cu(OH)_2$	1.0 M KOH	470	78	[35]
CuO nanowire	1.0 M KOH	340	54.5	[48]
CuO	1.0 M KOH	370	90	[49]
CuO	0.1 M KOH	340	N.A.	[50]
$Cu(OH)_2$@ LDH	1.0 M KOH	350	95	[51]
CuO/CF	1.0 M KOH	430	44	[52]
Cu_3P/CuO@NF	1.0 M KOH	330	54	[53]
Cu_3P NB/Cu	1.0 M KOH	380	72	[54]
Cu_3P-450	1.0 M KOH	290	83	[55]

6.4 Conclusions

The present research work reports a facile and effective surface modification approach that involves the growth of MOFs over the surface of Cu-based NDs followed by the heat treatment forming a CuO_x/C@ Cu core/shell electrode. The hollow shell nature of nanostructured CuO/C offers the NDs electrode an extraordinary OER activity, which is among the highest efficient Cu-based catalysts. The spherical porous structure not only provides a high surface area, but also facilitates the diffusion of the electrolyte and the evolved O_2 bubbles, which makes it a potential candidate for electrocatalysis. The favorable OER kinetics on the nanostructured CuO/C hollow shell is supported by the core-shell structure, where the highly conductive copper core allows the high speed electronic transmission to the thin shell. The inner passive film adjacent to the hollow shell prevents the degradation of the catalyst and stabilizes electrolysis towards a long term. By virtue of the versatility of NDs, the fabrication strategy here can be extended to the synthesis of more core-shell materials for energy conversion and storage applications.

References

[1] Anantharaj, S.; Ede, S. R.; Sakthikumar, K.; Karthick, K.; Mishra, S.; Kundu, S., *ACS Catal.*, **2016**, 6(12): 8069-8097.

[2] Roger, I.; Shipman, M. A.; Symes, M. D., *Nat. Rev. Chem.* **2017,** *1*, 0003.

[3] Zou, X.; Zhang, Y., *Chem. Soc. Rev.* **2015,** *44* (15), 5148-5180.

[4] Jiao, Y.; Zheng, Y.; Jaroniec, M.; Qiao, S. Z., *Chem. Soc. Rev.* **2015,** *44* (8), 2060-2086.

[5] Xu, K.; Ding, H.; Jia, K.; Lu, X.; Chen, P.; Zhou, T.; Cheng, H.; Liu, S.; Wu, C.; Xie, Y., *Angew. Chem. Int. Ed.* **2016,** *55* (5), 1710-1713.

[6] Cao, R.; Lai, W.; Du, P., *Energy Environ. Sci.* **2012,** *5* (8), 8134-8157.

[7] McCrory, C. C.; Jung, S.; Peters, J. C.; Jaramillo, T. F., *J. Am. Chem. Soc.* **2013,** *135* (45), 16977-16987.

[8] Lu, Z.; Wang, H.; Kong, D.; Yan, K.; Hsu, P.-C.; Zheng, G.; Yao, H.; Liang, Z.; Sun, X.; Cui, Y., *Nat. Commun.* **2014,** *5*, 5345.

[9] Chen, P.; Xu, K.; Fang, Z.; Tong, Y.; Wu, J.; Lu, X.; Peng, X.; Ding, H.; Wu, C.; Xie, Y., *Angew. Chem.* **2015,** *127* (49), 14923-14927.

[10] Kim, J.; Yin, X.; Tsao, K.-C.; Fang, S.; Yang, H., *J. Am. Chem. Soc.* **2014,** *136* (42), 14646-14649.

[11] Xu, Y.; Tu, W.; Zhang, B.; Yin, S.; Huang, Y.; Kraft, M.; Xu, R., *Adv. Mater.* **2017,** *29* (11).

[12] Zhang, Y.; Xia, X.; Cao, X.; Zhang, B.; Tiep, N. H.; He, H.; Chen, S.; Huang, Y.; Fan, H. J., *Adv. Energy Mater.* **2017**, 7(15).

[13] Guan, B. Y.; Yu, L.; Lou, X. W. D., *Angew. Chem. Int. Ed.* **2017,** *56* (9), 2386-2389.

[14] Su, J.; Xia, G.; Li, R.; Yang, Y.; Chen, J.; Shi, R.; Jiang, P.; Chen, Q., *J. Mater. Chem. A* **2016,** *4* (23), 9204-9212.

[15] Lee, D.-G.; Kim, S. H.; Joo, S. H.; Ji, H.-I.; Tavassol, H.; Jeon, Y.; Choi, S.; Lee, M.-H.; Kim, C.; Kwak, S. K., *Energy Environ. Sci.* **2017,** *10* (2), 523-527.

[16] Yu, X.-Y.; Feng, Y.; Guan, B.; Lou, X. W. D.; Paik, U., *Energy Environ. Sci.* **2016,** *9* (4), 1246-1250.

[17] Bak, W.; Kim, H. S.; Chun, H.; Yoo, W. C., *Chem. Commun.* **2015,** *51* (33), 7238-7241.

[18] Hou, C. C.; Fu, W. F.; Chen, Y., *ChemSusChem* **2016,** *9* (16), 2069-2073.

[19] Du, J.; Chen, Z.; Ye, S.; Wiley, B. J.; Meyer, T. J., *Angew. Chem. Int. Ed.* **2015,** *54* (7), 2073-2078.

[20] Zhou, L.; Shao, M.; Zhang, C.; Zhao, J.; He, S.; Rao, D.; Wei, M.; Evans, D. G.; Duan, X., *Adv. Mater.* **2017,** *29* (6).

[21] Yu, F.; Li, F.; Zhang, B.; Li, H.; Sun, L., *ACS Catal.* **2014,** *5* (2), 627-630.

[22] Guo, D.; Shibuya, R.; Akiba, C.; Saji, S.; Kondo, T.; Nakamura, J., *Science* **2016,** *351* (6271), 361-365.

[23] Chung, H. T.; Cullen, D. A.; Higgins, D.; Sneed, B. T.; Holby, E. F.; More, K. L.; Zelenay, P., *Science* **2017,** *357* (6350), 479-484.

[24] Kibsgaard, J.; Jaramillo, T. F.; Besenbacher, F., *Nat. Chem.* **2014,** *6* (3), 248-253.

[25] Yilmaz, G.; Yam, K. M.; Zhang, C.; Fan, H. J.; Ho, G. W., *Adv. Mater.* **2017**.

[26] Huang, Z.-F.; Song, J.; Li, K.; Tahir, M.; Wang, Y.-T.; Pan, L.; Wang, L.; Zhang, X.; Zou, J.-J., *J. Am. Chem. Soc.* **2016,** *138* (4), 1359-1365.

[27] Yu, L.; Wu, H. B.; Lou, X. W. D., *Acc. Chem. Res.* **2017,** *50* (2), 293-301.

[28] Hao, S.; Zhang, B.; Ball, S.; Wu, J.; Srinivasan, M.; Huang, Y., *J. Mater. Chem. A* **2016,** *4* (42), 16569-16575.

[29] Yang, S.; Peng, L.; Huang, P.; Wang, X.; Sun, Y.; Cao, C.; Song, W., *Angew. Chem. Int. Ed.* **2016,** *55* (12), 4016-4020.

[30] Wang, C.; Sun, L.; Zhang, F.; Wang, X.; Sun, Q.; Cheng, Y.; Wang, L., *Small* **2017,** *13* (32).

[31] Wu, Z.; Liu, R.; Wang, J.; Zhu, J.; Xiao, W.; Xuan, C.; Lei, W.; Wang, D., *Nanoscale* **2016,** *8* (45), 19086-19092.

[32] Huan, T. N.; Rousse, G.; Zanna, S.; Lucas, I. T.; Xu, X.; Menguy, N.; Mougel, V.; Fontecave, M., *Angew. Chem.* **2017,** *129* (17), 4870-4874.

[33] Xu, H.; Feng, J.-X.; Tong, Y.-X.; Li, G.-R., *ACS Catal.* **2016,** *7* (2), 986-991.

[34] Im, H.; Pawar, S. M.; Pawar, B.; Hou, B.; Kim, J.; Talha, A. A.; Chavan, H. S.; Jo, Y.; Cho, S.; Inamdar, A., *J. Mater. Chem. A* **2017**.

[35] Cui, S.; Liu, X.; Sun, Z.; Du, P., *J. Phys. Chem. C*, **2016**, 120(2): 831-840

[36] Shin, H.-C.; Liu, M., *Chem. Mater.* **2004,** *16* (25), 5460-5464.

[37] Yang, Q.; Liu, W.; Wang, B.; Zhang, W.; Zeng, X.; Zhang, C.; Qin, Y.; Sun, X.; Wu, T.; Liu, J., *Nat. Commun.* **2017,** *8*, 14429.

[38] Plowman, B. J.; Jones, L. A.; Bhargava, S. K., *Chem. Commun.* **2015,** *51* (21), 4331-4346.

[39] Ni, Y.; Yao, L.; Wang, Y.; Liu, B.; Cao, M.; Hu, C., *Nanoscale* **2017,** *9* (32), 11596-11604.

[40] Fan, L.; Liu, P. F.; Yan, X.; Gu, L.; Yang, Z. Z.; Yang, H. G.; Qiu, S.; Yao, X., *Nat. commu.* **2016,** *7*, 10667.

[41] Chawla, S.; Sankarraman, N.; Payer, J., *J. Electron. Spectrosc. Relat. Phenom.* **1992,** *61* (1), 1-18.

[42] Le Formal, F.; Tétreault, N.; Cornuz, M.; Moehl, T.; Grätzel, M.; Sivula, K., *Chem. Sci.* **2011,** *2* (4), 737-743.

[43] Wu, J.; Li, X.; Yadian, B.; Liu, H.; Chun, S.; Zhang, B.; Zhou, K.; Gan, C. L.; Huang, Y., *Electrochem. Commun.* **2013,** *26*, 21-24.

[44] Zhang, B.; Chen, B.; Wu, J.; Hao, S.; Yang, G.; Cao, X.; Jing, L.; Zhu, M.; Tsang, S. H.; Teo, E. H. T., *Small* **2017,** *13* (10).

[45] Wang, J.; Wang, K.; Wang, F.-B.; Xia, X.-H., *Nat. commun.* **2014,** *5*, 5285.

[46] Cheng, N.; Xue, Y.; Liu, Q.; Tian, J.; Zhang, L.; Asiri, A. M.; Sun, X., *Electrochim. Acta* **2015,** *163*, 102-106.

[47] Liu, X.; Cui, S.; Sun, Z.; Ren, Y.; Zhang, X.; Du, P., *J. Phys. Chem. C* **2016,** *120* (2), 831-840.

[48] Liu, X.; Cui, S.; Sun, Z.; Du, P., *Electrochim. Acta* **2015,** *160*, 202-208.

[49] Liu, X.; Cui, S.; Qian, M.; Sun, Z.; Du, P., *Chem. Commun.* **2016,** *52* (32), 5546-5549.

[50] Handoko, A. D.; Deng, S.; Deng, Y.; Cheng, A. W. F.; Chan, K. W.; Tan, H. R.; Pan, Y.; Tok, E. S.; Sow, C. H.; Yeo, B. S., *Catal. Sci. Technol.* **2016,** *6* (1), 269-274.

[51] Ma, X.; Li, X.; Jagadale, A. D.; Hao, X.; Abudula, A.; Guan, G., *Int. J. Hydrogen Energy* **2016,** *41* (33), 14553-14561.

[52] Lu, C.; Wang, J.; Czioska, S.; Dong, H.; Chen, Z., *J. Phys. Chem. C* **2017,** *121* (46), 25875-25881.

[53] Han, A.; Zhang, H.; Yuan, R.; Ji, H.; Du, P., *ACS Appl. Mater. Interfaces* **2017,** *9* (3), 2240-2248.

[54] Wei, S.; Qi, K.; Jin, Z.; Cao, J.; Zheng, W.; Chen, H.; Cui, X., *ACS Omega* **2016,** *1* (6), 1367-1373.

[55] Hao, J.; Yang, W.; Huang, Z.; Zhang, C., *Adv. Mater. Interfaces* **2016,** *3* (16).

Chapter 7

Discussion and Future Work

In the present part, the general conclusions of the thesis were drawn, where the implications, impact and outstanding questions were included. To be more specific, single-crystalline CuNWs were synthesized via electrodeposition followed by the study of their electrochemical behaviors in atmospheric air and alkaline solution. The electrochemical behavior and OER performance of the electrodeposited hierarchical CuNDs was also investigated in the alkaline solution. An improve OER activity was achieved by surface modification strategy to coat a nanostructured CuO/C hollow shell on the surface of CuNDs. In addition, future work about the mechanism study of electrochemical behaviors of copper nanostructures were also discussed. Finally, the summary of the thesis was illustrate to explain the outcomes that were reflected in the original hypotheses.

7.1 General Discussion

In this thesis, the electrochemical behaviors of single crystalline CuNWs and hierarchical CuNDs were discussed, followed by the evaluation of electrocatalytic activities of Cu-based NDs. Specifically, the electrochemical behaviors of single-crystalline CuNWs in atmospheric air and alkaline solution were firstly studied. Then, the electrochemical behavior hierarchical CuNDs in the alkaline solution was also investigated followed by the study of their electrocatalytic activity for OER. In order to improve their OER performance, surface modification strategy was employed by coating various nanostructured CuO shells on the surface of CuNDs.

First, the electrochemical behavior of single crystalline CuNWs atmospheric air and alkaline solution has been studied by TEM. The results show that a uniform Cu_2O film is found to epitaxially grow on the CuNW surfaces following the logarithmic law growth rate with the increase of exposure duration of CuNWs in 40 % RH air and the growth rate is much higher than those formed on their bulky counterpart. The electrochemical behavior of CuNWs in alkaline solution is studied by CV. Initially, a homogeneously epitaxial Cu_2O layer is formed and covers the CuNW substrates at low potentials and then it will convert into CuO at higher polarization potentials following SSR mechanism whilst the DR process of the partial CuO results in the formation of outer layer of $Cu(OH)_2$ mixed with CuO. The thickness of outer layer will increase at the expense of inner Cu_2O layer during the continuous rise of the potential. In addition, the parallel alignment CuO layer adjacent to the CuNW substrate disappears prior to the oxygen evolution potential, which is replaced by a dual-layer ($CuO/Cu(OH)_2$) film is formed on the CuNW surface.

Second, the electrochemical behaviors of hierarchical CuNDs in 0.1 M NaOH aqueous solution are studied by CV in combination with XRD, SEM and TEM. Initially, an epitaxially thin layer of Cu_2O is homogeneously formed on the CuNDs surface till the end of the first oxidation peak. Subsequently, $Cu(OH)_2$ nanoneedles start to nucleate and grow from the defective locations of the CuNDs followed by the oxidation of Cu_2O occurs. With the increase of potential, Cu_2O layer is completely transformed into CuO and $Cu(OH)_2$ as

a dual-layer structure. At the same time, $Cu(OH)_2$ nanoneedles undergo a the rapid growth over the surface of CuNDs. When being evaluated as an electrocatalyst for OER, the as-polarized CuNDs electrode presents a high overpotential due to the electrochemical degradation, which required a surface modification to boost their catalytic properties.

Last, a facile and effective surface modification approach that involves the growth of MOFs over the surface of Cu-based NDs is employed followed by the heat treatment forming a CuO_x/C@ Cu core/shell electrode. The nanostructured CuO/C hollow shell offers the NDs electrode an extraordinary OER activity, which is among the highest efficient Cu-based catalysts. Specifically, the overall porous structure of the foam makes it a potential candidate for electrocatalysis since it can not only provide a high surface area, but also facilitate the diffusion of the electrolyte and the evolved O_2 bubbles. Moreover, the Cu-CuO/C core-shell structure guarantees the favorable OER kinetics since the highly conductive copper core allows the high speed electronic transmission to the thin shell. Furthermore, the passive film beneath the hollow shell could protect the NDs from electrochemical degradation for a long time.

7.2 Reconnaissance Work not Included in Main Chapters

7.2.1 In situ TEM observation of electrochemical behaviors of one single CuNW

Although electrochemical behavior of single-crystalline CuNWs has been studied by TEM using ex situ TEM characterization. In situ TEM observation is still considered to be more convincing by providing direct information about the morphology and phase evolution of the CuNWs in the electrolyte.

Before electrochemical measurement under in situ TEM liquid cell holder, the in situ observation of a single CuNW under a flow of 6 M NaOH solution was initially conducted to monitor the morphological evolution of the individual CuNW. As shown in Figure 7.1, the overall morphological change of the CuNW in 6 M NaCl solution can be in situ observed.

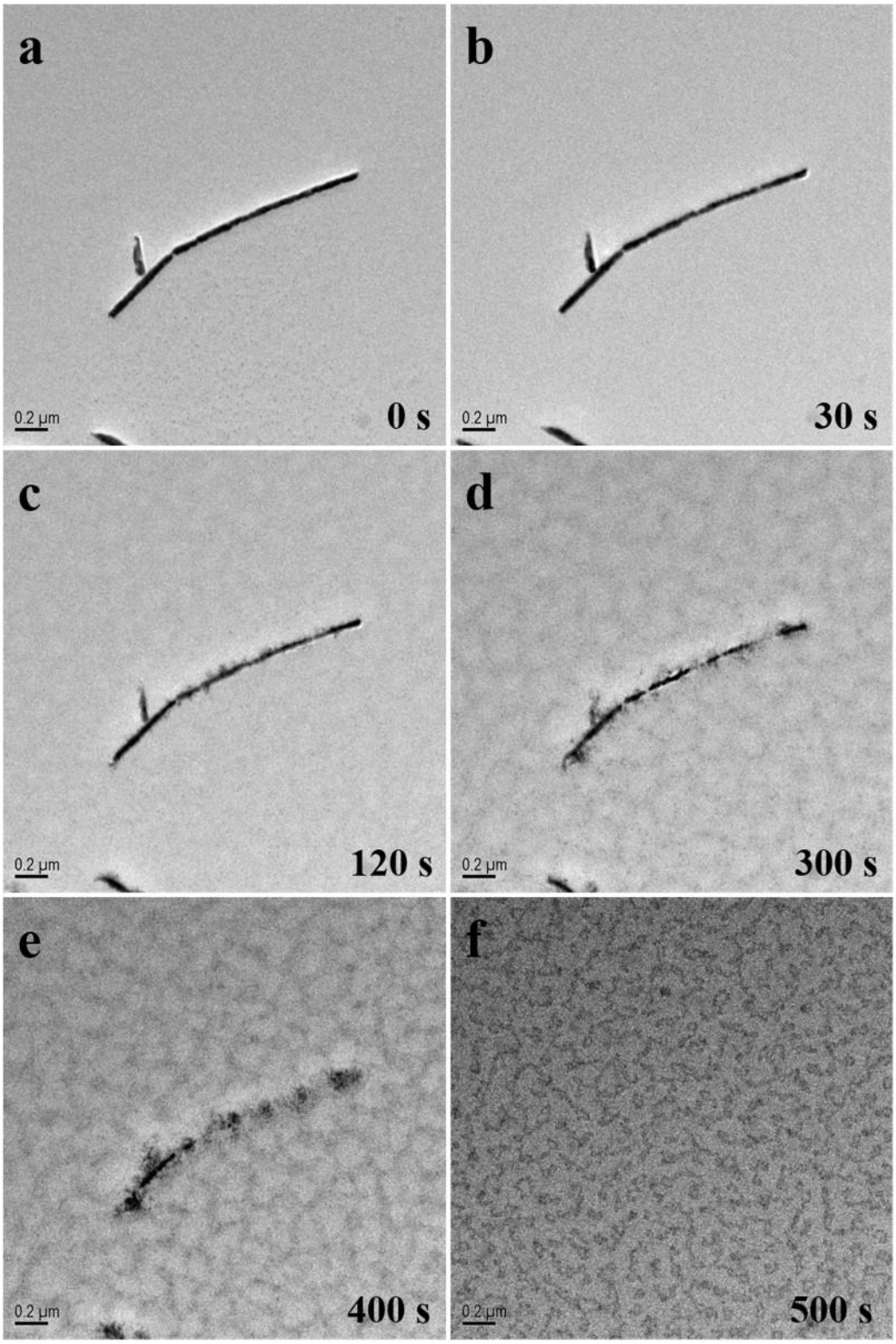

Figure 7.1 In situ TEM images of a single CuNW in 6 M NaCl solution for 0 s (a), 30 s (b), 120 s (c), 300 s (d), 400 s (e) and 500 (s), respectively.

Initially, the morphology of the CuNW changed little during the first 30 s. When the immersion time reached 120s as shown in Figure 7.1c, some dendrites were observed to appear on the surface of the CuNW at the expense of the decrease of the diameter of the CuNW. This is ascribed to the occurrence of pitting corrosion on the surface of CuNW, which is caused by the attack of high concentration chloride ions. With the increase of immersion time, the pitting corrosion became more severe so that part of the CuNW was broken due to the inhomogeneous dissolution to produce several discontinuous sections of the CuNW. The CuNW was completely dissolved into the 6 M NaCl solution after 500s, which can be distinguished by the low contrast of the image.

Although the in situ observation of the morphology evolution of an individual CuNW was accomplished, there are still many issues to be addressed before the further experiment was carried out successfully.

First, as shown in Figure 7.1, the resolution of the TEM image obtained by the in situ characterization using the electrochemical liquid cell holder. There are two main reasons: the strong electron scattering effect of the liquids (organic or inorganic); the other one is the thickness of the windows on the chips in the in situ holder.

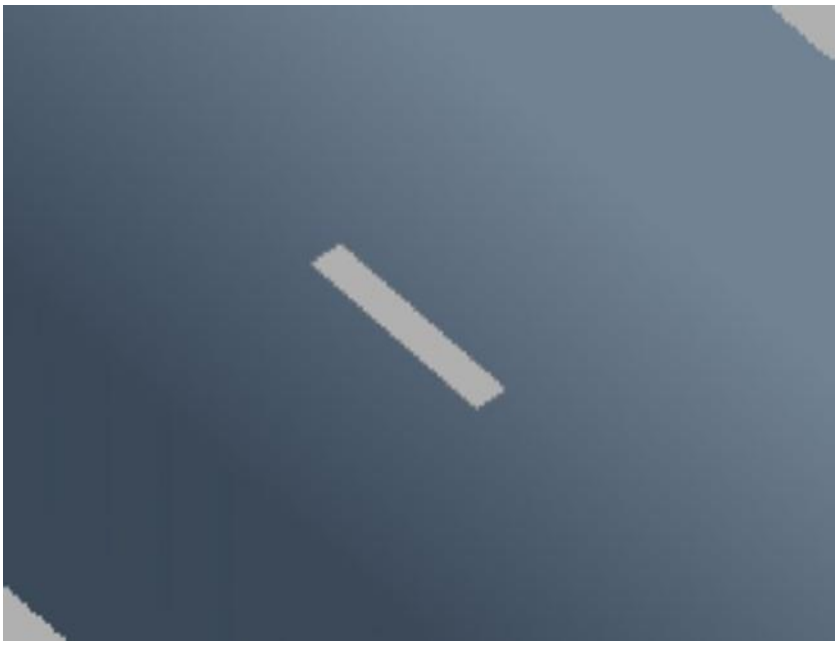

Figure 7.2 The chip for in situ TEM with a window in the center.

The thickness of the chip window in the current experiment is around 50 nm (Figure 7.2), which is made of silicon nitride. The spacer height between the two windows on the chips is 150 nm. The first issue could be solved by minimize the space distance between the up chip and the down chip, where less liquid was able to be contained in the small volume. The second issue can be solved by minimize the thickness of the silicon nitride window although this will increase the risk of the window breaking due to the decrease of mechanical strength. In the previous studies, micro window made of graphene was successfully used as the window material, where the thickness of the window was reduced and the mechanical strength of the graphene was excellent enough during the operation process.[1, 2]

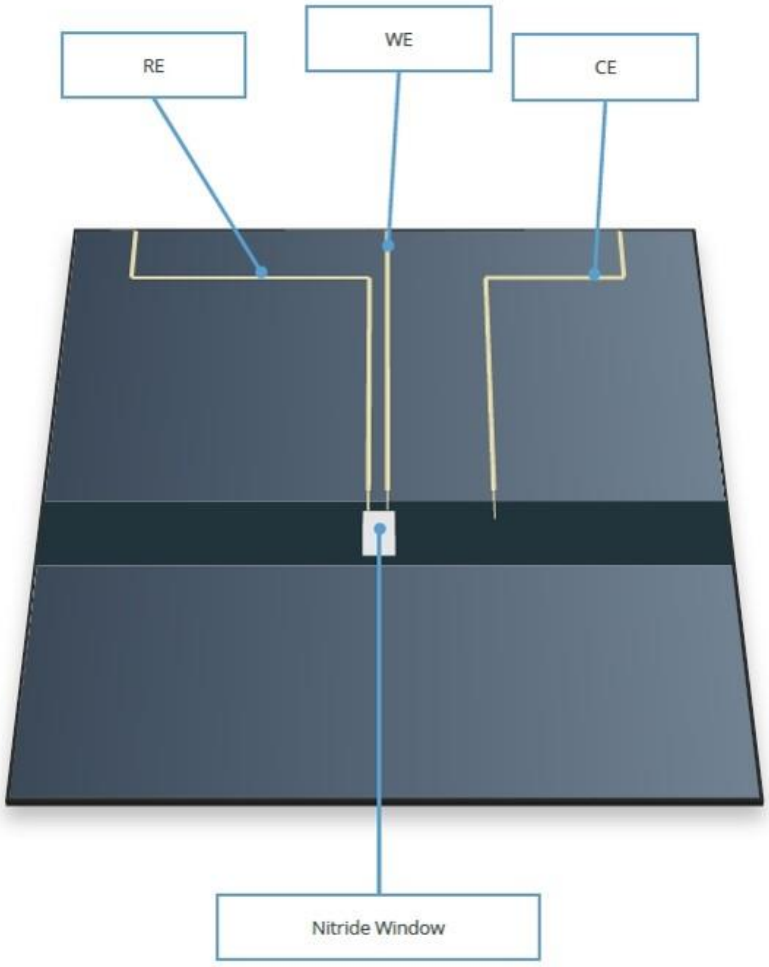

Figure 7.3 Layout of the down chip used for in situ liquid cell TEM holder for electrochemical experiment.

Compared to the immersion experiment in the in situ liquid cell holder, the electrochemical experiment in the same holder has much more challenges to be conquered in the future due to the increasing complexity of the chips and the operation.

Figure 7.3 present the layout of the chip of in situ liquid cell TEM holder for the electrochemical measurement. In order to create a three-electrode system, the target materials to be observed must be connected to the working electrode, which is made of glassy carbon film. For the current CuNW case, a single nanowire should be transferred to the chip and stick to the glassy carbon electrode firmly so that it won't flow away during the electrochemical test. Therefore, focused ion beam (FIB) was used to transfer the CuNW onto the chip and fix it on the surface of the window so that it could be used as the working electrode and observed under in situ TEM.

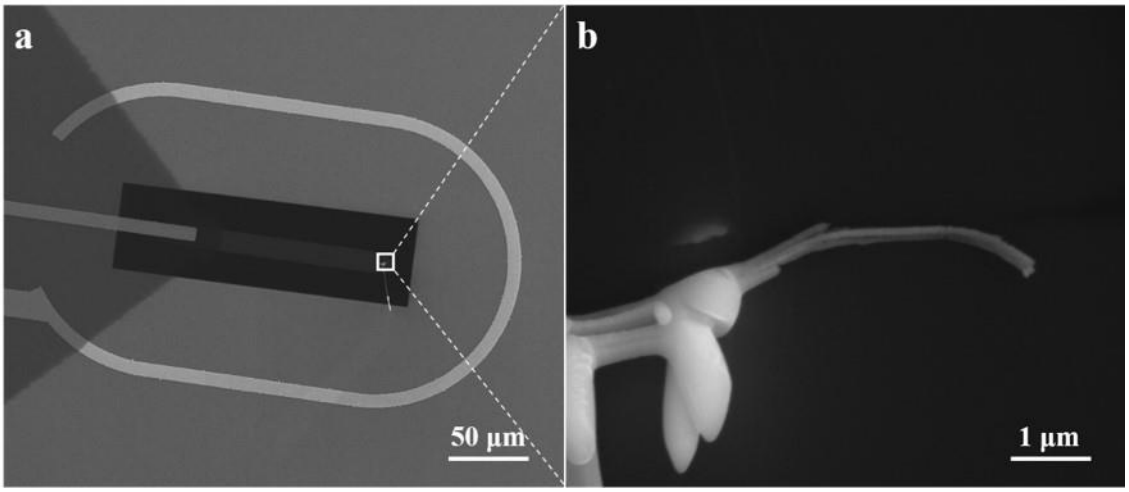

Figure 7.4 Fabrication of single CuNW electrode on the chip for in situ TEM characterization under electrochemical measurement.

Since it was very challenging to pick up a single CuNW by the omni-probe in FIB, a small branch of CuNWs consisting of several CuNWs was picked up and transferred to the in situ chip and fixed on the window position, which is shown in Figure 7.4. The bright spot in Figure 4b is the Pt deposition in order to connect the CuNWs to the silicon nitride window firmly prior to be sealed in the liquid cell holder and in situ observed under TEM with the application of electrochemical measurement.

Upon the observation under TEM, it was found that the CuNWs presented to be porous as shown in Figure 7.5. This was probably due to the damage by the gallium ion beam with strong intensity in FIB during the connection and disconnection procedures for several times. Moreover, many nanoparticles were also observed to cover around the CuNWs on the chip window, which was believed to be generated during the welding process by the contamination of the Pt source as the soldering material when connecting the CuNWs to the window substrate.

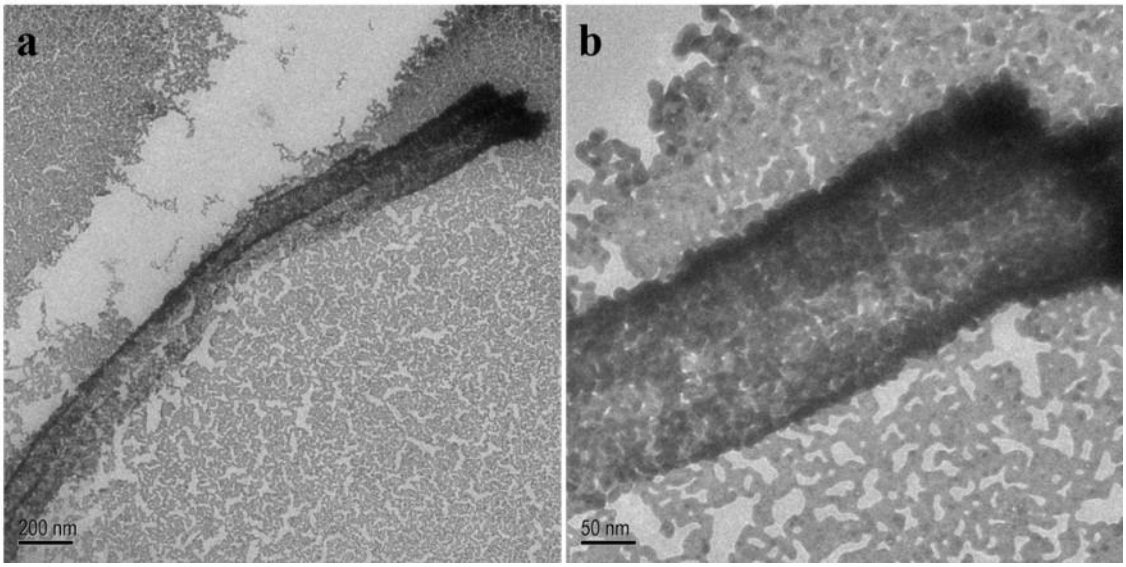

Figure 7.5 TEM images of the as-transferred CuNWs on the in situ chip.

As mentioned above, there are still many issues to be addressed before the successful conducting of the in situ TEM observation of the electrochemical behavior in liquid cell holder. Among them, the damage of the CuNWs and the Pt contamination are two biggest challenges in front of the experiment. More solutions are being working in progress in order to achieve the in situ TEM observation of the electrochemical process on nanomaterials in the near future.

7.2.2 Fabrication of Co-based nano-dendritic structures for electrocatalysis

Different from Cu, the low exchange current densities of Ni and Co makes the fabrication of foam structures with nano-dendritic morphology much more difficult than those with high values like Cu and Au et al. The construction of Ni-based metal foam have been

widely reported as the conductive support with large surface area while no such structures based on Co have been synthesized.[3-6]

Co-based 3D foam has been successfully fabricated via bubble dynamic template method by electrodeposition. Similar to the Ni cases above, the electrolyte used for the deposition is the mixture of high concentrated ammonium chloride and less cobalt chloride, where the ammonium chloride can not only act as a complexing agent but also adjust the pH value of the electrolyte.

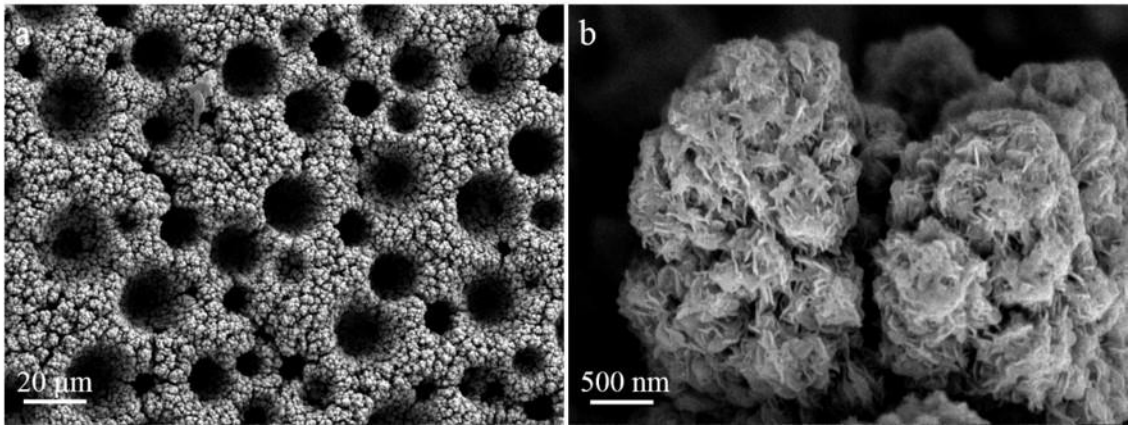

Figure 7.6 SEM images of the as-fabricated Co foam.

Different from the copper foam in Chapter 5 and 6, the morphology of the Co foam is seen to be more compact with low density of micron pores, which is believed to be ascribed to the intrinsic properties of the Co and the complexing agent or surfactant that can affect the surface electric charge of the nanoparticles. Moreover, unlike the Cu-dendrites, the Co-dendrites turns out to be covered with nano-flakes on the outmost surface, which is still needed to be further characterized. Taking advantage of this nano-flake layer, surface treatment to transform this layer into Co-MOFs can be employed as the template for the further modification to fabricate a thin layer of active catalyst for the HER, OER or ORR applications.

In addition, the fabrication of bi-metal (Co, Ni) or tri-metal (Co, Ni, Fe) foam with adjustable elemental ratio can also been attempted as the conductive template for the further surface modification to produce high-performance materials for the bubble-related

electrocatalysis, where the porous structure can facilitate the rapid transport of electrolyte and the bubbles and the template is able to provide a large surface area to load active materials for the electrocatalysis.

7.3 Outcomes Reflected in the Original Hypothesis

In this thesis, the three original hypotheses have all been well reflected by the outcomes of the experiments. The specific details are as followed:

First, single crystalline CuNWs were successfully fabricated via electrodeposition method and their electrochemical behaviors were subsequently studied based on atmospheric exposure, electrochemical measurement and TEM characterization. The results are in good agreement with the hypothesis that the electrochemical behaviors of the CuNWs is quite different from their bulk counterpart when subject to the same environments or treatments. Although the uniform Cu_2O film also follows the logarithmic law growth rate with the increase of exposure duration of CuNWs in 40 % RH air like the bulk copper sample, the growth rate of the Cu_2O film on CuNWs is much higher than those formed on their bulky counterpart.

Second, the CuNDs present an unusual CV curve as expected when being subject to the electrochemical scan in alkaline solution, indicating their special electrochemical behavior compared to the homogeneous CuNWs. This is because the electrochemical oxidation mechanism on the hierarchical CuNDs with abundant defects is much different from that on the homogeneous CuNWs with smooth surface. The results are in accordance with the second hypothesis.

Last, the third hypothesis is that the surface modification on the CuNDs would greatly improve their catalytic activity for OER, which has been well proved by the experiment in Chapter 6. Specifically, nanostructured CuO/C hollow shell could act as active layer whilst the CuO passive film is able to protect the CuNDs from electrochemical corrosion in harsh

alkaline electrolyte so that a high OER efficiency is achieved by HS-CuO/C CuNDs for a long term electrolysis.

References

[1] Yuk, J. M.; Park, J.; Ercius, P.; Kim, K.; Hellebusch, D. J.; Crommie, M. F.; Lee, J. Y.; Zettl, A.; Alivisatos, A. P., *Science* **2012,** *336* (6077), 61-64.

[2] Loh, N. D.; Sen, S.; Bosman, M.; Tan, S. F.; Zhong, J.; Nijhuis, C. A.; Král, P.; Matsudaira, P.; Mirsaidov, U., *Nat. Chem.* **2017,** *9* (1), 77.

[3] Nguyen, T.; Eugénio, S.; Boudard, M.; Rapenne, L.; Carmezim, M. J.; Silva, T. M.; Montemor, M. F., *Nanoscale* **2015,** *7* (29), 12452-12459.

[4] Wang, M.; Yu, X.; Wang, Z.; Gong, X.; Guo, Z.; Dai, L., *J. Mater. Chem.A.* **2017,** *5* (20), 9488-9513.

[5] Chen, G. F.; Su, Y. Z.; Kuang, P. Y.; Liu, Z. Q.; Chen, D. Y.; Wu, X.; Li, N.; Qiao, S. Z., *Chem. Eur. J.* **2015,** *21* (12), 4614-4621.

[6] Xia, X.; Tu, J.; Zhang, Y.; Mai, Y.; Wang, X.; Gu, C.; Zhao, X., *J. Phys. Chem. C* **2011,** *115* (45), 22662-22668.

Publications

1. **Zhang, B.**, Yang, G., Li, C., Huang, K., Wu, J., Hao, S., ... & Huang, Y.(2018). Electrochemical behaviors of hierarchical copper nanodendrites in alkaline media. *Nano Research*, Nano Res. 11, 4225.
2. **Zhang, B.**, Yang, G., Li, C., Huang, K., Wu, J., Hao, S., ... & Huang, Y. (2018). Phase controllable fabrication of zinc cobalt sulfide hollow polyhedra as high-performance electrocatalysts for the hydrogen evolution reaction. *Nanoscale*, 10.1774-1778.
3. **Zhang, B.**, Chen, B., Wu, J., Hao, S., Yang, G., Cao, X., ... & Huang, Y. (2017). The Electrochemical Response of Single Crystalline Copper Nanowires to Atmospheric Air and Aqueous Solution. *Small*, 13(10), 1603411.
4. **Zhang, B.**, Hao, S., Wu, J., Li, X., Li, C., Di, X., & Huang, Y. (2017). Direct evidence of passive film growth on 316 stainless steel in alkaline solution. *Materials Characterization*, 131,168-174.
5. **Zhang, B.**, Hao, S., Xiao, D., Wu, J., & Huang, Y. (2016). Templated formation of porous Mn2O3 octahedra from Mn-MIL-100 for lithium-ion battery anode materials. *Materials & Design*, 98, 319-323.
6. **Zhang, B.**, Hao, S., Wu, J., Li, X., & Huang, Y. (2016). Evidence of a nanosized copper anodic reaction in an anaerobic sulfide aqueous solution. *RSC Advances*, 6(24), 19937-19943.
7. **Zhang, B.**, Wu, J., Peng, D., Li, X., & Huang, Y. (2016). In-situ Scanning Micro-Electrochemical Characterization of Corrosion Inhibitors on Copper. *Int. J. Electrochem. Sci*, 11, 4110-4119.
8. **Zhang, B.**, Wu, J., Li, X., Liu, H., Yadian, B., Ramanujan, R. V., ... & Huang, Y. (2014). Passivation of Nickel Nanoneedles in Aqueous Solutions. *The Journal of Physical Chemistry C*, 118(17), 9073-9077.
9. Yang, G.[1], **Zhang, B.[1]**, Feng, J., Lu, Y., Wang, Z., Aravindan, V., ... & Huang, Y. (2018). Morphology controlled lithium storage in Li 3 VO 4 anodes. *Journal of Materials Chemistry A*, 6, 456-463.
10. Hao, S.[1], **Zhang, B.[1]**, Feng, J., Liu, Y., Ball, S., Pan, J., ... & Huang, Y. (2017). Nanoscale ion intermixing induced activation of Fe 2 O 3/MnO 2 composites for

application in lithium ion batteries. *Journal of Materials Chemistry A*, 5(18), 8510-8518.

11. Hao, S.[1], **Zhang, B.[1]**, Ball, S., Hu, B., Wu, J., & Huang, Y. (2016). Porous and hollow NiO microspheres for high capacity and long-life anode materials of Li-ion batteries. *Materials & Design*, 92, 160-165.
12. Hao, S., **Zhang, B.**, Ball, S., Wu, J., Srinivasan, M., & Huang, Y. (2016). Phase transition of hollow-porous α-Fe 2 O 3 microsphere based anodes for lithium ion batteries during high rate cycling. *Journal of Materials Chemistry A*, 4(42), 16569-16575.
13. Dou, J., **Zhang, B.**, Liu, H., Hong, J., Yin, S., Huang, Y., & Xu, R. (2016). Carbon supported Pt9Sn1 nanoparticles as an efficient nanocatalyst for glycerol oxidation. *Applied Catalysis B: Environmental*, 180, 78-85.
14. Hao, S., **Zhang, B.**, Ball, S., Copley, M., Xu, Z., Srinivasan, M., ... & Huang, Y. (2015). Synthesis of multimodal porous ZnCo2O4 and its electrochemical properties as an anode material for lithium ion batteries. *Journal of Power Sources*, 294, 112-119.
15. Huang, H., Feng, J., Fu, H., **Zhang, B.**, Fang, T., Qian, Q., Huang, Y., ... & Zou, Z. (2018). Improving solar water-splitting performance of LaTaON2 by bulk defect control and interface engineering. *Applied Catalysis B: Environmental*. (2018), 226, 111-116.
16. Lin, Z. Q., Xie, J., **Zhang, B.**, Li, J., Weng, J., Song, R., ... & Xu, Z. (2017). Solution-processed nitrogen-rich graphene-like holey conjugated polymer for efficient lithium ion storage. *Nano Energy*, 41, 117-127.
17. Zhao, T., Liu, Z., Du, C., Dai, C., & Li, X., **Zhang, B.**. (2017). Corrosion fatigue crack initiation and initial propagation mechanism of E690 steel in simulated seawater. *Materials Science and Engineering: A*, 708, 181-192.
18. Tu, W., Xu, Y., Wang, J., **Zhang, B.**, Zhou, T., Yin, S., ... & Zou, Z. (2017). Investigating the Role of Tunable Nitrogen Vacancies in Graphitic Carbon Nitride Nanosheets for Efficient Visible-Light-Driven H2 Evolution and CO2 Reduction. *ACS Sustainable Chemistry and Engineering*, 5, 7260-7268.
19. Wang, Y., He, J., Mu, X., Wang, D., **Zhang, B.**, Shen, Y., ... & Chen, H. (2017). Solution Growth of Ultralong Gold Nanohelices. *ACS nano*, 11(6), 5538-5546.

20. Du, X., Yao, H., Ma, M., Feng, T., **Zhang, B.**, Xu, Y., ... & Huang, Y. (2017). Green ball dianthus-like Na2Ti6O13 as high-rate performance anode for sodium-ion batteries. *Journal of Alloys and Compounds*,721, 100-105.
21. Liu, J., Chen, Z., Xuan, W., Chen, S., **Zhang, B.**, Wang, J., ... & Huang, Y. (2017). "Electron/Ion Sponge"-Like V-Based Polyoxometalate: Toward High-Performance Cathode for Rechargeable Sodium Ion Batteries. *ACS nano*, 11(7), 6911-6920.
22. Wu, J., Peng, D., He, Y., Du, X., Zhang, Z., **Zhang, B.**, ... & Huang, Y. (2017). In Situ Formation of Decavanadate-Intercalated Layered Double Hydroxide Films on AA2024 and their Anti-Corrosive Properties when Combined with Hybrid Sol Gel Films. *Materials*, 10(4), 426.
23. Zhang, Y., Xia, X., Cao, X., **Zhang, B.**, Tiep, N. H., He, H., ... & Fan, H. J. (2017). Ultrafine Metal Nanoparticles/N‐Doped Porous Carbon Hybrids Coated on Carbon Fibers as Flexible and Binder‐Free Water Splitting Catalysts. *Advanced Energy Materials*, 7(15), 1700220.
24. Yang, G., Feng, J., **Zhang, B.**, Aravindan, V., Peng, D., Cao, X., ... & Huang, Y. (2017). Solvothermal synthesis of Li3VO4: Morphology control and electrochemical performance as anode for lithium-ion batteries. *International Journal of Hydrogen Energy*, 42 (34), 22167-22174.
25. Chen, M., Chao, D., Liu, J., Yan, J., **Zhang, B.**, Huang, Y., ... & Shen, Z. X. (2017). Rapid Pseudocapacitive Sodium‐Ion Response Induced by 2D Ultrathin Tin Monoxide Nanoarrays. *Advanced Functional Materials*, 27(12), 1606232.
26. Xu, Y., Tu, W., **Zhang, B.**, Yin, S., Huang, Y., Kraft, M., & Xu, R. (2017). Nickel Nanoparticles Encapsulated in Few‐Layer Nitrogen‐Doped Graphene Derived from Metal‐Organic Frameworks as Efficient Bifunctional Electrocatalysts for Overall Water Splitting. *Advanced Materials*, 29(11), 1605957.
27. Yao, Z., Xia, X., Zhong, Y., Wang, Y., **Zhang, B.**, Xie, D., ... & Huang, Y. (2017). Hybrid vertical graphene/lithium titanate–CNTs arrays for lithium ion storage with extraordinary performance. *Journal of Materials Chemistry A*, 5(19), 8916-8921.

28. Zhou, J., Liu, F., Lin, J., Huang, X., Xia, J., **Zhang, B.**, ... & Wang, X. (2017). Large‐area and high‐quality 2D transition metal telluride. *Advanced Materials*, 29(3), 1603471.
29. Dou, J., Yin, S., Chong, J. Y., **Zhang, B.**, Han, J., Huang, Y., & Xu, R. (2016). Carbon spheres anchored Co3O4 nanoclusters as an efficient catalyst for dye degradation. *Applied Catalysis A: General*, 513, 106-115.
30. Zhu, B., Huang, Y., Fan, L., Ma, Y., Wang, B., Xia, C., **Zhang, B.**, ... & Lund, P. D. (2016). Novel fuel cell with nanocomposite functional layer designed by perovskite solar cell principle. *Nano Energy*, 19, 156-164.
31. Zhang, Z., Mu, S., **Zhang, B.**, Tao, L., Huang, S., Huang, Y., ... & Zhao, Y. (2016). A novel synthesis of carbon nanotubes directly from an indecomposable solid carbon source for electrochemical applications. *Journal of Materials Chemistry A*, 4(6), 2137-2146.
32. Jing, L., Tay, R. Y., Li, H., Tsang, S. H., Huang, J., Tan, D., **Zhang, B.**, ... & Tok, A. I. Y. (2016). Coaxial carbon@ boron nitride nanotube arrays with enhanced thermal stability and compressive mechanical properties. *Nanoscale*, 8(21), 11114-11122. (IF: 7.3670)
33. Liu, Z., Yadian, B., Liu, H., Liu, C., **Zhang, B.**, Ramanujan, R. V., & Huang, Y. (2013). Fabrication of hybrid CuO/Pt/Si nanoarray for non-enzymatic glucose sensing. *Electrochemistry Communications*, 33, 138-141.
34. Wu, J., Li, X., Yadian, B., Liu, H., Chun, S., **Zhang, B.**, ... & Huang, Y. (2013). Fabrication of hybrid CuO/Pt/Si nanoarray for non-enzymatic glucose sensing. *Electrochemistry Communications*, 26, 21-24.